AN INVESTIGATION OF NANOMATERIALS FOR SOLAR CELLS, CATALYSTS AND SENSORS

By

TYLER DEED POUNDS

A thesis submitted in partial fulfillment of the requirements for the degree of:

MASTER OF SCIENCE IN MATERIALS SCIENCE AND ENGINEERING

WASHINGTON STATE UNIVERSITY
School of Mechanical and Materials Engineering

MAY 2007

To the Faculty of Washington State University:

The members of the Committee appointed to examine the dissertation/thesis of TYLER DEED POUNDS find it satisfactory and recommend that it be accepted.

_____

Chair

_____

_____

_____

ACKNOWLEDGEMENTS

The author wishes to acknowledge Dr. M Grant Norton and Dr. David McIlroy for their supervision, expert assistance, sharp insight and tremendous help with all material. Special thanks to Dr. Matt McCluskey and Dr. Kelvin Lynn for their guidance, input and assistance. Dr. Robert Olson, Dr. David Field and Dr. David Bahr are recognized for providing expertise in several areas.

Much gratitude is offered to the W. M. Keck Foundation for support of this research.

AN INVESTIGATION OF NANOMATERIALS FOR SOLAR CELLS, CATALYSTS AND SENSORS

ABSTRACT

By Tyler Deed Pounds, M. S.
Washington State University
May 2007

Chair: M. Grant Norton

Nanoscale metals and ceramics have ideal properties for a wide range of modern applications. Quantum size effects give nanomaterials different electronic properties than their bulk counterparts in many cases. These unique properties make nanomaterials attractive for modern medical, imaging, optic, sensor, catalyst and alternative energy devices. Several factors including processing conditions, crystallographic properties and surface features affect the quality of nanomaterials for potential applications. Many of these areas require further research before nanomaterials can impact technology in the areas they have been proposed.

Thin films composed of Ag nanoparticles in a Teflon matrix exhibited absorption spectrum that varied according to the microstructure of the film and closely matched the solar spectrum with the proper microstructure. At resonant wavelengths optical absorption occurs due to surface plasmon resonance in metal nanoparticles as a response to polarization by an incident light wave. This phenomenon was responsible for the absorption of the Ag/Teflon composites that were analyzed. A model for predicting optical absorption by metal nanoparticle/dielectric composite thin films based on the microstructure of the films has been developed. Depending on the size and shape distribution of the metal nanoparticles and materials used, the model can accurately predict optical absorption spectra for metal nanoparticle/dielectric thin films.

Optical absorption spectra due to surface plasmon resonance of smooth metal nanoparticles dispersed in a dielectric were predicted based on the materials used to form the films as well as microstructural characteristics. The volume fraction of metal in the film and aspect ratio of the individual metal nanoparticles strongly influenced the absorption properties of the composite thin films. Characterization of the relative volume of the components and aspect ratio distribution of the films allowed for accurate prediction of the optical absorption spectrum using the model. In addition the developed model gives basis for optimization of the nanostructure of metal nanoparticle/dielectric thin films for tailored absorption properties.

TABLE OF CONTENTS

Page

LIST OF TABLES

LIST OF FIGURES

INTRODUCTION

In the past two decades, nanomaterials research surged due to the unique properties and immense amount of potential application. The discovery of carbon nanotubes (CNT) in 1991 helped to spur new interest in nanomaterials.[1] A tremendous amount of research is now focused on integrating nanotechnology into industrial and commercial devices. The widespread concentration on nanomaterials has ushered in a new era in materials research, often called the nano age.[2].

In the early years following the first laboratory controlled formation of carbon nanotubes, much effort was put forth to develop processes for fabricating 1D nanostructures such as nanowires and nanotubes of many types of materials, such as oxides, precious metals and commonly used semiconductors.[3-5] As new methods for forming these materials were developed, research proved that nanomaterials had drastically different mechanical and electronic properties than bulk material.[6, 7] Due to these interesting properties, non-traditional applications were proposed for many materials, leading to a revival in study for several materials. Gold is an excellent example of a material that received new interest due to its properties near the atomic scale.[8] The continuous electronic bands of Au are quantized for Au particles in the nm size range (nanoparticles).[9] The quantization of the bands, often called quantum size effects, creates many new electronic states, making Au nanoparticles extremely chemically active, while bulk Au is very inert.

One-dimensional ceramic nanostructures are ideal for a wide range of applications due to their high surface area and tunable properties. In many 1D ceramic nanostructures, the surface chemistry is controlled by the processing conditions. For example, the oxygen vacancy density

on the surfaces of transition metal oxide nanostructures is often dependent on specific gas partial pressures during growth.[10] One-dimensional ceramic nanostructures are ideal for catalytic applications where surface vacancies are reactive sites for many catalytic processes.

Various growth processes present ways to form large amounts of identical, single crystal nanostructures in one growth procedure with the crystallographic properties dependent on the growth process.[11, 12] Material adsorption is a key process in sensor and catalyst applications, and certain crystallographic planes in a catalyst or sensor support material interact with adsorbed species differently.[13] In this respect, one-dimensional ceramic nanostructures have much more useful surface area for adsorption than any currently used sensor or catalyst material.

Metal nanoparticles have much different electronic properties than bulk material, lending them to a variety of new applications. Particles in the range of tens of nm are unable to prevent polarization in an incident electromagnetic (EM) field by the same mechanism as a bulk metal. Surface plasmons, dense areas of conduction electrons, form on nanoparticle surfaces under the right conditions in an EM field to counteract large order polarization. Surface plasmons have many potential uses including imaging and photovoltaic (PV) materials.

In recent years, nanomaterials research has largely shifted away from basic formation techniques towards development of specific systems for several applications of high importance. With several basic formation techniques and their primary mechanisms well established and understood relatively well (although cheap mass production techniques remain a major issue), the final hurdle preventing widespread incorporation of 1D ceramic nanostructures and metal nanoparticles into everyday devices is finding the optimal materials for a number of important applications.

A primary target for 1D ceramic nanostructures and metal nanoparticles is energy materials. The need for affordable alternative energy sources is rising as the demand for energy increases and the supply of non-renewable energy resources diminishes. According to the Department of Energy, over 85% of the energy consumed in the U.S. is currently provided by coal, natural gas, and petroleum: all non-renewable resources.[14] These energy sources are often detrimental to the environment, and their price may rise to unaffordable levels for many people in the near future. The demand for non-renewable resources is expected to increase dramatically on a global scale as developing nations become industrialized and the world population continues to increase.

Solar energy remains the largest supply of untapped natural energy. Only a small percentage of solar energy that reaches the Earth could be used to fill the world's energy demand. Among other issues, the primary problem with current solar cells is their inability to efficiently absorb the entire spectrum of solar radiation. Solar radiation strikes the Earth as light waves in the infrared, visible, and ultraviolet wavelengths. Current solar cell materials are only capable of converting a very narrow range of wavelengths into electrical energy. However, Metal nanoparticle/dielectric composite thin films can be engineered to efficiently absorb solar radiation.[15] The absorption spectrum of these films are a function of the materials used and nanoparticle morphology. We have developed a model for predicting the absorption of metal nanoparticle/composite thin films from microstructural images that not only allows for prediction of absorption characteristics but provides a guideline for engineering PV materials from almost any combination of metal and dielectric.

The enormous surface area of 1D ceramic nanostructures and metal nanoparticles make them ideal as catalysts. In a small volume of material, there are enormous amounts of reactive

surface sites compared even to thin films. In addition, 1D dimensional ceramic nanostructures catalysts are typically operate more efficiently low temperatures compared to thin films. Nanoscale ceramics and metals have shown promise as fuel cell catalysts and hydrogen storage devices, two key issues that must be solved before fuel cells can realistically be introduced into automobiles on a large scale.[16-18]

One-dimensional nanostructures have been proposed as next generation sensors. Several properties make 1D ceramic nanostructures ideal sensors. Detection devices using 1D ceramic nanostructures have been shown to have much better sensitivity and faster detection times at with lower operating temperatures than the best thin film sensors.[19, 20] Under the right conditions, the resistivity of a 1D nanostructure can change by orders of magnitude in less a second when even a single molecule or atom is adsorbed on the surface of the nanostructure. Ultra sensitive detectors selective to an individual DNA sequence have been fabricated, demonstrating the potential for portable anti-terrorism devices based on 1D nanostructures.[21] Much work still remains to determine ideal materials systems in order to make 1D ceramic nanostructure based sensors competitive with traditional sensors.

References

1. S. Iijima, Nature, **354**, 56 (1991).

2. http://www.eurekalert.org/features/doe/2001-10/dbnl-tco052302.php

3. E. Comini, G. Faglia, G. Sberveglieri, Z. Pan, and Z. L. Wang, Appl. Phys. Lett., **81**, 1869 (2002).

4. T. Scheibel, R. Parthasarathy, G. Sawicki, X. M. Lin, H. Jaeger and S. L Lindquist, Biophys., **100**, 4527 (2003).

5. L. Schubert, P. Werner, N.D. Zakharov, G. Girth, F. M. Kolb, L. Long, U. Gösele, and T. Y. Tan, Appl. Phys. Lett., **84**, 4968 (2004).

6. J. Hu, T. W. Odom and C. M. Lieber, Acc. Chem. Res., **32**, 435 (1999).

7. Z. L. Wang, Z. R. Dai, R. P. Gao, Z. G. Bai and J. L. Gole, Appl. Phys. Lett., **77**, 3350 (2000).

8. M. Haruta, Applied Catalysis A: General, **222**, 427 (2001).

9. M. Haruta, The Chemical Record, **3**, 75 (2003).

10. B. Lei, C. Li, D. Zhang, T. Tang and C. Zhou, Appl. Phys. A, **79**, 439 (2004).

11. N. S. Ramgir, I. S. Mulla, K. P. Vijayamohanan, Sensors and Actuators B, **107**, 708 (2005).

12. Y. Cai, S. K. Chan, I. K. Sou, Y. F. Chan, D. S. Su, and N. Wang, Adv. Mater., **18**, 109 (2004)

13. K. Zhou, X. Wang, X. Sun, Q. Peng, and Y. Li, J. Catal., **229**, 206 (2005).

14. http://www.eere.energy.gov/states/us_energy_statistics.cfm#consumption

15. H. Eilers, A. Biswas, T. D. Pounds, M. G. Norton and M. Elbahari, J. Mater. Res., **21**, 2168 (2006).

16. C. Wang, M. Waje, X. Wang, J. M. Tang, R. C. Haddon, and Y. Yan, Nano Lett., **4**, 345 (2004).

17. S. F. Yin, B. Q. Xu, C. F. Ng, and C. T. Au, Appl. Catal. B, **48**, 237 (2004).

18. J. N. Armor, Catal. Lett., **101**, 131 (2005).

19. Z. Sun, H. Yuan, Z. Liu, B. Han, and X. Zhang, Adv. Mater., **17**, 2993 (2005).

20. R. W. Bogue, Sensor Review, **24**, 253 (2004).

21. Z. Li, Y. Chen, X. Li, T. I. Kamins, K. Nauka, and R. S. Williams, Nano Lett., **4**, 245 (2004).

A MODEL FOR BROADBAND OPTICAL ABSORPTION BY METAL NANOPARTICLE/DIELECTRIC THIN FILMS

ABSTRACT

Metal nanoparticles exhibit optical absorption through localized surface plasmons. Under the right conditions, they show non-linear absorption properties in the visible part of the electromagnetic spectrum. Sharp absorption peaks may be observed at the resonant wavelengths for individual nanoparticles. At this wavelength, the magnitude of the electric field induced on the surface of a nanoparticle can exceed that of the incident field. Metal nanoparticle/polymer composite thin films can be synthesized to absorb over a range of wavelengths. The resonant wavelength is dependent on the metal, the dielectric matrix, and the size and shape of the nanoparticle. A model for predicting the optical absorption for photovoltaic applications of metal nanoparticles held in a dielectric has been developed. This model permits microstructural optimization for solar energy capture.

INTRODUCTION

Metal particles have been used to add vibrant colors to glass for centuries. In most cases, these glasses are not the color of the bulk metal used as the colorant. One of the most famous examples is the Lycurgus Cup, which is dichroic: red in transmitted light and green in reflected. The color is due to silver/gold alloy nanoparticles.[1] In 1904, Maxwell-Garnett (MG) first proposed resonant optical absorption as the explanation for the seemingly unnatural optical properties of small metal particles.[2]. Later, Mie theorized that spherical metal particles in a dielectric exhibited resonant absorption by the oscillation of free electrons under the proper boundary conditions.[3] These two theories were subsequently expanded, leading to a more complete understanding of nanoscale optics.[4, 5] In the past decade, metal nanoparticles have received much attention for potential applications including surface enhanced raman spectroscopy (SERS), biosensors and near-field optical microscopy.[e.g., 6, 7, 8]

Surface plasmons, dense localized regions of electrons, form on the surfaces of metal particles at metal nanoparticle/dielectric interfaces to counteract polarization by incident electromagnetic (EM) fields. Incident light waves produce surface plasmons with fields of greatest magnitude at the surface plasmon resonance (SPR) conditions for each individual nanoparticle. Recently, thin film materials containing arrays of metal nanoparticles have been considered for photovoltaic (PV) applications due to SPR absorption.[9] Since individual nanoparticles have resonant wavelengths strongly dependent on multiple shape and material factors, efficient, broadband PV materials based on SPR will only be possible with properly engineered materials. Our previous research showed that the optical absorption of Ag nanoparticles in a Teflon AF matrix can closely match the solar spectrum.[10] Several thin film

samples were prepared with varying Ag volume concentration by a co-evaporation process. The experimental results indicated that the volume fractions of each component and the particle size distribution of Ag had significant effects on the measured absorption spectra.

In this paper, the important parameters for creating ideal PV materials that absorb efficiently over the entire solar spectrum are identified. Mie and MG theories are used to create a model for predicting the optical absorption of metal nanoparticle/dielectric thin films. This theory is then shown to predict the results obtained in our previous experimental studies.

RESULTS/DISCUSSION

The parameters that most strongly influence SPR absorption have been identified and used to create a model for predicting the response of metal nanoparticle/dielectric composite thin films that have potential as PV materials.

The dielectric material must form a barrier to electron flow with the metal nanoparticles in order to create an interface where SPR is possible. If the conduction electrons of the metal are able to freely move across the interface, polarization induced by incident light may be counteracted in a manner other than SPR. For example, bulk metals resist polarization by incident EM waves through free movement of the conduction electrons. Conduction electrons are scattered by surfaces in nanomaterials, preventing them from quickly responding to external electric fields. At resonant frequencies of electron transitions, surface plasmons form in response to incident light when conduction electrons are unable to reduce the net polarization of the particle due to surface scattering. Table 1 summarizes the variables that will be used in developing our model.

Table 1. Terms and their units

Variable	Definition	Unit
ε_D	Dielectric constant of dielectric	None
ε_{1m}	Real part of Drude dielectric function of metal	None
ε_{2m}	Imaginary part of Drude dielectric function of metal	None
ε_0	Dielectric constant due to interband electron transitions in metal	None
λ_p	Bulk plasma wavelength of metal	nm
λ_{sp}	Surface plasmon wavelength of metal nanoparticle	nm
λ	Wavelength of incident light	nm
f	Volume fraction of metal	None
A	Aspect ratio of metal nanoparticle	None
α	Polarization of metal nanoparticle	nm^{-1}
P	Shape factor	None
$\Delta\lambda_{SP,\ MATERIAL}$	Shift in SPR wavelength due to materials	nm
$\Delta\lambda_{SP,\ SHAPE}$	Shift in SPR wavelength due to nanoparticle shape	nm

Materials

The metal and dielectric determine the SPR wavelength for perfectly spherical metal nanoparticles and were used as the starting point for our model. According to Mie theory, the absorption coefficient of a metal nanoparticle (where the diameter is much smaller than □) is a function of the wavelength and the dielectric constants of the metal and surrounding dielectric.[3] This relationship is given by Equation 1:

$$\gamma = \frac{18\pi\varepsilon_0^{3/2}}{\lambda}\frac{\varepsilon_{2m}}{(2\varepsilon_D + \varepsilon_{1m})^2 + \varepsilon_{2m}^2} \quad (1)$$

SPR occurs when the condition $2\square_0+\square_{1m}=0$ is satisfied. The real term of the Drude dielectric function for a metal under incident light in the UV, visible, and near IR wavelengths is given by Equation 2:[11]

$$\varepsilon_{1m} = \varepsilon_0 - \frac{\lambda^2}{\lambda_p^2} \quad (2)$$

The SPR wavelength for isolated, spherical nanoparticles in a vacuum ($\square_D=1$) can be determined by substituting the real part of the Drude dielectric function into Equation 1 and solving for □:

$$\lambda_{SP} = \lambda_P(2\varepsilon_D + \varepsilon_0)^{1/2} \quad (3)$$

Using the following properties for Ag: λ_p=137 nm and ε_0=1.1, it was determined that λ_{sp}=242 nm for spherical Ag nanoparticles in a vacuum.[12] This value agrees with other sources.[e.g. 11]

According to MG theory, maximum optical absorption of a two component composite material occurs when incident light has the SPR wavelength at the condition given in Equation 2.[2] The SPR wavelength for spherical nanoparticles is a function of the volume fraction of both components as well as the materials parameters. The SPR wavelength scales according to the volume fraction of the minority component (metal nanoparticles in this model) as shown in Equation 4.[13]

$$\lambda_{SP} = \lambda_P \left(\frac{2+f}{1-f} \varepsilon_D + \varepsilon_0 \right)^{1/2} \tag{4}$$

According to Equation 4, the SPR wavelength of the nanoparticles exhibit a red shift as the volume fraction of the metal increases. This effect has been demonstrated in several metal nanoparticle/dielectric thin films.[e.g. 13, 14]

Figure 1 shows the theoretical dependence of SPR wavelength for spherical Ag nanoparticles in Teflon according to the volume fraction of Ag. This figure was generated using Equation 4 and the properties listed above for Ag and ε_D=2.1 for Teflon.[10]

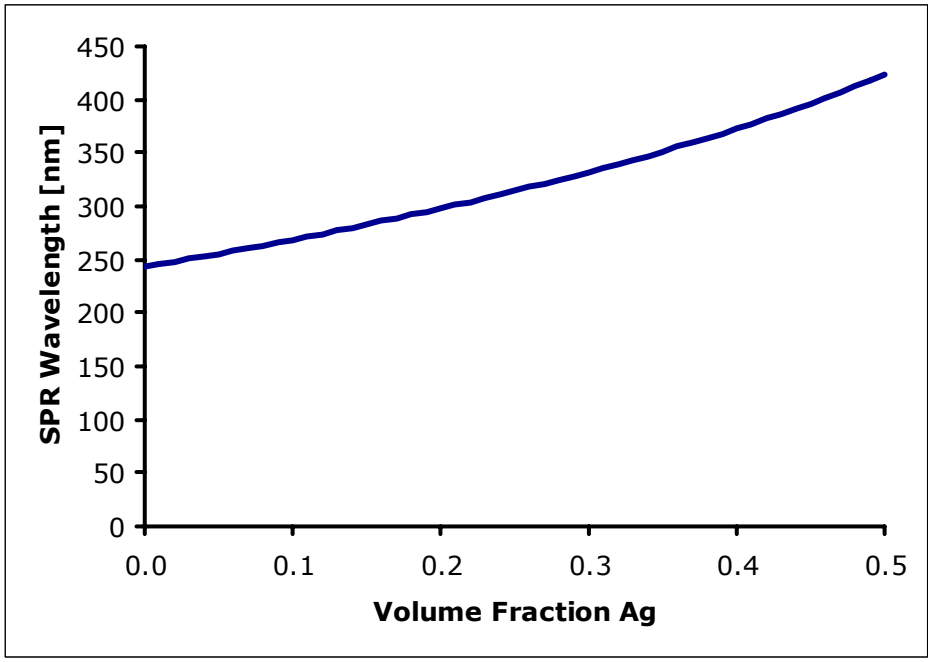

Figure 1. Theoretical SPR wavelength versus. volume fraction of Ag for spherical nanoparticles in a Teflon matrix.

Nanoparticle Size

The size of a metal nanoparticle affects its SPR wavelength and absorption intensity, an effect that has been demonstrated for Au nanoparticles ranging from 60 nm to 30 nm.[15]. In this cited study, 60 nm Au particles showed SPR at 656 nm, while particles with a 30 nm diameter exhibited a SPR peak at 556 nm. However, the shift in SPR absorption peak was relatively small (<50nm) for Au particles ranging in size from 30-43 nm. In the materials analyzed in this study, the Ag nanoparticles were all smaller than 50 nm as shown in the transmission electron microscope (TEM) images of the samples in Figure 2. For this reason, our absorption model does not focus specifically on SPR peak shifts caused by nanoparticle size. However size effects in part explain small deviations in the modeled spectra from the experimental data.

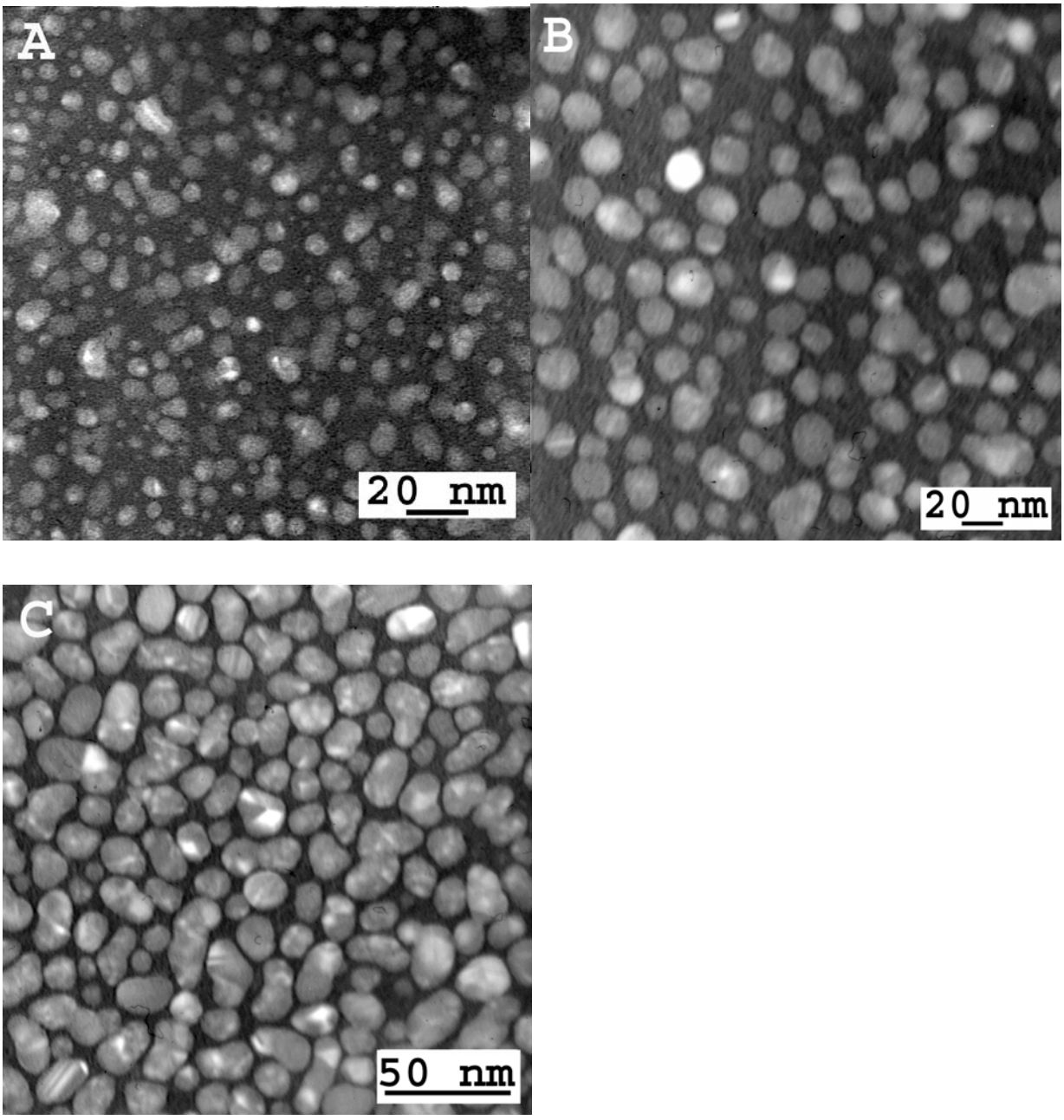

Figure 2. Bright-field TEM images of Ag nanoparticle/TF composite thin films containing: (A) 27 vol% Ag, (B) 30 vol% Ag, and (C) 43 vol% Ag.

Nanoparticle Shape

The shape of an individual metal nanoparticle has strong influence on its optical absorption. Metal nanoparticles deviating from a spherical or equiaxed shape exhibit multiple polarization dipoles corresponding to secondary surface plasmon resonant wavelengths.[16] A single axis extension of a spherical particle into a non-equiaxed particle results in transverse (about the circular cross-section) and longitudinal (about the long axis) resonance modes.[11, 16] Increasing the aspect ratio of an Au nanorod results in a blue shift of the resonant wavelength of the transverse SPR wavelength.[4, 15] However, the SPR wavelength of the longitudinal mode increases with increasing aspect ratio and exhibits a much larger wavelength shift than the transverse mode.[11, 16] In addition, the magnitude of the longitudinal SPR absorption peak is proportional to the aspect ratio of the nanoparticle.[11, 16] Several theoretical and experimental studies have confirmed these shape effects on the optical absorption by metal nanoparticles.[see, for example 11, 16, 17]

According to an extension of Mie Theory, the polarization along the long axis of a non-equiaxed metal nanoparticle is a function of the aspect ratio of the particle.[5] Equations 5 and 6 give the polarization of a non-equiaxed metal nanoparticle and the dependence of its shape factor on aspect ratio:[11]

$$\gamma = \frac{18\pi\varepsilon_0^{3/2}}{\lambda} \frac{\varepsilon_{2m}}{\left(\frac{1-P}{P}\varepsilon_D + \varepsilon_{1m}\right)^2 + \varepsilon_{2m}^2} \tag{5}$$

$$P = \frac{1-e^2}{e}\left[\frac{1}{2e}\ln\left(\frac{1+e}{1-e}\right)-1\right] \text{ where: } e = \sqrt{1-A^{-2}} \quad (6)$$

The SPR wavelength of a non-equiaxed metal nanoparticle with aspect ratio A is a function of the shape factor and is calculated in the same manner as for a spherical nanoparticle. The solutions for a nanorod and spherical particle are identical except for the inclusion of the shape factor, seen in the denominator of Equation 5. The SPR wavelength of the longitudinal mode of a non-equiaxed metal nanoparticle is given by Equation 7:

$$\lambda_{SP} = \lambda_P\left(\frac{1-P}{P}\varepsilon_D + \varepsilon_0\right)^{1/2} \quad (7)$$

Since P decreases as A increases, increasing the aspect ratio of a non-equiaxed nanoparticle should result in a red shift in the SPR wavelength of the longitudinal resonance mode. This effect has been demonstrated in several previous studies.[16, 17]

In order for the model described above to remain accurate, the metal nanoparticles must not percolate to an extent that yields a bulk metal. In our earlier report, Ag nanoparticle/Teflon composite thin films with greater than 60% Ag appeared to exhibit bulk metal absorption properties with no strong SPR absorption peaks.[10]

The SPR absorption spectra of metal nanoparticle/dielectric composites can be predicted from images of the microstructure. Nanoparticle shape and material factors determine the shift of the SPR wavelength for a metal nanoparticle from that of an isolated spherical nanoparticle in a

vacuum. The shift in SPR wavelength due to materials factors can be predicted by subtracting Equation 3 from Equation 4. This result is shown in Equation 8:

$$\Delta\lambda_{SP,MATERIAL} = \lambda_P\left(\frac{2+f}{1-f}\varepsilon_D - 2\right)^{1/2} \tag{8}$$

The shift of the longitudinal axis SPR wavelength in a non-equiaxed nanoparticle in a dielectric from that of a spherical particle in the same dielectric support was determined by subtracting Equation 3 from Equation 7. This result is shown in Equation 9:

$$\Delta\lambda_{SP,SHAPE} = \lambda_P\left(\varepsilon_D\left(\frac{1-P}{P} - 2\right)\right)^{1/2} \tag{9}$$

Equations 8 and 9 were used to predict the total shift in wavelength for individual nanoparticles based on aspect ratio and volume fraction measurements from TEM images such as those shown in Figure 2.

The aspect ratios of individual nanoparticles were calculated using ImageJ software.[18] Each of the SPR wavelength shifts was added onto the SPR wavelength for a spherical Ag nanoparticle in a vacuum to determine the peak absorption wavelength for each nanoparticle. The magnitude of the surface plasmon for each nanoparticle was calculated assuming that the induced field was proportional to the aspect ratio. With these data the absorption spectra for Ag nanoparticle/Teflon composite thin films were predicted, as shown in Figure 3.

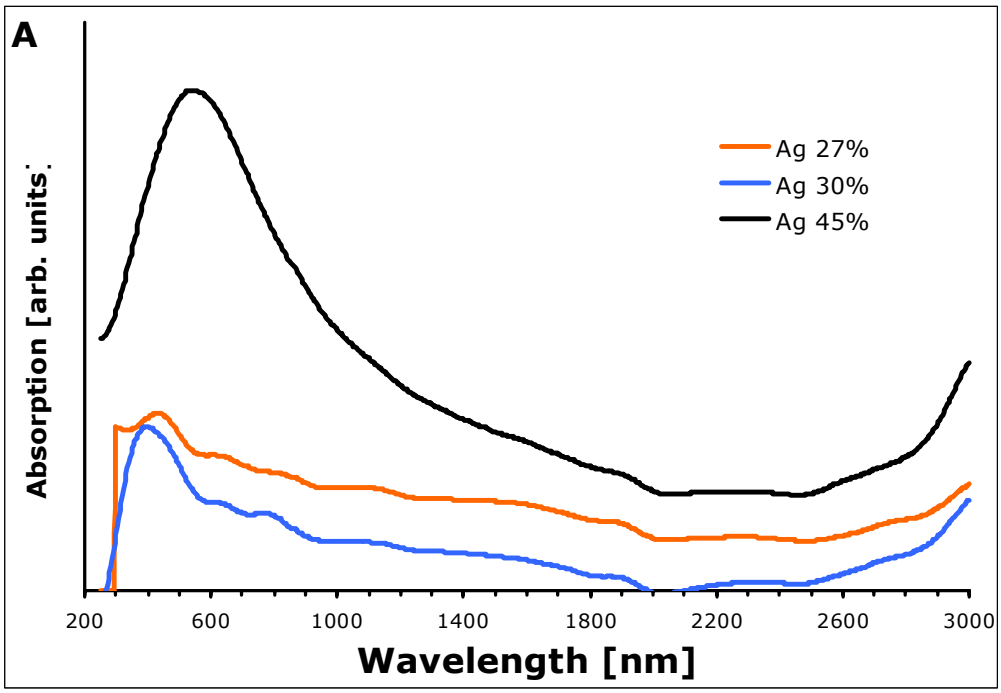
A
Absorption [arb. units]
Ag 27%
Ag 30%
Ag 45%
200
600
1000
1400
1800
2200
2600
3000
Wavelength [nm]

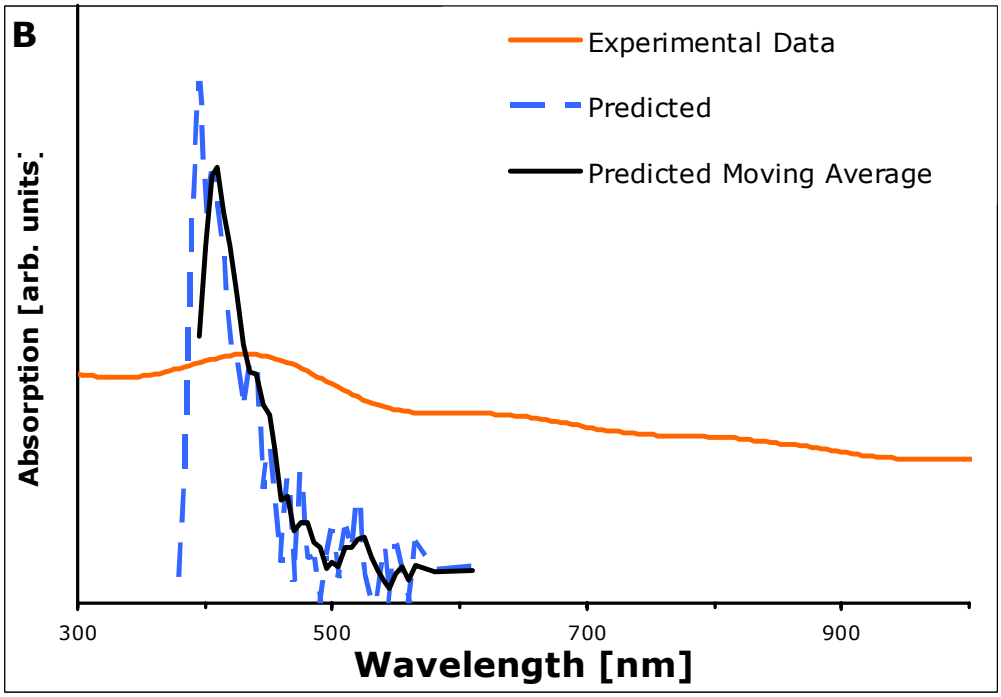
B
Absorption [arb. units]
Experimental Data
Predicted
Predicted Moving Average
300
500
700
900
Wavelength [nm]

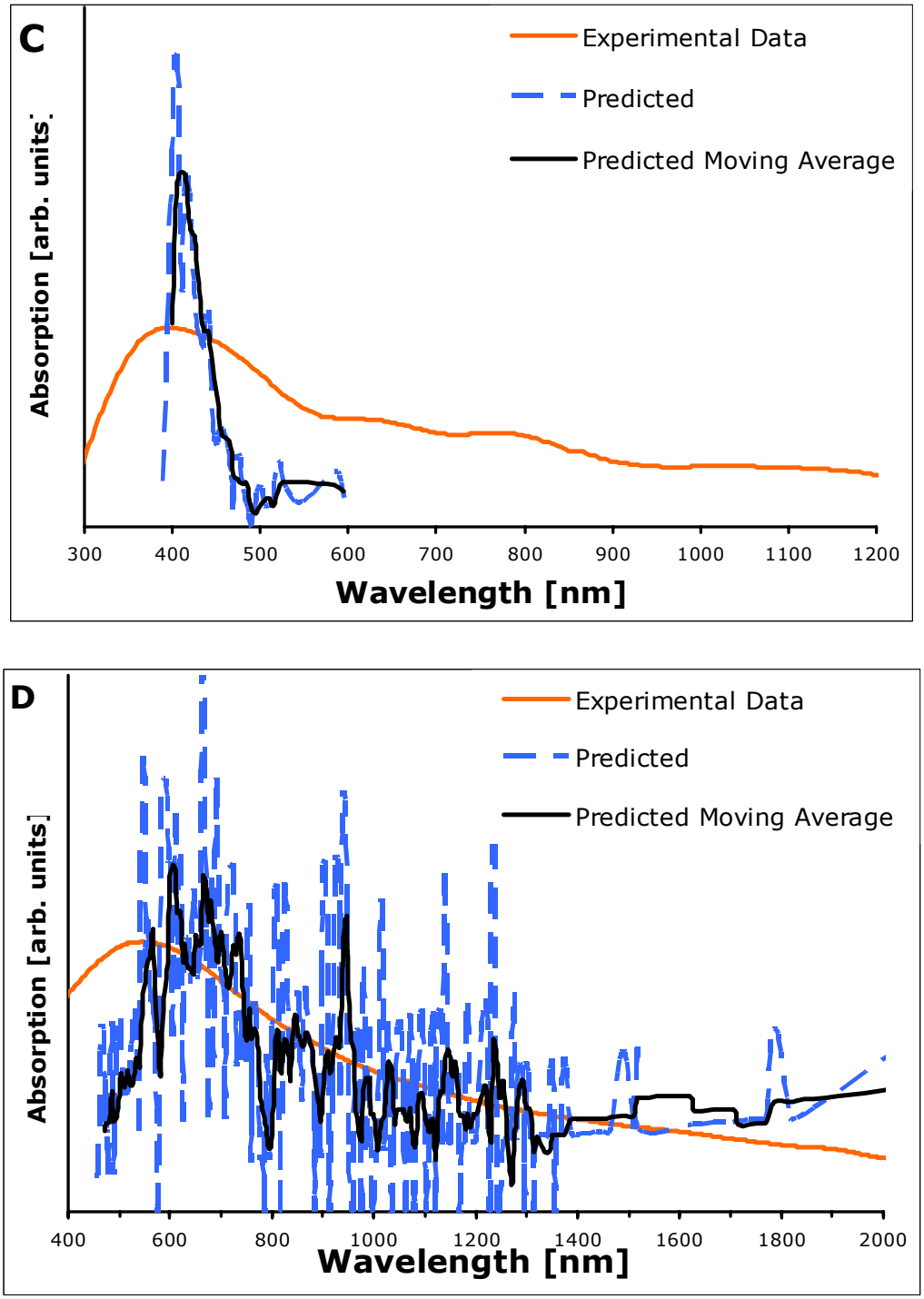

Figure 3. (A) Experimental absorption data for Ag nanoparticle /Teflon composite thin films with three different Ag loadings; (B) Predicted absorption for 27 vol% Ag; (C) Predicted absorption for 30 vol% Ag; (D) Predicted absorption for 45 vol% Ag. The moving average curves show the mean absorption for three data points (i.e. the absorption at 450 nm on the moving average curve is the mean of the absorption at 445, 450, and 455 nm).

The wavelengths of the maximum SPR absorption peaks of the predicted spectra closely match the experimental spectra for all the metal loadings studied. Small deviations result from small shifts in SPR wavelength due to nanoparticle size effects as described earlier. Nanoparticles with similar shapes, but different sizes have slight differences in SPR wavelengths.

The modeled absorption spectra for the 27 and 30 vol% Ag samples do not predict the very weak absorption observed in the IR range of the experimental data. The absence of the absorption 'shoulder' extending from the SPR peak in the modeled spectra results from several issues. The absorption for each Ag particle is modeled as a sharp peak at a single wavelength. In both theory and experimental results, metal nanoparticles exhibit Gaussian type absorption peaks, and size effects can result in broader peaks.[19] SPR absorption effects are not exhibited at a sharp wavelength as estimated by the model. In reality, SPR absorption also occurs at wavelengths near the peak SPR wavelength meaning the SPR peaks in the predicted spectra should be broader.

The modeled absorption spectrum for the 45 vol% Ag sample closely matches the experimental data. This result is of the most interest because the absorption curve very closely matches the solar spectrum. The metal particles in the 45 vol% sample had a much wider distribution of aspect ratios than either of the samples with lower Ag loadings matching our hypothesis that a metal nanoparticle/dielectric composite thin film for efficient PV applications must have a specifically tailored distribution of aspect ratios. These results show that the Ag nanoparticle/Teflon composite thin films will not be effective as broadband PV materials if they contain only spherical particles.

Stereographic considerations can contribute to inaccuracy in the modeled spectra for all samples. The Ag nanoparticles have aspect ratios extending from unity to values probably not exceeding five for the 45 vol% Ag sample. Due to the random orientation of the particles in the film (as evidenced by electron diffraction patterns in the TEM), it is probable that many of the Ag particles that appear nearly spherical in the TEM images may be non-equiaxed particles being imaged at angles that make the particle appear to have a lower aspect ratio (i.e. it is actually a nanorod rather than a nanoparticle). This effect is very difficult to quantify.[20] However, Ag particles in such an orientation should contribute only to SPR absorption at longer wavelengths than those calculated. If exact measurements of the maximum aspect ratios were possible, it is certain that several of the particles contributing to the strong SPR peaks in the model would show a red shift and contribute to broadband absorption spectra.

There are additional stereographic considerations for the estimation of the volume fraction of metal in each sample stemming from uncertainty induced by translating aspect ratio and volume measurements of the Ag nanoparticles from 2D TEM images into a 3D model. The filling volumes of the Ag nanoparticles were calculated from TEM images in our previous paper.[10] It was assumed that the Ag particles were spherical when calculating the volume fraction from the projected area in the TEM images. The volume fraction measurements undoubtedly have error since many of the particles are not spherical. Inaccuracy in the volume fraction measurements would result in a shift of the modeled spectra if corrected. However, the majority of measured aspect ratios fell between 1 and 2 for all samples, indicating that the particles were relatively equiaxed and volume fraction estimates are near the actual values.

Even though there is some uncertainty in measurements taken from our images, it is clear that our model can be used to effectively predict the range of optical absorption by metal

nanoparticles in a dielectric by SPR. In each predicted absorption spectrum, the general intensity or sharpness of the primary SPR absorption peak corresponded well to the broadness of the SPR peak in the experimental data. The predicted spectra had narrower SPR peaks, but the width of the predicted spectra relative to each other showed the same trends as the experimental data.

Based on the strong dependence of the longitudinal SPR resonance mode on materials parameters and shape factors, a highly efficient solar absorption material could be created from an array of smooth, isolated, metal nanoparticles supported in a dielectric. Given a specific metal and dielectric, the ideal system would have a distribution of aspect ratios such that the absorption spectrum of the array would match the solar spectrum. Individual combinations of metals and dielectrics would require different aspect ratio distributions, but it is given that a metal nanoparticle/dielectric composite thin film with nanoparticles of the same shape will not absorb over a broad range of wavelengths. The nanoparticles must have the proper distribution such that the longitudinal SPR wavelength modes yield an absorption spectrum matching the solar spectrum. Given these parameters, engineering thin films with broadband absorption, efficient PV materials might be possible with a wide range of metal/dielectric combinations.

Our model can be used to interpret a variety of experimental results. For example, previous reports have indicated that increasing the concentration of metal nanoparticles in a metal/dielectric thin film results in a red shift of the absorption peak. Liao and colleagues reported this effect for Au nanoparticle/TiO_2 and Au nanoparticle/SiO_2 composite thin films.[21, 22] For the Au nanoparticle/SiO_2 films, the SPR wavelength was 530 nm with 21% Au and 540 nm with 45% Au. This shift is slightly less than our model would predict. Using Equation 4 and a dielectric constant of 3.9 for SiO_2, we would predict the SPR peak for a thin film with 21% Au to be approximately 430 nm, while a thin film with 45% Au should be around 560 nm.[23] These

cited papers did not contain images of the microstructures. Hence, aspect ratio effects were not considered. The volume percentage of Au for each film was measured by XPS, however direct calculations from images may give slightly different values. Even 3 vol% changes in the Au concentrations would have resulted in shifts in the predicted SPR wavelength of >10 nm.

In addition, these papers showed that the sharp absorption peak disappeared and the conductivity drastically increased by orders of magnitude for Au nanoparticle/SiO_2 composite thin films containing >60 vol% Au. This result supports our previous work with Ag nanoparticle/Teflon composite thin films. At. 60 vol% Ag concentration, where the Ag nanoparticles appeared to coalesce into a fully connected network approximating a bulk metal, strong absorption peaks were not observed.[10]

Our model considers smooth metal nanoparticles mostly free of sharp corners and edges. Some recent studies have shown the strong effect of edges and corners on the SPR wavelength of individual metal nanoparticles.[e.g. 24, 25] Nanoparticle spacing has also been shown to affect SPR wavelength.[26] In the study by Rechberger et al., the change in SPR wavelength was dependent on the polarization of the incident light, making it difficult to quantify spacing effects for randomly oriented nanoparticles in unpolarized light. The results showed that two neighboring Au nanoparticles interacted at spacings as great as 450 nm under certain polarization conditions.

CONCLUSIONS

A model for predicting surface plasmon absorption by randomly oriented, smooth metal nanoparticles supported in a dielectric has been developed from Mie and Maxwell-Garnett theories. The model allows prediction of the general absorption spectra from 2D images. In addition, the model provides insight into the methods needed to engineer thin film metal nanoparticle/dielectric systems for photovoltaic applications. The correct combinations of materials and metal nanoparticle aspect ratio distributions will yield thin films that absorb over the entire solar spectrum.

Uncertainty in the predicted spectra is due to the need to obtain 3D statistics from 2D TEM images. This point must be emphasized when using the model with metal nanoparticles of high aspect ratios. The effect is that absorption peaks are actually broadened toward longer wavelengths.

ACKNOWLEDGEMENTS

The authors acknowledge the support of the W. M. Keck Foundation and helpful discussions with Professor Robert G. Olsen.

REFERENCES

[1] D. J. Barber and I. C. Freestone, Archaeometry, **32**, 33 (1990).

[2] J. C. Maxwell-Garnett, Phil. Trans. Royal Soc. A, **203**, 385 (1904).

[3] G. Mie, Ann. Phys., **25**, 377 (1908).

[4] C. A. Foss, Jr., M. J. Tierney and C. R. Martin, J. Phys. Chem. B, **96**, 9001 (1992).

[5] R. Gans, Ann. Physik, **47**, 270 (1915).

[6] D. A. Genov, A. K. Sarychev, V. M. Shalaev and A. Wei, Nano Lett., **4**, 153 (2004).

[7] R. Elghanian, J. J. Storhoff, R. C. Mucic, R. L. Letsinger and C. A. Mirkin, Science, **277**, 1078 (1997).

[8] O. Sqalli, M.-P. Bernal, P. Hoffman and F. Marquis-Weible, Appl. Phys. Lett., **76**, 2134 (2000).

[9] D. M. Schaadt, B. Feng and E. T. Uy, Appl. Phys. Lett., **86**, 063106 (2005).

[10] H. Eilers, A. Biswas, T. D. Pounds, M. G. Norton and M. Elbahari, J. Mater. Res., **21**, 2168 (2006).

[11] V. M. Shalaev, Top. Appl. Phys., **82**, 93 (2002).

[12] K. C. See, J. B. Spicer, J. Brupbacher, D. Zhang and T. G. Vargo, J. Phys. Chem. B, **109**, 2693 (2005).

[13] K. Akamatsu and S. Deki, Nanostruct. Mater., **8**, 1121 (1997).

[14] H. Ma, P. Sheng and G. K. L. Wong, *Optical Properties of Nanostructured Random Media*, V. M. Shalaev Ed., Springer: New York (2002).

[15] C. A. Foss Jr., G. L. Hornyak, J. A. Stockert and C. R. Martin, J. Phys. Chem., **98**, 2963 (1994).

[16] S. Link, M. B. Mohamed and M. A. El-Sayed, J. Phys. Chem. B, **103**, 3073 (1999).

[17] K. S. Lee and M. A. El-Sayed, J. Phys. Chem. B, **110**, 19220, (2006).

[18] http://rsb.info.nih.gov/ij/index.html

[19] P. Mulvaney, Langmuir, **12**, 788 (1996).

[20] J. C. Ross and R. T. Dehoff, *Practical Stereology, 2nd Ed.,* Kluwer Academic/Plenum Publishers: New York (2000).

[21] H. B. Liao, R. F. Xiao, J. S., Fu, P. Yu, G. K. L. Wong and P. Sheng, Appl. Phys. Lett., **70**, 1 (1997).

[22] H. B. Liao, R. F. Xiao, H. Wang, K. S. Wong, and G. K. L. Wong, Appl. Phys. Lett., **72**, 1817 (1998).

[23] S. Mizuno, A. Verma, H. Tran, P. Lee and B. Nguyen, Thin Solid Films, **283**, 30 (1996).

[24] R. Jin, Y. Cao, C. A. Mirkin, K. L Kelly, G. C .Schatz and J. G. Zheng, Science, **294**, 1901 (2001).

[25] J. J. Mock, M. Barbic, D. R. Smith, D. A. Schultz and S. Schultz, J. Chem. Phys, **116**, 6755 (2002).

[26] W. Rechberger, A. Holenau, A. Leitner, J. R. Krenn, B. Lamprecht and F. R. Aussenegg, Optics Comm., **220**, 137 (2003).

APPENDIX

A. ONE-DIMENSIONAL CERAMIC NANOSTRUCTURES FOR CATALYSTS AND SENSORS

1. Introduction

One-dimensional (1D) nanomaterials are ideal for sensing and catalyst applications because of their large surface area to volume ratio, which results in orders of magnitude more reactive sites than thin films or bulk materials. For example, one cm^3 of material has 2000 times more surface area if processed into 10nm nanowires instead of a 10□m thick film. The greater number of reactive sites allows more external atoms, ions, and molecules to adsorb, which is essential for both catalyst and sensor applications. It also leads to enhanced sensitivity of 1D nanostructures compared to conventional thin film and bulk sensors. Most of the sensors described in this chapter function by measuring changes in resistivity (□) of the nanostructure when an outside species is adsorbed. The adsorbed molecule or atom locally affects the carrier density in a small volume of the nanostructure. Conventional thin film sensors work on a similar principle, however the change in □ is much more dramatic in nanostructures because the region where the carrier density is influenced by the adsorbate is on the same scale as the diameter of the nanostructure, causing orders of magnitude changes in □.

Beyond the fact that 1D nanostructures lend themselves to miniaturization, nanoscale materials often have dramatically different electronic properties relative to their bulk counterparts. For example, surface atoms can more easily switch between valence states. In the case of metal oxide 1D nanostructures, it is possible to create surfaces with a specific density of oxygen vacancies, which in turn have unique qualities that can be exploited for enhanced sensitivity or specificity.

The morphologies of 1D nanostructures makes them ideal for use in field effect transistor (FET) based devices, which have already been proven as an ideal setup for sensors and catalysts.[e.g., 1, 2] The small cross-sectional areas of 1D nanostructures allow them to be very effective gating elements in FET devices since outside molecules can drastically affect the resistivity of the 1D nanostructures. Furthermore, because they can have large aspect ratio (length/diameter), electrical leads are more readily made relative to zero dimensional nanostructures.

The detection levels of thin film sensors are typically on the order of 1 ppm.[3], where for nanowire sensors they are often in the ppb range and have recently been demonstrated to the fM level in the laboratory.[4-6] Conventional gas sensors, such as thin film SnO_2, are often only effective at temperatures > 450°C, while sensors using 1D nanostructures of SnO_2 are effective in detecting the same gases (NO_2, NH_3, and O_2) at temperatures < 200°C, which arises from their unique surface morphology.[7-11] Since thin film sensors almost always use polycrystalline materials, high operating temperatures lead to very short lifetimes because of grain growth, which in turn decreases sensitivity.[11]

The large surface areas of 1D nanostructures also makes them excellent candidates for catalysts because of their large number of potential reaction sites. As a point of reference, the surface area per mass of Si nanowires with mean diameters around 15nm has been calculated to be 115m^2/g, which is over 1000% larger than that of a 100nm thick Si film with 1□m x 1□m dimensions. Nanowire catalysts are often reusable and in some cases are more environmentally friendly than traditional catalyst materials. For example, expensive Lewis acids have been used in the past for for the formation of tetrazoles.[12] The use of Lewis acids results in large amounts of toxic and corrosive waste in addition to creating a dangerous environment for workers handling these acids.[13] Alternatively, nanocrystalline ZnO has been shown to be an inexpensive and efficient

catalyst for the formation of tetrazoles. Nanoscale catalysts offer improvements over conventional catalysts in many applications and may also have novel medical uses, such as drug delivery to specific cells and treatment of microbial infections, which are impossible with traditional approaches.[14] Efficient catalysts are also required before hydrogen-based fuel cells can become a cost effective alternative energy source. Current hydrogen production techniques are powered by fossil fuels and performed at high temperatures.[7, 12] Identification of an efficient low temperature catalyst is important in the search for a simple process to harvest hydrogen. Several 1D ceramic nanostructures including TiO_2 nanotubes, carbon nanotubes (CNT), MnO_2 nanowires, and CeO_2 nanowires have shown promise as catalysts for reactions associated with hydrogen generation.[15-18] These issues will be discussed in more detail in **Section 7.**

In this chapter, the term "ceramic" is defined to include all nonmetallic inorganic materials. Thus, CNT whose electronic properties are based on the chirality of the nanotube will be considered a ceramic. The landmark discovery of CNT in 1991 spurred a surge in research of 1D nanostructures and led to the development of a host of new materials and structures.[19] Our definition also includes materials such as GaN, which is a wide band gap semiconductor and glasses such as SiO_2. One-dimensional ceramic nanostructures have been demonstrated to be integral active components in advanced sensors and highly efficient catalysts. Some examples are listed in Table 1. One-dimensional ceramic nanostructures are also used as support structures for metallic nanoparticles in order to enhance reactivity, or to build in specificity. These hybrid nanosystems are very effective for the adsorption of gases, making them ideal for gas sensing and catalysis.[8, 15] For example, TiO_2 supports can increase the catalytic activity of Au

nanoparticle catalysts for the low temperature oxidation of CO.[20, 21] In this case, the TiO_2 substrate works in concert with the Au nanoparticles to enhance the process.

Table 1. Catalytic and Sensor Applications of 1D Ceramic Nanostructures

Ceramic	Form	Application	References
SnO_2	Nanowire, Nanobelts*	Sensor: CO, NO_2, O_2, H_2, ethanol	4, 8, 22
ZnO	Nanowire	Sensor: NO_2, NH_3, O_2, ethanol	12, 23-25
CeO_2	Nanowire	Catalyst: Oxidation of CO	26-28
TiO_2	Nanotube	Catalyst: Oxidation of CO	15, 20, 29
$ZnAl_2O_4$	Nanowire	Catalyst: Reduction of NO	30
Si	Nanowire	Sensor: NH_3, H_2O, DNA	31-33
Fe_2O_3	Nanotube	Sensor: H_2, H_2S, Ethanol	34, 35

*Nanobelts have similar dimensions to nanowires, except their cross sections are rectangular.

2. Ceramic Sensor and Catalyst Materials

Section 2.1 Sensor Materials

One-dimensional ceramic nanostructures have been identified as effective detectors for a wide variety of species. Tin dioxide is the most commonly used thin film and bulk sensor material and has been extensively studied as a 1D nanoscale sensor (see **Table 2).**

Table 2. 1D SnO_2 Nanostructured Sensors

Form	Species Detected	Detection Limit	References
Nanowire with Pd nanoparticles	H_2	10^{-3} torr	8
Nanowire with Pd nanoparticles	O_2	10^{-3} torr	2, 8
Nanobelt; nanowire doped with Ru	NO_2	0.1 ppm, 3 ppm at room temperature	3, 4, 9, 22, 36-38
Nanobelt	CO	200 ppm	4, 2
Nanobelt; nanowire doped with Sb	Ethanol	10 ppm	3, 4, 39, 40
Nanowire	N_2	Not demonstrated	2

Thin film and bulk SnO_2 sensors have shorter lifetimes and lower sensitivities than sensors based on SnO_2 nanowires and nanobelts due the present of grain boundaries and the lower surface to volume ratios. Since thin film SnO_2 sensors typically most efficiently in temperatures ranging from 350°C to 500°C, grain growth in the films limits the lifetime of the detector. In contrast, single crystal nanowire and nanobelt sensors are stable at high temperatures because they are single crystals.[41] An additional limitation of thin films sensors is their lower surface to volume ratios, which makes changes less apparent when an atom or molecule is adsorbed on the surface of the sensor.

Tin oxide nanobelts have been used as resistive elements in both simple circuit and FET configurations for sensing CO [2, 4], which illustrates the versatility of 1D nanostructures in terms of sensor design. The ability to design more efficient carbon monoxide sensors with 1D nanostructures could have significant societal impact. Carbon monoxide is an environmental pollutant and a highly toxic gas that is produced by the burning of common fuels. It is colorless, odorless and can be produced in household settings. Brief exposure to the gas can be fatal and those exposed to dangerous amounts are usually unaware until they experience symptoms of CO poisoning. For these reasons quick, efficient sensing of CO is important in areas where hazardous amounts of CO can be produced. When SnO_2 nanobelt sensors are exposed to CO, the gas molecules adsorb on the nanobelt surface. The nanobelts behave as n-type semiconductors andresistivity decreases significantly upon exposure to CO due to the formation of an adsorbate induced carrier depletion layer.[2, 4]

Nitrogen dioxide is another common air pollutant and toxin, where Sensing of this gas has important applications in environmental and household applications.[9] **Figure 1** shows the change in resistance of Ru-doped SnO_2 nanowires upon exposure to various concentrations of

NO_2 at room temperature. There is a measurable response down to concentrations as low as 50ppm.

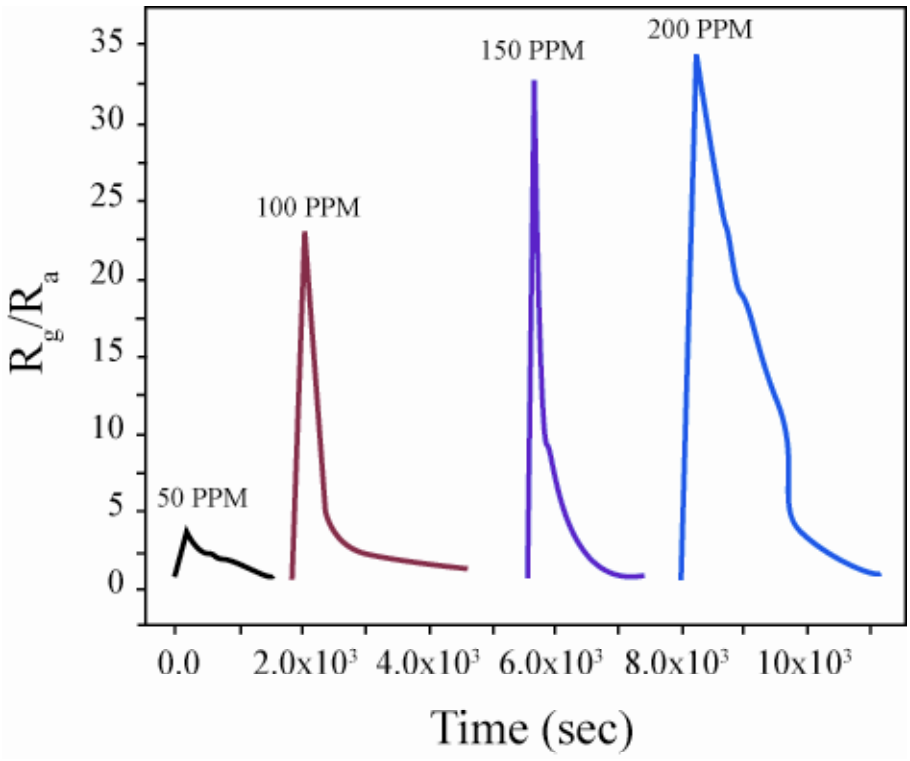

Figure 1. Change in resistance of Ru-doped SnO2 nanobelt sensors upon exposure to various concentrations of NO2 at room temperature. Data from Ref. 36.

Carbon nanotubes (CNT) are another 1D nanostructure that has been widely studied for use in gas sensors (**Table 3).** While CNTs are 1D nanostructures, their hollow structure results in unique electrical responses that differ from those of solid nanowires. CNTs come in two chiral flavors: conducting and semiconducting, which will obviously have distinctly different electrical properties. Because the chirality of CNTs is difficult to control, batch to batch variations in their electrical properties makes their commercial application in sensors problematic, i.e. a highly conductive sensor, as opposed to a semiconducting sensor. Furthermore, the electrical conductivity of CNT is affected by the number of graphene sheets that make up the CNT, but also the folding angle of the sheets.[42] This is further exacerbated by the inability to produce single batches of CNT with identical folding angles. Consequently, calibration of CNT-based sensors is nontrivial.

Table 3. Sensor Applications for CNT

Species Detected	**Detection Limit**	**References**
NO_2	50 ppb	43, 44
He	25 ppm	45
Ar	25 ppm	45
N_2	25 ppm	45
CO_2	25 ppm	45
O_2	25 ppm	45, 46
NH_4	25 ppm	45
H_2O (relative humidity)	0-100% in air	47
NH_3	Limit not determined	43
Alcohol vapor	1 ppm	48, 49
Nitrotoluene	0.3 ppm	44
Glucose	30 □M	50, 51
pH	Sufficient for all pH values	51
Cholesterol	Sufficient for human use	52, 53
Various proteins, biological molecules, and specific DNA sequences	nM levels in some cases	49, 54-59

In most of the studies listed in **Table 3**, the CNT were used as resistive elements in simple circuits and FETs. They can be used in a disordered manner, where electrode arrays are created and a liquid suspension of CNT is then placed over the electrodes and allowed to dry.[44] Alternatively, single CNT have been used as resistive elements.[48-50] In the case of vertically aligned CNT, the entire nanotube array often forms the working electrode in an electrochemical setup. [52, 54, 55] Reference and counter-electrodes are immersed in the solutions containing the species to be detected along with the CNT array. Amperometric measurements of the system of electrodes determine the sensing capabilities of the CNT arrays. This type of approach is commonly used when the tips of the CNT are functionalized for detection of a specific organic molecule (e.g., a protein). In all sensors using CNT as a resistive element an adsorbed species causes a change in □ of the device.

CNT-based gas sensors have been developed that utilize gas ionization in addition to resistivity changes.[45] A gas ionization sensor, using billions of vertically aligned CNT, is based on the principle that all gas molecules have a specific breakdown voltage. A varying electric field is applied to the CNT creating a large, uniform, field at the free ends. The measured current flowing through the nanotubes at each voltage is proportional to the amount of gas breaking down. After scanning a range of voltages, the relative amount of almost any gas present can be determined using tabulated breakdown voltages.

The advantage of the field ionization sensor is that low concentrations (down to the 10^{-7} mol.l^{-1} level.[45]) of individual gases can be identified with a single sensor. However, breakdown voltages of some gases common in air, such as NH_3 and O_2, can be very similar making sensitive detection of several individual gases difficult.[45] This type of sensor may be better equipped for

determining the presence of multiple gases in air with very distinctive breakdown voltages rather than detection of trace amounts of a specific gas.

Various other 1D ceramic nanostructures have been demonstrated as sensors as shown in **Table 4**. All the sensors listed in Table 4 had fast detection times and very high sensitivities. For example, In_2O_3 nanowire sensors showed a response time of < 5 s upon exposure to 1000 ppm of NH_3[60] , where the response time was defined as the period that elapsed before □ changed by an order of magnitude after exposure to the detected species; the response was more than an order of magnitude faster than that of thin film sensors currently used.[60]

Table 4. Examples of 1D Ceramic Nanostructure Sensors

Ceramic	Form	Species Detected	Detection Limit	References
Si	Nanowire	H_2O, NH_3, DNA, H_2O_2, glucose	<1000 ppm (H_2O, NH_3), 10 fM (DNA)	31-33, 61
Si/SiO_2	Nanowire	Biological molecules	pM levels	62
TiO_2	Nanowire	H_2, H_2O in air	<1 ppm (H_2), full range of relative humidity	42, 63
ZnO	Nanowire	NO_2, NH_3, O_2, ethanol	10 ppm (NO_2, NH_3), 1 ppm (ethanol)	23-25
V_2O_5	Nanobelt	NH_3, amines	30 ppb	64
Co_3O_4	Nanotube	H_2, ethanol	10 ppm	65
Fe_2O_3	Nanotube	H_2S, H_2, ethanol	10 ppm	34, 35
In_2O_3	Nanowire	NH_3, NO_2	ppb	5, 60

In terms of biological sensing, silicon-based nanowire sensors have been shown to exhibit with surface modification ultra specific detection of individual biological species . Proteins, catalysts, or complementary DNA sequences with specific structures were covalently or electrostatically bonded to the surface of the nanowire, which provided selective sites for the species to be detected. Other proteins and molecules present (i.e., those not intended to be sensed) did not attach to the surface of the nanowires. This type of approach could be invaluable for the treatment of cancer and other diseases where early detection is essential.[1] The ultimate limit of single molecule detection by sequence selective sensors may be realized with modified nanowire sensors in controlled environments.[1]

Similar types of selective sensing by surface modification has been performed with CNT, however Si nanowires offer the following advantages for selective sensing:

- There is a vast amount of knowledge on the surface science of Si and SiO_2 due to many years of research by the semiconductor industry.[e.g., 66-69]
- The exposed surfaces and electrical properties of Si and SiO_2 nanowires are usually identical among different growth processes.[e.g., 70-74] On the other hand, CNT from the same growth process can have different surface structures and electrical properties due to different wrapping configurations and the inner surface of the nanotube might interact with molecules and ions in the surrounding solution interfering with the sensing mechanism.

A major shortcoming identified with several 1D nanostructure-based sensors is the difficulty in achieving short recovery times. When the detected species is strongly attracted to the surface of the nanostructure successive detection procedures may be difficult to perform. The adsorbed

species do not readily desorb in a timely manner, particularly at low temperatures, and may in turn interfere with succeeding measurements. Two solutions for long recovery times have been identified:

- A large voltage pulse has been shown to cause desorption of NO_2 from the surface of ZnO nanowires.[23] A gate voltage of -60 V applied to a FET device for 60 s after exposure to 10 ppm of NO_2 causes the recovery of the detector in 4 minutes.

UV light may also be used to remove adsorbed species by thermal desorption.[7, 37, 44, 60] **Figure 2** shows the recovery of an ZnO nanowire based O_2 sensor when assisted by a UV light source

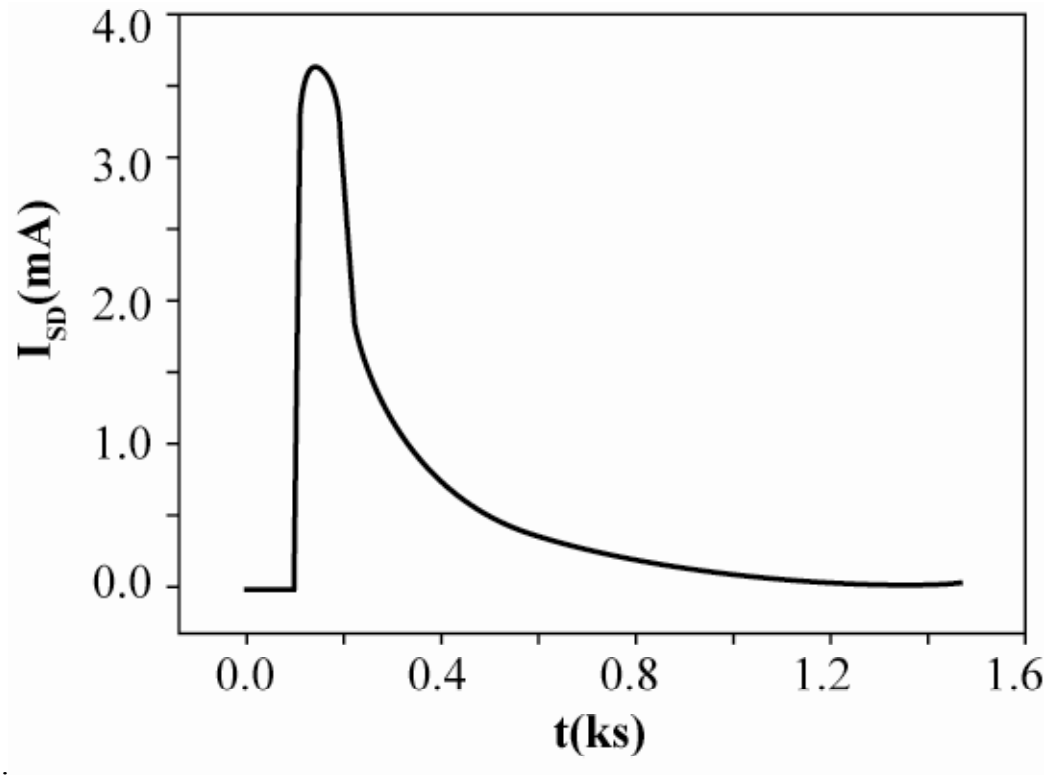

Figure 2. Change in detector current of a ZnO nanowire sensor upon exposure to O_2 at 0.1s, followed by recovery in less than 2s with assistance of a UV source. Data from Ref. 24.

Section 2.2 Catalyst Materials

One-dimensional ceramic nanostructures offer desirable alternatives to conventional catalysts for a number of different reactions as summarized in **Table 5.** One of the main advantages of using 1D ceramic nanostructures is that they are more active at low temperatures relative to thin films; TiO_2 nanotubes with Au nanoparticles are almost five times as catalytically active as conventional Au/Al_2O_3 catalysts for the oxidation of CO at 300°C.[15] This reaction is essential for the operation of hydrogen fuel cells. Ceramic nanostructures also offer stability in harsh environments. For example, reduction of NO_x gas species to N_2 and O_2 is an important reaction for environmental health due to the fact that NO_x gases are a primary cause of acid rain, a common by-product of the combustion of fuels in automobiles. Mats of $ZnAl_2O_4$ nanowires were found to effectively catalyze the reduction of NO_x vapors in typical automotive conditions and were thermally stable in these environments unlike traditional zeolite-based catalysts.[30]

Table 5. Catalysts Using 1D Ceramic Nanostructures

Catalyst	Form	Reaction	References
SnO_2	Nanowire	Oxidation of CO	2
TiO_2	Nanotube with Au nanoparticles	Oxidation of CO	15
ZnO	Nanobelt	Synthesis of 1H-tetrazoles	12, 75
CeO_2	Nanowire; nanowire with CuO and Rh nanoparticles	Oxidation; harvesting of H_2 from organic molecules	26-28, 76-78
C	Nanotube; nanotube with metal nanoparticles	Oxidation of CO; reduction of NH_3 to H_2; oxygen reduction reaction in direct methanol fuel cell	16, 79-81
MnO_2	Nanowire with Ag nanoparticles	Oxidation of CO	17
$ZnAl_2O_4$	Nanowire	Reduction of NO complexes to N_2 and O_2	30

Nanowires-based catalysts also provide a level of control of the catalytic process, which is very desirable for commercial processing. Tin oxide nanowire catalysts have been used in FET devices in the same manner as SnO_2 sensors.[2] The advantage of using the nanowire catalyst in this case is the ability to start and stop the reaction by controlling the gate voltage. The gate voltage affects the amount of O_2 adsorbed on the nanowire surface. At negative gate voltages there are few electrons available in the n-type nanowires, which results in the adsorption of very few oxygen molecules. The lack of oxygen molecules essentially stops the oxidation of CO.[2]

Simple metal oxides form the majority of 1D ceramic nanostructures studied for catalysis. These materials were studied due to their ease of synthesis, low cost, and known functionality (at least in bulk form). There remains a vast amount of research to be done using nanowires of more complex ceramics, which may actually function better than many of the materials listed in Table 5. For example, one study has shown that the lanthanide hydroxide ceramics, e.g., $Pr(OH)_3$, $Nd(OH)_3$, and $Yb(OH)_3$, can be predictably synthesized as nanowires using a solvent growth method and have potential as catalysts due to the many possible transitions within their 4f subshells. [82]

3. Growing 1D Nanostructures

The ability to produce arrays of 1D nanostructures is essential for catalyst and sensor applications. Simple processing methods, such as evaporation in a gas flow furnace, can produce high yields of structurally and physically similar nanowires of ceramics such as Si_3N_4, Ga_2O_3, ZnO, SiC, and SiO_2.[e.g., 83, 84] Growth processes that result in high product variability, for example in nanowire diameter, are not in general suitable because sensors formed from these materials will often have unpredictable behavior. Conventional sensors and catalysts are often produced using methods that yield products with a wide distribution of grain sizes and grain

orientations (i.e., different crystallographic planes are exposed), which makes these devices inherently inefficient. For example, SnO_2 thin film sensors must be carefully manufactured and annealed in an attempt to reduce grain growth and enhance sensitivity.[85] An ongoing challenge is to develop controllable growth processes for forming 1D nanostructures, ideally in useful quantities.

Over the past decade and a half, several techniques for the synthesis of 1D nanostructures have been developed. Each of the approaches described in this chapter offers at least one promising aspect for the formation of 1D nanostructures for catalysts and sensors. As is the case with most nanomaterials, there are issues associated with each process that must be resolved before nanowires can be mass-produced economically for these applications.

The first techniques described rely on the anisotropic nature of the nanowire, nanotube, or nanobelt to drive 1D growth. Many involve the classic vapor-liquid-solid (VLS) growth mechanism, which was first proposed by Wagner and Ellis in 1964 to describe the formation of Si whiskers.[86] In the conventional description of this mechanism, a liquid catalyst particle on a solid substrate is the preferred site for absorption of the vapor from the source material or precursor. According to early descriptions of the VLS mechanism, the catalyst particles must have a low melting temperature (T_M) relative to the desired growth temperature. This was often achieved by the presence of alloying elements in the vapor, generated from the source material, which would form a liquid alloy droplet. The conventional VLS mechanism is ideal for 1D nanostructure formation because the growth temperature can usually be predicted using a binary or pseudo-binary phase diagram.[87] In order for nanowire growth to occur, there must to be a region on the phase diagram where the catalyst is a liquid and the desired 1D nanostructure

material can exist as a solid. The solid phase will then precipitate out as the catalyst becomes supersaturated with species from the vapor.

One-dimensional nanostructures produced via the VLS mechanism are usually either single crystalline or a glass. In the original description of the VLS mechanism, the catalyst droplet remains at the top of the wire as shown in **Figure 3.** Growth proceeds until either the conditions change, often when the catalyst particle grows far enough away from the hot substrate that it solidifies or the vapor source is terminated. However, it has been demonstrated that 1D nanostructures can form out of the top of the catalyst particle as it remains in contact with the substrate.[e.g., 88] CNT have been grown both with the catalyst particles at the top of the nanotubes and also with the catalyst particle remaining attached to the substrate. It is believed that the catalyst remains in contact with the substrate when the substrate-particle interaction is strong. If the interaction is weak, the nanotube forms at the substrate with the catalyst particle being carried atop the nanotube. In either case, the diameter of the catalyst droplet is directly proportional to the diameter of the nanowire, making the process of forming the catalyst particles very important.

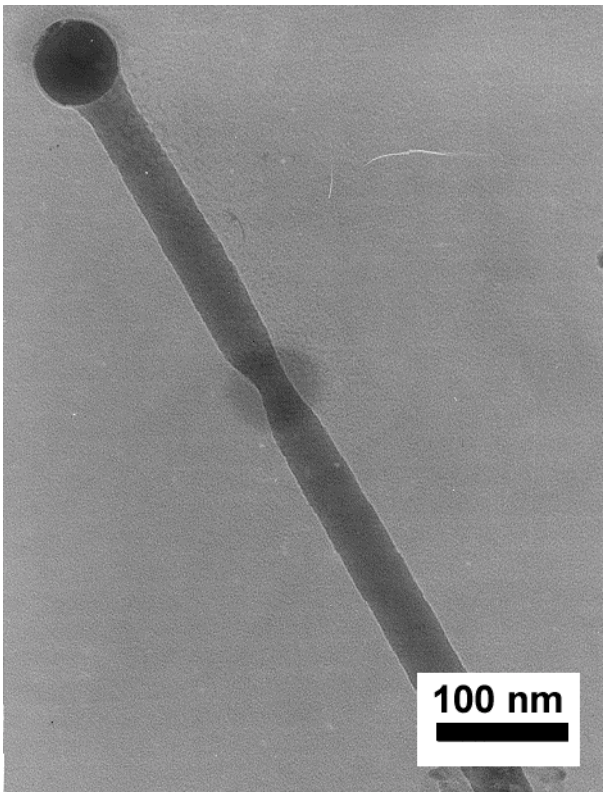

Figure 3. TEM image of an SiC nanowire formed by the VLS mechanism with an Au catalyst particle.

In the last two years, studies have indicated that the catalyst does not have to be liquid during the growth process in order to catalyze nanostructure formation.[89, 90] These studies have shown that the catalyst particles and source vapor form a solid solution and that nanostructure growth actually terminates when the catalyst particle is liquid. For example, GaAs nanowires can be formed using solid Au catalysts.[89] X-ray energy dispersive spectroscopy (XEDS) indicated that only the Ga atoms were soluble in the Au, and the GaAs nanowires actually formed by a chemical reaction between the Ga nanowires and As vapor. In the case of InAs, nanowires did not form in the temperature range where InAs and liquid Au are in equilibrium. They only formed below T_M of the Au nanoparticles.[90] Collectively these recent studies have led to a newly proposed growth mechanism: the vapor-solid-solid (VSS) mechanism.

In some VLS and VSS growth processes, graphite is mixed in with the powdered source material to lower the growth temperature. The process is referred to as carbothermal reduction and may be employed when growing 1D nanostructures of oxides that sublime at high temperatures, e.g., SnO_2, Al_2O_3, Ga_2O_3, or ZnO. [91-96] Highly volatile intermediate species, such as AlO, SnO, or Zn vapor are formed when the graphite reduces the source powder during heating. The graphite powder is typically mixed in 1:1 or 1:2 ratios with the source material. The carbon source can also be CNT.[96]

Nitride nanowires such as AlN, GaN, Al_3N_4, and BN can be formed using carbothermal reduction.[96] [This process is widely used to produce powders of non-oxide ceramics such as AlN.] A mixture of NH_3 and Ar is typically used as the flow gas. The graphite reduces the oxide powders and the reactive intermediates combine with NH_3 to form nitrides.

3.1 Vapor Processes

Simple evaporation of a powder source is a commonly used approach to fabricate nanowires and nanobelts as shown in **Table 6**. In this process the source is heated in a furnace or locally with a laser or electron beam to cause sublimation. A flow of inert gas, typically Ar, is used to carry the sublimated source to the heated substrate. The morphology of the product depends on several factors. For example, the substrate temperature can determine whether nanowires or nanobelts form.[e.g., 97].

Table 6. Evaporation Methods for 1D Ceramic Nanostructures

Ceramic	Form	Process	References
SnO_2	Nanobelt; nanowire	Nanobelt: oxide powder in Al_2O_3 tube furnace 1350°C, 0.04 MPa, 2h Nanowire: Sn and Sb powders mixed in 10:1 ratio and evaporated in Al_2O_3 tube furnace 900°C; Au catalyst particles on Si substrates.	4, 36-40, 98-101
ZnO	Nanobelt; nanowire	Nanobelt: oxide powder in Al_2O_3 tube furnace 1400°C, 0.04 MPa, 2 h. Nanowire: oxide powder evaporated in tube furnace 950°C; Au catalyst particles.	91, 98, 101, 102
In_2O_3	Nanobelt; nanowire	Nanobelt: oxide powder in Al_2O_3 tube furnace 1400°C, 0.04 MPa, 2 h. Nanowire: laser ablation of In in Ar/O_2, 770 °C.	98, 103
CdO	Nanobelt	Oxide powder in Al_2O_3 tube furnace 1000°C, 0.04 MPa, 2 h.	98
Ga_2O_3	Nanobelt	GaN powder in Al_2O_3 tube furnace 950°C, 0.04 MPa, 2 h.	98
ZnS	Nanowire; nanobelt	ZnS powder evaporated in Al_2O_3 tube furnace, Si substrates. Nanobelts: 950-1000°C. Nanowires: 900-950°C.	97
PbO_2	Nanobelt	PbO powder evaporated in tube furnace 950°C, 300 torr, 1 h.	104
SeO_2	Nanobelt	Simultaneous evaporation of Zn powder at 600°C and Se powder at 370°C in quartz tube furnace.	105
Mn_3O_4	Nanowire	$MnCO_3$ and NaCl powders 800 – 900°C, 3 h.	106
InP	Nanowire	Laser ablation of InP, Si substrates, Au catalyst particles, 650-700°C.	107
Si	Nanowire	MBE from Si powder at 525°C .	108

Evaporation offers several advantages:

- The process is relatively simple to set up and repeat, especially when catalyst particles are used. Only a tube furnace with inert gas flow is required.
- Growth times are usually fairly short compared to some other techniques. One dimensional nanostructures form in ~2h.[e.g., 93, 98]
- By using different substrate temperatures it is possible to change the form of the nanostructure [e.g., 94]. Although, in the case of nanobelts, it can be difficult to control the dimensions.

Copper oxide nanowires and SnO_2 nanobelts have been formed by direct oxidation of a metal source.[109, 110] This process differs from other evaporative methods because no heterogeneous substrate is needed to support nanowire formation. Tin oxide nanobelts were formed by oxidation of tin powder mixed with $Fe(NO_3)$ in the range of 1080 to 1250°C.[110] The $Fe(NO_3)$ powder aided in nanobelt formation; the VLS mechanism was not believed to be operative. The CuO nanowires formed directly on copper wires, grids, and foils by the VS mechanism when heated to temperatures ranging from 400-700°C. The higher growth temperatures resulted in nanostructures with smaller cross sectional areas and a narrower size distribution.[109, 110] The CuO nanowires grew in the <111> direction and had a twin plane along their entire length. (The mechanism leading to twinning was not determined.) It would seem to be possible to grow other 1D ceramic nanostructures using this technique. Although this simple process could be used to produce device ready substrates with 1D nanostructures attached for sensor or catalyst use, the preferential nucleation and growth on ledges and corners would be limiting.

Chemical vapor deposition (CVD) is often used in cases where it is difficult to sublimate the pure source material. **Figure 4** shows a dense array of GaN nanowires formed by CVD. Precursor powders or gases (organometallic molecules with low boiling temperatures are the most common precursors) may be expensive, but they often require much lower temperatures to provide ample reactants for nanostructure formation. For example, Si and SiO_2 nanostructures can be formed at temperatures much lower than the T_M of the pure Si.[111, 112] Silicon nanowires have been formed at temperatures as low as 120°C using hot filament CVD. A further example is the formation of B_4C nanowires, which has been achieved using plasma enhanced (PE) CVD in the temperature range 1100-1200°C: T_M of boron and carbon are approximately 2075°C and 3525°C respectively. The first observation of nanosprings was made on samples produced by PECVD.[87, 113, 114] **Figure 5** shows a TEM image of an amorphous boron carbide nanospring.

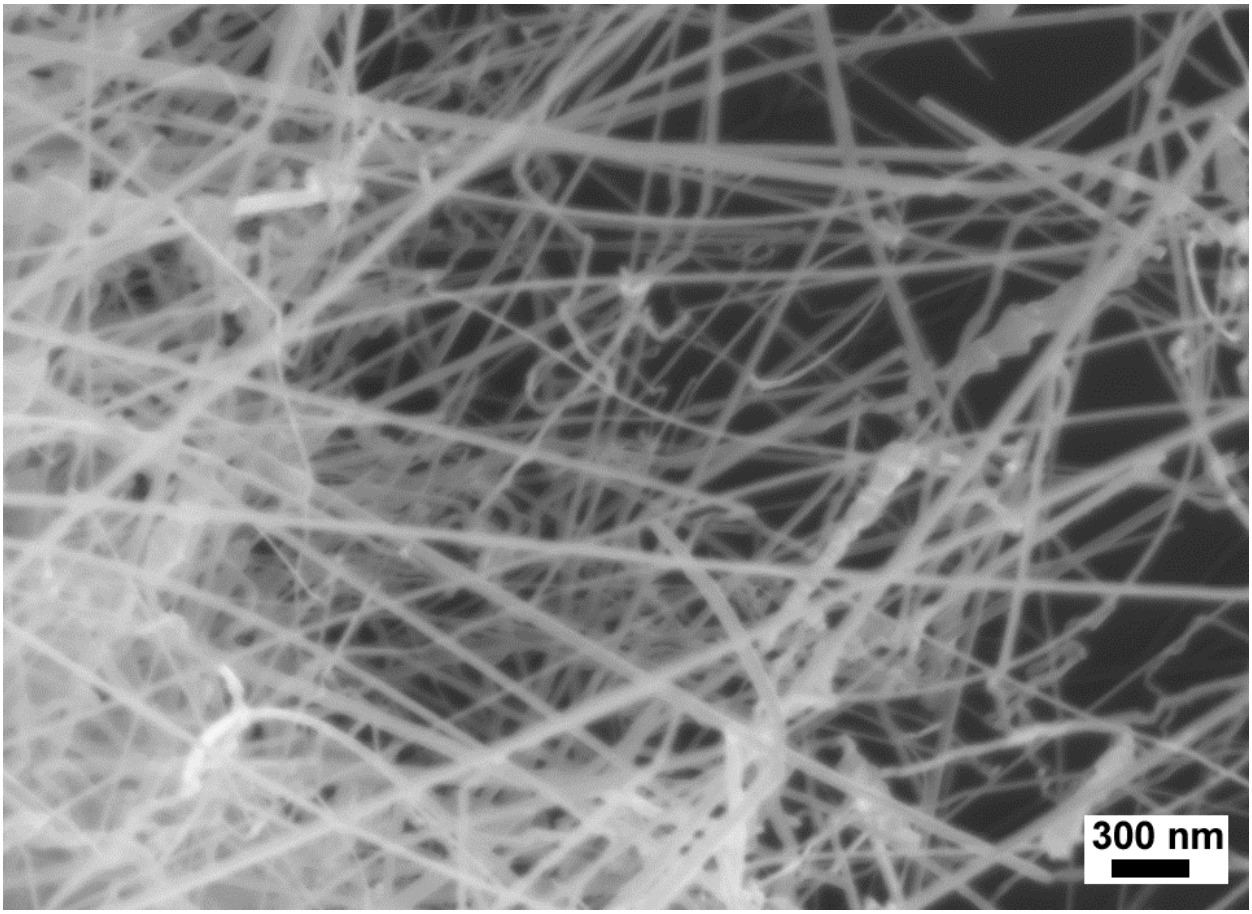

Figure 4. SEM image of a mat of GaN nanowires formed by PECVD. Reprinted with permission from Ref. 115, V. Dobrokhotov, D.N. McIlroy, M.G. Norton, A. Abuzir, W.J. Yeh, I. Stevenson, R. Pouy, J. Bochenek, M. Cartwright, L. Wang, J. Dawson, M. Beaux and C. Berven

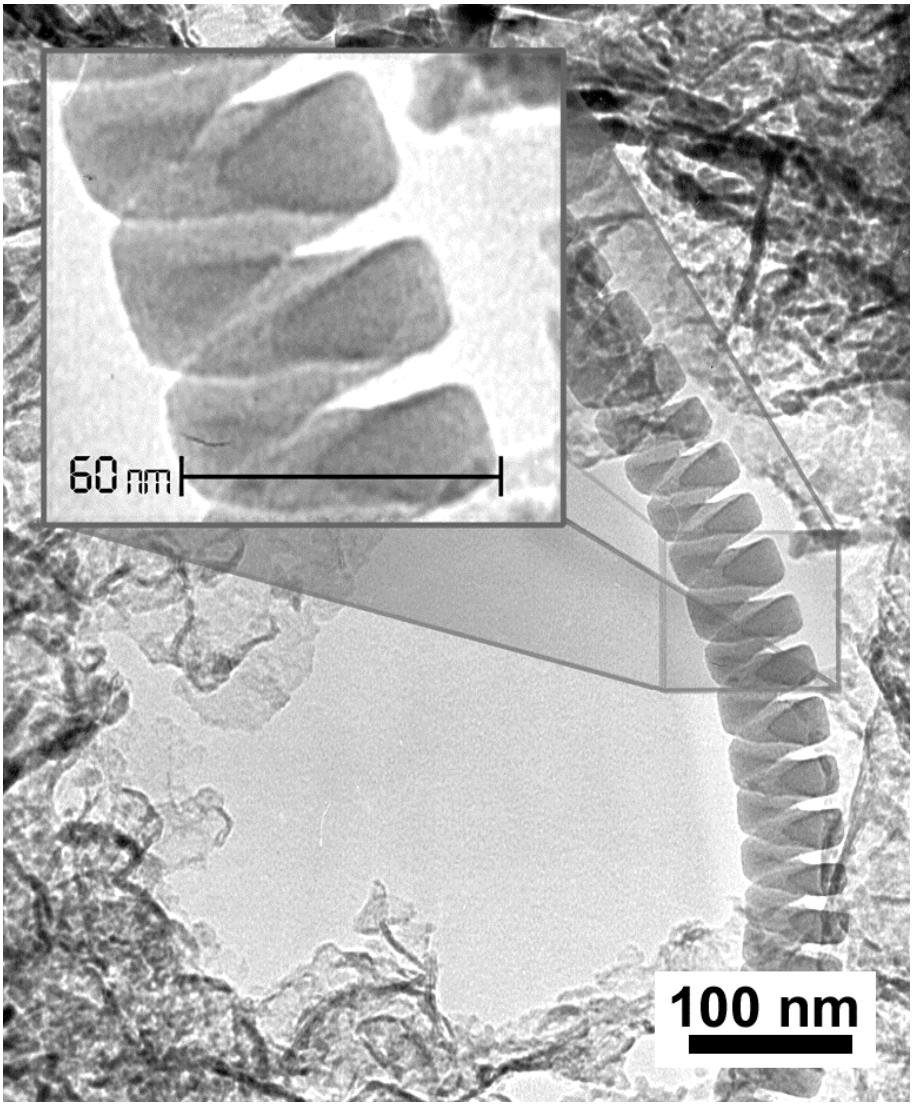

Figure 5. Bright field TEM image of an amorphous BC nanospring. Reprinted with permission from Ref. 115, D. N. McIlroy, D. Zhang, Y. Kranov and M. G. Norton, Appl. Phys. Lett., 79, 1540 (2001). Copyright @ American Institute of Physics.

Table 7 lists some of the 1D ceramic nanostructures that have been successfully grown by CVD.

Table 7. 1D Ceramic Nanostructures Formed by CVD

Ceramic	Form	Catalyst	Process	References
B_4C	Nanowire	Fe	PECVD at 1100-1200°C with $C_2B_{10}H_{12}$ precursor .	115, 116
Si/SiO_2	Nanowire; nanotube (SiO_2)	Ti, Au	Si/SiO_2 nanotube: reducing $SiCl_4$ in Ar/10% H_2 at 900-950°C and subsequent oxidation in O_2 at 800-1000°C yielded Si nanowire core/SiO_2 sheath Si nanowire: $SiCl_4$ reduced by H_2 in tube furnace	111, 112, 117, 118
BN	Nanotube	Ni_2B, NiB Co, Ni	Multiwalled nanotubes formed on SiO_2 from $B_3N_3H_6$ precursor in tube furnace 1000-1100°C.	119
SnO_2	Nanowire, hollow nanobelts	Ti, Cr, Fe, Co, Ni, Cu, Ni, Mb, Pa, Ag, Ta, W, Ir, Pt, Au, and Al	SnO or Sn powder heated to 850-1150°C in tube furnace. Ar carrier gas with traces of O_2 deposited precursor on SiO_2 substrate.	2, 76, 120
ZnO	Nanowire	Au	ZnO powder precursor 850-1150°C in tube furnace. Ar carrier gas with traces of O_2 deposited precursor on sapphire substrate.	118
GaN	Nanowire	None	Ga layer deposited on Si substrate, quartz boat, 900°C in NH_3	121
SiC	Nanowire, nanospring	NiB	PECVD using $C_2B_{10}H_{12}$ precursor. Si substrate 980-1100°C, 1.5 sccm of Ar during deposition.	111, 113
BC	Nanowire, nanospring	NiB, FeB	PECVD using $C_2B_{10}H_{12}$ precursor. Si substrate 980-1100°C, 3 sccm Ar .	87, 114
GaP	Nanowire	None	Tube furnace 1000°C Ar atmosphere. Quartz tube of Ga_2O and CNT and alumina crucible of P powder downstream of high temperature zone.	95
In_2O_3	Nanowire	Au	Laser ablation of In target in Ar and O_2, 770°C.	103

3.2. The Role of the Catalyst

Many CVD and evaporation processes for the growth of 1D ceramic nanostructures rely on the VLS mechanism, although the process can be used without catalysts under certain conditions.[109, 111, 116, 123] Where the VLS mechanism is operative, the catalyst particles play an important role in the growth process and can affect growth morphology, crystallographic growth direction, and diameter of the product.[e.g., 121, 124, 125] As a general rule, a catalyst with a lower T_M will yield a higher product density on the substrate. For example, Ta (T_M = 3017°C) catalyst particles have been shown to result in much lower growth densities than Au (T_M = 1065°C) particles for SnO_2 nanowires grown by evaporation.[121] The proposed explanation for this observation is related to the greater number of nanoparticles formed and the increased fluidity of the catalyst particles with the lower T_M.

It has been observed that the crystal structure of the catalyst particle can affect the morphology of the resultant 1D nanostructure.[121] For example, the growth of SnO_2 nanowires by carbothermal reduction yielded isolated islands of nanowires and nanoparticles on the substrate if the catalyst had the BCC crystal structure (e.g., Cr, Mo, Nb, Ta, and W); metal catalyst particles with the FCC crystal structure (e.g., Cu, Al, and Au) produced a uniform mat of randomly aligned nanowires. The reason for this effect is complex and is not yet fully understood. However, this explanation only makes sense for VSS mechanism since in the VLS process the catalyst is in the liquid phase and the crystal structure of the solid is irrelevant. The explanation for this catalyst specific growth may be related to the interaction of the catalyst with the substrate, which will depend on whether the material is BCC or FCC.

A striking illustration of the importance of the catalyst in determining the morphology of 1D nanostructures is the growth of nanosprings. The model, which is based on contact angle anisotropy (CAA), requires that the center of mass of the catalyst droplet is not aligned with the center of mass of the nanostructure during growth as illustrated in **Figure 6**. [87, 113, 114] The surface tensions (□ associated with the displacement (□) of the catalyst particle produce anisotropy in the work of adhesion (W_A) across the nanowire-catalyst interface. This anisotropy is significant because the probability of an atom in the catalyst particle attaching itself to a point at the interface is a function of the energy required to break a catalyst-nanowire bond, minus the energy gained by making a new bond to the nanowire. The probability is higher for lower values of W_A hence it is expected that an atom will be more likely to attach at position B in Figure 6 creating the asymmetry necessary to curl the growth trajectory. Nanosprings are the result.

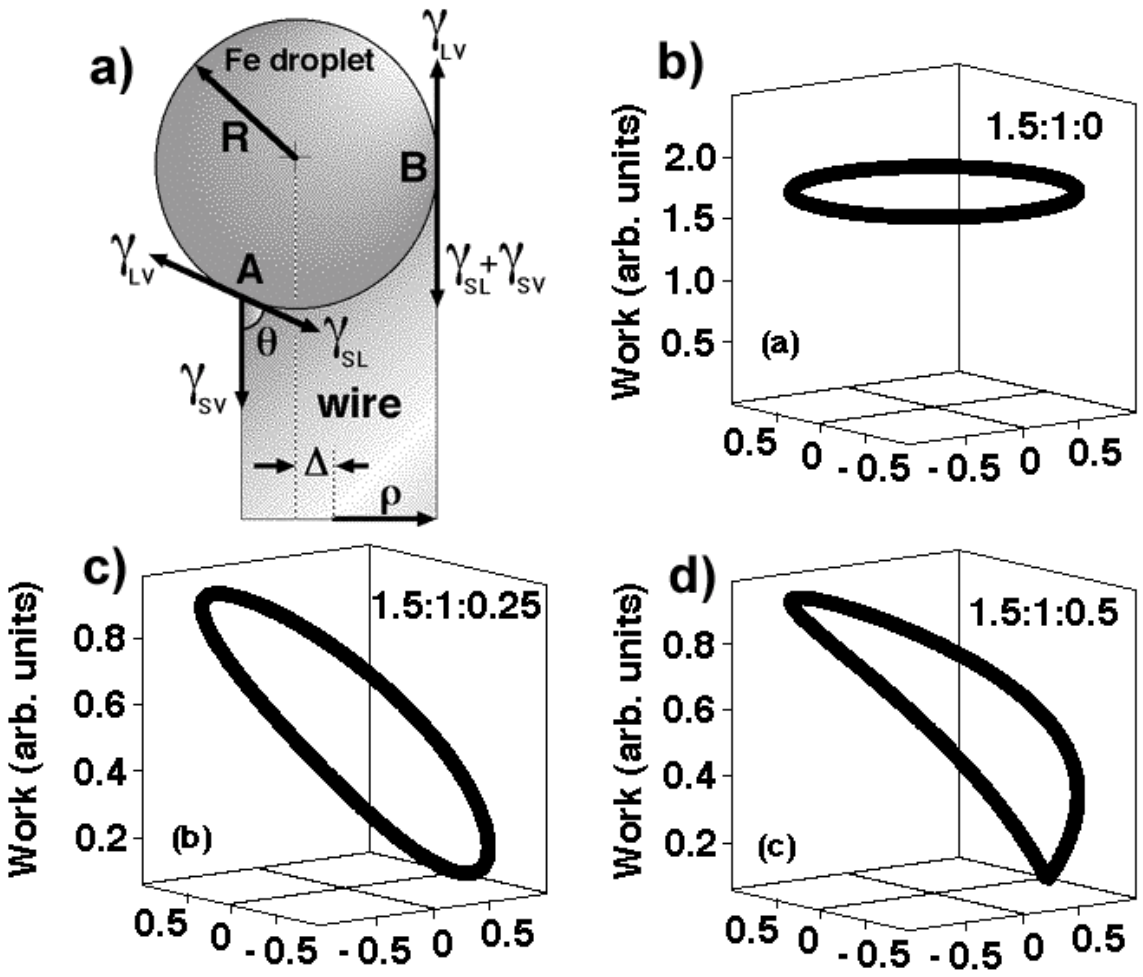

Figure 6. (a) Schematic of a spherical Fe catalyst particle located asymmetrically atop a forming nanowire and the corresponding surface tensions; (b) Work of adhesion of a spherical catalyst particle located symmetrically atop a forming nanowire, (c) Catalyst particle slightly off axis, (d) When the catalyst is located far off axis. Redrawn after Ref. 87.

The size of the catalyst particle is important in defining the size of the resultant nanostructure. Unfortunately, the relationship is not straightforward and depends on the specific combination of materials and is best determined through experimentation: even then correlations can be tenuous. Examples from the literature illustrate some of the trends.

- GaP nanowires grown by laser catalytic growth (LCG) had diameters that were slightly larger to the diameter of the Au catalyst nanoparticles.[124] The average diameters of the nanoparticles were 8.4, 18.5, and 28.2 nm; the corresponding nanowire diameters were 11.4±1.9, 20.0±1.0, and 30.2±2.3 nm, respectively.
- Si nanowires formed by CVD had average diameters of 20.6±3.2, 24.6±4.0, 29.3±4.5, and 60.7±6.2 nm corresponding to Au catalyst particles of 15.3±2.4, 20.1±3.1, 25.6±4.1, and 52.4±5.3 nm respectively.[119]
- Boron nitride nanotubes formed by a CVD with NiB catalyst particles had diameters ranging from a few nm to tens of nm, while the NiB catalyst particles had a diameters on the order of microns.[120]

In general, to produce 1D nanostructures it is desirable (and often necessary) to have nanosized catalysts and several methods have been developed for generating such particles. These methods overcome the thermodynamic limitations associated with nanometer-sized particles. There is a minimum size, r, possible for a liquid particle according to free energy considerations

$$r = \frac{2\gamma_{LV} V_L}{RT \ln \sigma} \qquad (1)$$

γ_{LV} = liquid-vapor interfacial energy

V_L = molar volume of the liquid

□ = vapor phase supersaturation

R = gas constant

T = temperature

Values of r for the metals commonly used as catalysts are on the order of microns.[126] However, various approaches have been used to create nanometer-sized catalyst particles. Laser ablation of a thin film is a simple, quick way of creating nanometer-sized catalyst particles. [5, 103, 127] However, it can be difficult to control the average size of the particles using this technique, which can result in a broad size distribution of 1D nanostructures. This in turn, may lead to a variation of properties among products from a single growth process, which is undesirable for device manufacturing.

If an evaporation-based growth process is used, small particles of the catalyst can be incorporated directly into the source material. A laser can be used to vaporize the source and catalyst in a single-step process: LCG.[107, 124, 128-131] LCG and has been used to form nanowires of many ceramics including GaAs, GaP, InP, and GaN [e.g., 107, 124, 129, 132] and Si and Ge nanowires with narrow size distributions (standard deviation < 1nm.[130]

Nanometer-sized catalyst particles for VLS growth have been created using solution methods.[e.g., 91, 133] In one process, polystyrene spheres suspended in a liquid were deposited on a substrate in a close packed array by dripping the suspension on a substrate and allowing it to dry. A metal was then deposited onto the substrate surface and the polystyrene spheres washed away. The metal remained in only those areas where the polystyrene spheres were absent. Vertically aligned ZnO nanowires were grown in a hexagonal array at the remaining catalyst sites.[91] In a simpler process, the catalyst was distributed on a substrate by simply pulling it

through a suspension containing nanometer-sized particles.[133] The disadvantage to this latter method is that the catalyst particles are often distributed unevenly on the substrate surface. The addition of a surfactant (e.g., a block copolymer) can create suspensions of metal nanoparticles that can be evenly distributed on a substrate.[134]

3.3 Solution Processes

Solution growth describes a wide variety of fabrication methods, which are usually characterized by the use of a pressurized and heated solution. **Table 8** lists a number of approaches that have been used to form 1D ceramic nanostructures. These processes may require multiple steps and solution-based methods are generally harder to predict than their vapor-based counterparts.

Table 8. 1D Ceramic Nanostructures Formed from Solution

Ceramic	Form	Process	References
SnO_2	Porous nanowire; nanowire	$SnC_2O_4.H_2O$ mixed with poly(vinylpyrrolidone) in ethylene glycol, 3 h, 195°C.	11, 134
CdS	Nanowire	Cd^{2+} distributed in polyacrylamide and treated with thiourea (NH_2CSNH_2) in ethylenediamine at 170°C or mixed with S^{2-} in ethylenediamine and heated to 195°C for 24 h.	135, 136
InP	Nanowire	Precursor ({t-Bu_2In[□-P($SiMe_3$)$_2$}$_2$) and methanol suspended in toluene and stirred for 10 h. Suspension then heated for 24 h at 111-200°C.	137
Ge	Nanowire	Ge precursors (tetraethylgermane and diphenylgermane) mixed with alkanethiol-coated Au catalysts suspended in cyclohexane. Nanowire formation performed in a titanium	138

		cell at 300-450°C, 4.2 MPa, 8-20 min.	
MnO_2	Nanowire	Solution of manganese sulfate and ammonium persulfate heated in a Teflon-lined autoclave, 120°C, 12h. Ammonium sulfate resulted in □-phase.	139
WO_3	Nanowire bundles	Tungstic acid (WO_3xH_2O) mixed with Li_2SO_4 in oxalic acid and heated in an autoclave, 180°C, 2-24 h.	140
CdSe	Nanowire	Cd and Se precursors dissolved in a mixture of trioctylphosphine oxide and hexylphosphonic acid, heated to 300°C, 30 min.	136, 141
TiO_2	Nanotube; nanobelt	TiO_2 sol-gel treated with 10M NaOH, 20h at 110°C then 0.1M HCl added.	142, 143
Si	Nanowire	Si precursor (dihpynylsilane) and Au catalysts suspended in hexane, 500°C.	132
$ZnAl_2O_4$	Nanowire	Precursors of Zn and Al combined with NO_3, mixed in water and heated 180-200°C, 20 h.	30
V_2O_5	Nanobelt	V^{5+} ions suspended in H_2O condensed into nanobelts by heating at 200°C, 48 h.	64
ZnO	Nanowire	Zinc nitrate hexahydrate ($Zn(NO_3)_2.6H_2O$) and methenamine ($C_6H_{12}N_4$) mixed in H_2O at 1 mM concentration, 95°C for several hours.	144
CeO_2	Nanotube	Cerium nitrate added to H_2O and heated to 100°C. Ammonia hydroxide added and solution cooled after 3 min. Samples aged for 45 days to yield nanotubes.	145
Lanthanide series hydroxides: $Ln(OH)_3$	Nanowire	Ln_2O_3 dissolved in nitric acid and KOH. Precipitate formed and mixture stirred for 10 min before being added to H_2O in autoclave and heated, 180°C, 12 h.	82

One dimensional nanostructures have been formed using sol-gel processes.[e.g., 143] This method is similar to that used to produce ceramic nanopowders. Hydrolysis produces a suspension of particles, which then aggregate to form a gel. It is during thermal treatment of the gel that 1D nanostructures, rather than nanopowders, can be produced. Colloidal suspensions have also been used as precursors to form 1D nanostructures in solution-based processes.[e.g., 141]

CdS nanowires with high aspect ratios have been formed using a solution containing Cd^{2+} ions and a polyacrylamide gel.[136] In this procedure $Cd(NO_3)_2$ was dissolved in deionized water and mixed with a polyacrylamide gel. The resulting solution was dehydrated and placed in an autoclave with thiourea. The autoclave was held at 170°C for 10 days. Although solution-based techniques are not as predictable for forming 1D nanostructures as vapor-phase processes they do offer some advantages:

- Reactions in solution usually occur at much lower temperatures than vapor processes. For example, SnO_2 nanowires grown by solution method have been produced at 200°C, while 1D SnO_2 nanostructures produced from the vapor usually require temperatures ~ 1000°C.[39, 40, 135]
- The phase can be controlled. For example, MnO_2 nanowires have been grown by a nearly identical solution approach in both □ and □ forms.[140] The nanowires formed initially in the □ phase and could be converted into the □ form by addition of a small amount of ammonium sulfate before heating. The phase often impacts the detection limit of sensors or the efficiency of a catalyst, making phase control an important aspect of 1D nanostructure device fabrication.

- The growth direction and the Miller indices of the exposed sidewall planes can be controlled. Silicon nanowires formed by a solution method were found to primarily grow in the <100> direction when the pressure was 0.027 MPa, whereas the nanowires grew in the <110> direction when the pressure was increased to 0.036 MPa.[133] Si nanowires typically grow in <111> direction in vapor processes.[119] These results are likely due to surface energy considerations. The interaction between the nanostructure and the solution is very different than that between the nanostructure and a vapor environment. Controlling growth direction may be critical in sensing and catalysis where specific crystallographic planes are required for optimal detection and efficiency.

A huge drawback for many of the current solution methods is the amount of time required to grow 1D nanostructures. The growth times demonstrated in several studies are not feasible for efficient production of devices. For example, V_2O_5 nanobelts grown by a solution method at ambient temperature took 3 months to form.[64] In several studies 1D nanostructures formed by solution growth took > 10 h. [135, 140, 141] Increasing the temperature and pressure of the solution may drastically reduce the formation time. High aspect ratio Ge nanowires have been grown in less than 20 minutes in solution by keeping the temperature of the solution between 350 and 400°C and holding the pressure between 13 and 40 MPa.[139]

The growth mechanisms leading to formation of 1D nanostructures by solution methods vary widely. Metal particles can be used to catalyze growth in a process very similar to the VLS mechanism, often referred to as solution-liquid-solid (SLS) synthesis. Catalyst particles are dispersed in the solution along with the source material and become supersaturated, leading to precipitation. Germanium, InP, and Si nanowires have all been grown via this mechanism.[133, 138, 139] One dimensional nanostructures can be formed from solution with the aid of functional

molecules that direct self assembly.[136, 141, 143] For example, WO_3 nanowires formed in solution only in the presence of Li_2SO_4. Nanoparticles of WO_3 were formed in the absence of Li_2SO_4. It is generally accepted that functional molecules in a solution bind to certain sites on the reactant ions or particles, thereby allowing only those regions to join together. Consequently, this process allows nanostructures to be grown in orientations not possible by vapor-phase processes.

Solution processes may produce 1D nanostructures without the aid of catalyst particles or heterogeneous molecules.[11, 82, 13, 140] These growth processes rely on preferential formation due to the anisotropic nature of the crystal structure. Solution growth using this approach is often a very precise and delicate process. Nanowires of SnO_2 were formed from a complex solution comprising hexanol and heptane with $Sn(OH)_6^{2-}$ only when the concentration of $Sn(OH)_6^{2-}$ ions was > 0.03M.[135]. $Sm(OH)_3$ nanowires were formed by solution growth only when the pH of the solution was over 9, however the aspect ratio of the nanowires was an order of magnitude lower when the pH of the solution was 14.[82] These results indicate that formation of 1D nanostructures with exact dimensions may be possible through solution growth, but processes that do not use catalysts or functional molecules are often difficult to control.

3.4 Template Assisted Growth

Templates can be used with either vapor or solution growth processes to create ordered arrays of 1D nanostructures. This approach makes device fabrication on a substrate much simpler than relying on the placement of single 1D nanostructures. Several different templates have been used and anodized aluminum templates (AAT) are one of the most widely used types as shown in

Table 9. 1D Ceramic Nanostructures Formed Using AAT

Ceramic	Form	Process	References
SnO_2	Nanowire	AAT placed in electrolyte containing 0.05 M $SnCl_2.H_2O$. AC current (80 V peak-to-peak, 200 Hz) applied. Template removed and nanowires oxidized at 550°C for at least 2 h.	2, 10,
Si	Nanowire	Small layer of Au deposited on one end of template. Template was then exposed to silane and nanowires formed in pores by VLS. Etching with phosphoric and chromic acid removed template.	71
TiO_2	Nanowire	AAT placed in TiO_2 sol and held at 30°C, 10 h followed by drying at 60°C, 14 h.	146
ZnO	Nanowire	AAT placed in electrolyte containing $ZnSO_4$,H_2O and H_3BO_3. Electrodeposition used to form Zn nanowires. Template removed an Zn oxidized to ZnO.	147
SiO_2	Nanotube	Si sol deposited in pores of AAT and heated 150°C, 20 min.	148

AAT are ideal for 1D nanostructure formation because they can be used at much higher temperatures than other templates making them suitable for both solution and vapor-phase processes. Polymer templates break down at around 400°C.[150] Silicon nanowires have been formed using VLS growth mechanism at 540°C with AAT to form ordered, vertically aligned arrays with a very narrow range of size distribution.[71] The Si nanowires had average diameters of 38, 22, and 12 nm corresponding to AATs with pores of the same diameters. Solution-based processes have also used AAT.[e.g., 10, 147, 148] The main disadvantage with the use of an AAT is that an extra processing step is needed to remove the template. Polymer templates can often be burned off, but AAT are typically removed by etching that may be combined with ultrasonication to free the nanostructures.[10, 71, 147, 148] **Table 10** lists some of the 1D nanostructures that have been formed with the use of polymer templates.

Table 10. 1D Ceramic Nanostructures Formed Using Polymer Templates

Ceramic	Form	Process	References
TiO_2	Nanowire	PC template immersed in Ti sol and metal nanowires deposited by electrodeposition. Template burned off at 700°C for 15 min. Ti nanowires oxidized during heating.	74, 150
$BaTiO_3$	Nanowire	Same as TiO_2 except using Ba/Ti sol.	74
SiO_2	Nanowire	Same as TiO_2 except using Si sol.	73, 74
PZT	Nanowire	Same as TiO_2 except using Pb/Zr/Ti sol.	74, 149
V_2O_5	Nanowire	PC template with Al electrode on one end placed in aqueous solution of $VOSO_4$ and H_2SO_4. 1.5 to 2 V applied to electrode for 2 h, template was dried for 6 h at 110°C.	151
Si	Nanowire	Photoresistive polymer layer deposited on Si substrate. Lithography produced an array of aligned nanoscale features in photoresist. Subsequent plasma etching produced array of aligned nanowires.	152

Polycarbonate (PC) is currently the most commonly used polymer template for the formation of 1D nanostructures.[74, 150, 152]. Thin films of PC can be etched to create aligned pores with controllable diameters. Polymer templates can also be formed using lithographic methods.[151] The advantage of this approach is that the nanostructures can be formed with uniform sizes and in well defined 2D and 3D arrays.[151] Three-dimensional arrays are created by forming new polymer templates on top of already deposited arrays of aligned nanowires. The disadvantage of lithographic polymer templating methods is the number of processing steps. There are four major steps needed to form each nanowire layer:

- Deposition of polymer film
- Photolithography
- Nanostructure formation
- Template removal

The lithography step can be difficult to perform since the wavelength of light for lasers used in photolithography is often longer than the desired feature size. For example, arrays of aligned TiO_2 nanowires produced by photolithography with diameters of 250 nm may provide little advantage over conventional choices for sensors and catalysts.[151] Lenses and interference patterns may be used to reduce feature sizes.[151, 153, 154] Silicon nanowires with diameters of 20 nm have been produced using complex lithographic procedures; 10 additional processing steps were needed.[153] **Figure 7** outlines the steps required to form an array of 1D ceramic nanostructures using photolithography of a thin film deposited on a ceramic substrate.[154]

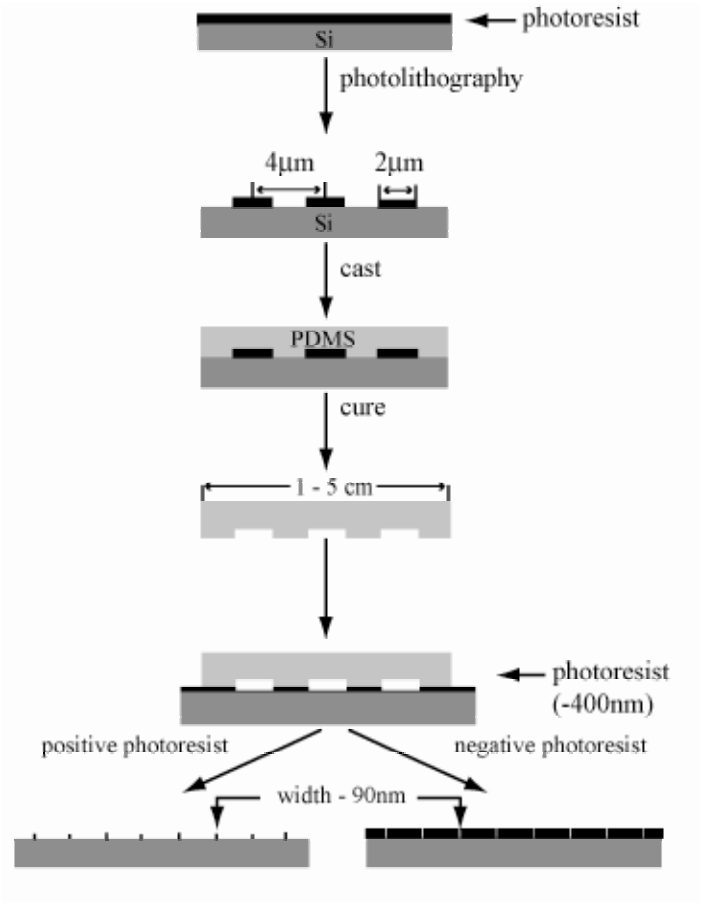

Figure 7. Schematic showing the process used to create aligned nanowires using photolithography. A negative photoresist is deposited on a ceramic substrate and a light source is used to create relief features. A PDMS mold is then cast on these features. The PDMS mold is placed in contact with a new, thin layer of photoresist, which is exposed using UV. The PDMS mold creates an interference pattern leaving an array of aligned 1D nanostructures. After developing a perfect template remains on the substrate for subsequent deposition of 1D nanostructures. Redrawn after Ref. 154

In addition to the solution growth techniques described earlier in this section, electrodeposition is an excellent method for forming 1D nanostructures (e.g., nanowires of ZnO, SnO_2, TiO_2, and $BaTiO_3$) using a template.[2, 74, 148] In electrodeposition, an electrode is plated at one end of the template (usually a PCT or AAT). A potential applied at this electrode attracts ions of the source material into the pores and initiates nanostructure formation. Unaided solution growth techniques using a template rely on capillary action to draw the solution into the pores before heating can begin, which generally takes a significant amount of time. In addition, the solution or sol-gel contains only a small fraction of source material, so drying causes considerable shrinkage. Electrodeposition can greatly reduce formation times but increases the possibility of forming polycrystalline or porous nanostructures. These types of structures are not desirable for most sensing applications due to the reduced conductivity. A porous structure adds surface area, which would seem advantageous for catalyst applications. However, the porous structure may be highly non-uniform with varying crystallographic surfaces exposed. Since specific planes are often desired in catalyst applications, the loss of exposure of certain planes may offset the effect of increased surface area.

The interaction of the source material with the walls of a porous template is very important to consider with solution-based growth processes. If the source material is attracted to the walls of the template, nanotubes will be formed.[149] If the source material is repelled from the template walls then nanowires are more likely, but they may not reach the full diameter of the template even with extended growth times.[155]

Nanostructures can also be used as templates and some examples are listed in **Table 11.** The templates can be coated in solution.[e.g., 156, 157] For example, SiO_2 nanotubes can be created around Au nanowires using an organic precursor with an attached silane functional group.[157]

The precursor molecules selectively attach to the gold and leave exposed silane groups, which facilitate the deposition of sodium silicate. The reaction between the silane and sodium silicate yields SiO_2. The diameter of the SiO_2 nanotubes was controlled by the ratio of precursor molecules to sodium silicate added to the solution. The Au cores were dissolved with KCl to yield SiO_2 nanotubes. Metal nanowires have been created by coating strands of DNA and individual proteins through a solution-based process.[158, 159] These methods have not been widely explored, but would seem to offer potential for 1D ceramic nanostructures as well.

Table 11. 1D Ceramic Nanostructures Formed Using Nanostructure Templates.

Ceramic	Form	Template	Process	References
SiO_2	Nanotube	Au and Ag nanowires	Nanowire templates placed in (3-mercaptopropyl)trimethoxysilane in ethanol. 2.0M aqueous sodium silicate added and solution stored for 1 day. Cyanide treatment removed the Au nanowire cores.	155, 156
Transition metal oxides e.g., Fe_3O_4	Nanowire	MgO nanowires	Laser ablation used to deposit metal oxides on an array of aligned MgO nanowires.	159
RuO_2	Nanotube	CNT	Ru was deposited on CNT by atomic layer deposition using a solution containing Ru precursors. Coated CNT heated to 500°C resulting in oxidation of the Ru nanotubes and ashing of the CNT.	160

Vapor processes have also been used to coat 1D nanostructure templates.[95, 160, 161] Gallium phosphide nanowires have been produced by coating CNT using CVD from Ga_2O_3 and P source powders.[95] The CNT were removed by converting them to CO. Nanostructure templates are especially advantageous for the creation of complex ceramic structures that might be difficult to create with other processes. One example is the formation of $La_{0.67}Ca_{0.33}MnO_3$ nanowires were produced by laser ablation using vertically aligned MgO nanowire templates.[160] These types of ceramics appear to be difficult to form by vapor phase synthesis without the use of a 1D nanostructure template to provide a suitable surface.

A unique 1D nanostructure fabrication technique (superlattice nanowire pattern transfer or SNAP) has been developed using a thin film composed of alternating layers of GaAs and $Al_xGa_{1-x}As$.[162, 163] The process is illustrated in **Figure 8**. The edge of the thin film layer is wet etched and a template of aligned channels is formed because the GaAs etches at a much lower rate than $Al_xGa_{1-x}As$. The diameter of the channels and their pitch are controlled by the specifics of the film growth and nanometer-sized dimensions are possible. A line-of-sight evaporation process allows for selective deposition of the metal in the channels of the template. The aligned metal nanowires are transferred to a ceramic substrate via a polymer, which is subsequently removed. A final plasma etching process yields an aligned set of ceramic nanowires or nanobelts on a substrate as the metal nanowires act as an etch mask.

The SNAP technique is useful because arrays of device-ready, aligned 1D ceramic nanostructures can be mass-produced without having to manipulate single nanowires. Although the number of steps involved would likely make it an expensive alternative to some other simpler approaches. It does offer the ability to easily vary the dimensions of the nanostructures. Silicon nanowires have been fabricated with diameters as small as 10 nm, pitches of 40-50 nm, and

lengths in excess of 1mm.[162] Defects were common in doped Si nanowires that have diameters < 25 nm. It is believed that doping of the substrate before nanowire formation was responsible for the introduction of the defects. So traditional doping procedures may need to be altered if very small, defect-free 1D nanostructures are required.

3.5 Arc Discharge Growth

Arc discharge growth was the first process intentionally used to form 1D nanostructures. [19] It was used for CNT and it has since been successful in producing other nanostructures such as Si nanowires and SiC nanowires. [e.g., 164, 165, 166] In a typical arc discharge growth two closely spaced electrodes are submerged in a liquid, often water, and an arc is created between them. The electrodes supply the source material for the nanostructures, which form on the electrode surface. Other liquids, including liquid nitrogen, have been used. [166] In some cases, heterogeneous catalysts are needed to initiate nanostructure formation, which often proceeds via a VLS process, and these are incorporated into the electrode. For example, iron powder can be added to the electrodes to form SiC nanowires, and Ni powder was required in the graphite electrodes to form single walled CNT.[165, 166]

The advantage of arc discharge growth is its relative simplicity. The procedure involves pressing the electrodes, immersing them in a suitable liquid and applying a potential difference. Only a few pieces of equipment are required: electrodes, a power supply, and a suitable bath to hold the liquid. No expensive vacuum systems are necessary and expensive or hazardous precursors can be avoided. The growth times are usually a few hours or less.

The primary disadvantage of the arc discharge method is the poor quality of the resultant nanostructures. The products are frequently mixed with various nanoparticles and must be

separated prior to use. The nanostructures created are often bent, polycrystalline, and have non-uniform diameters along their length. The poor qualities of the 1D products make them unusable in sensor or catalyst devices. The size distribution of the nanostructures can be very large, which means that the products of a single growth run can have widely varying properties. Improvements in the arc discharge method could make the procedure a simple, low cost method for the formation of 1D nanostructures compared to vapor, solution, and template methods.

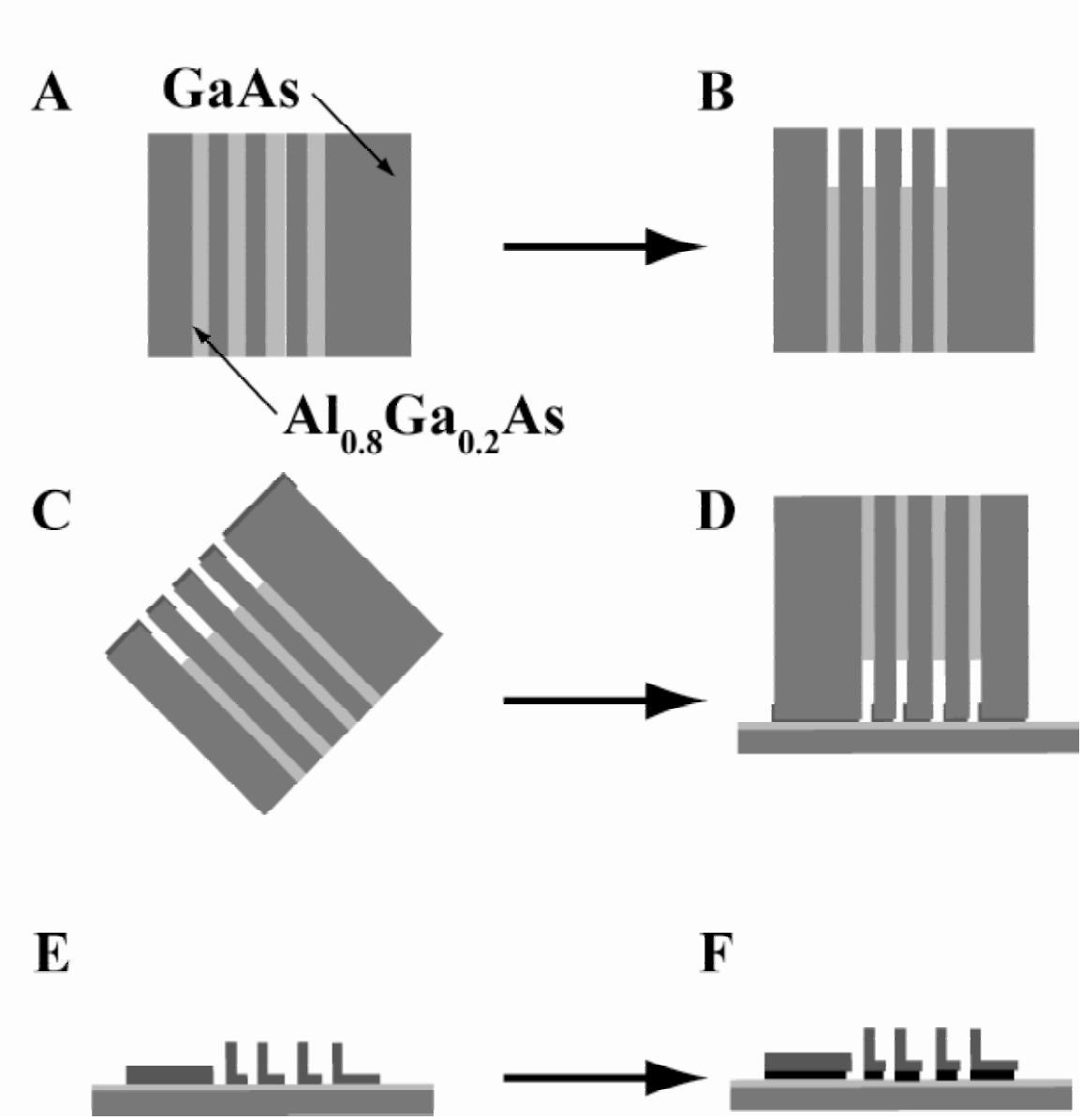

Figure 8. The main steps in the SNAP fabrication technique. A) A layered thin film of GaAs/$Al_{0.8}Ga_{0.2}As$ is created by atomic layer deposition. B) Wet etching is used to selectively etch the $Al_{0.8}Ga_{0.2}As$ layers on one edge of the film. C) Metal is deposited in the nanoscale channels by evaporation. The thin film is tilted relative to the metal source to prevent uniform deposition in the channels. D) Metal nanowires are deposited into a thin layer of epoxy and placed on a ceramic substrate. E) The template is removed leaving aligned 1D metal nanostructures above the substrate. F) Plasma etch with oxygen removes the epoxy and any ceramic not masked by the metal. Redrawn after Ref. 163.

3.6 Etching Procedures

Etching can be used to form vertically aligned arrays of 1D nanostructures on a substrate.[e.g., 167, 168] In an example of one process, Au or Ag nanoparticles were used to form Si nanowires.[167] The metal nanoparticles were deposited on a flat Si substrate and an etching procedure resulted in selective etching beneath the nanoparticles. An array of single crystal, vertically aligned Si nanowires was formed after etching of the substrate for only 1 minute. The nanowires could be formed in any crystallographic direction as the etching occurred perpendicularly to the substrate surface regardless of its surface orientation. The problem with this particular etching procedure was the varied shapes of the 1D nanostructures that formed. Since the substrate etched selectively underneath the spherical Au or Ag nanoparticles, the area between the spherical particles determined the cross sectional shapes of the nanostructures. It is unlikely that the Si nanowires had the same sidewall faces or a narrow distribution of cross sectional areas, making them unappealing choices for sensors or catalysts. A procedure for the formation of a very uniform distribution of metal nanoparticles would be needed before this process could be used for mass production of sensors or catalysts.

By etching an anodized aluminum membrane (which are also commonly used as 1D nanostructure templates) alumina nanotubes have been produced.[168] Commercially available alumina templates with different pore sizes were attached to Au foils. Etching in NaOH for less than 1h yielded arrays of Al_2O_3 nanotubes that were roughly aligned vertically on the gold film. The pore size of the Al_2O_3 template had little effect on the diameters of the nanotubes, which ranged from tens of nm up to 200 nm.

Etching procedures show some promise as quick, simple methods to form arrays of 1D ceramic nanostructures, but the processes need refinement before they can be used for sensor or catalyst device production.

4. Methods for Depositing Metal Nanoparticles on 1D Ceramic Nanostructures

Metal nanoparticles deposited on the surface of ceramic nanostructures can enhance their overall sensing and catalytic properties by several orders of magnitude. Controlled methods for depositing metal nanoparticles are of great importance because their size, shape and surface density can significantly affect the detection and catalyst capabilities of the nanosystem.

Several deposition methods have been developed to form metal nanoparticles and these can be separated into two general categories:

- Vapor phase, often involving an organometallic precursor
- Solution or suspension

4.1 Vapor Processes

Both CVD and physical vapor deposition (PVD) processes such as evaporation and sputtering have been used to deposit metal nanoparticles on 1D ceramic nanostructures.[e.g., 169, 170] CVD has been used to deposit nanoparticles of a number of different metals on ceramic nanostructures, including Pd on CNT, and Pt and Ni on both SiC and SiO_2 nanowires [171-173] It usually involves an organometallic precursor such as bis(cyclopentadienyl)nickel [Ni-$(C_5H_5)_2$] for the formation of Ni nanoparticles or dimethyl(1,5-cyclooctadiene)platinum (II) [$(CH_3)_2Pt(C_8H_{12})$] for Pt particles.[173] When the organometallic molecules come in contact with a heated surface a chemical reaction occurs and the metal atoms become physisorbed on the nanostructure. The rest of the molecule is removed in a carrier gas, usually argon. In general,

CVD allows for much shorter processing time than PVD. Platinum nanoparticles have been deposited on SiO_2 nanowires using CVD in a few minutes (**Figure 9**), while deposition times ≥1h are often reported for PVD process, e.g., W nanoparticles on CNT.[170] CVD also allows for good control over the size of metal nanoparticles. The flow rate of the gas and precursor, substrate temperature, and pressure in the deposition chamber all affect the particle size and size distribution.

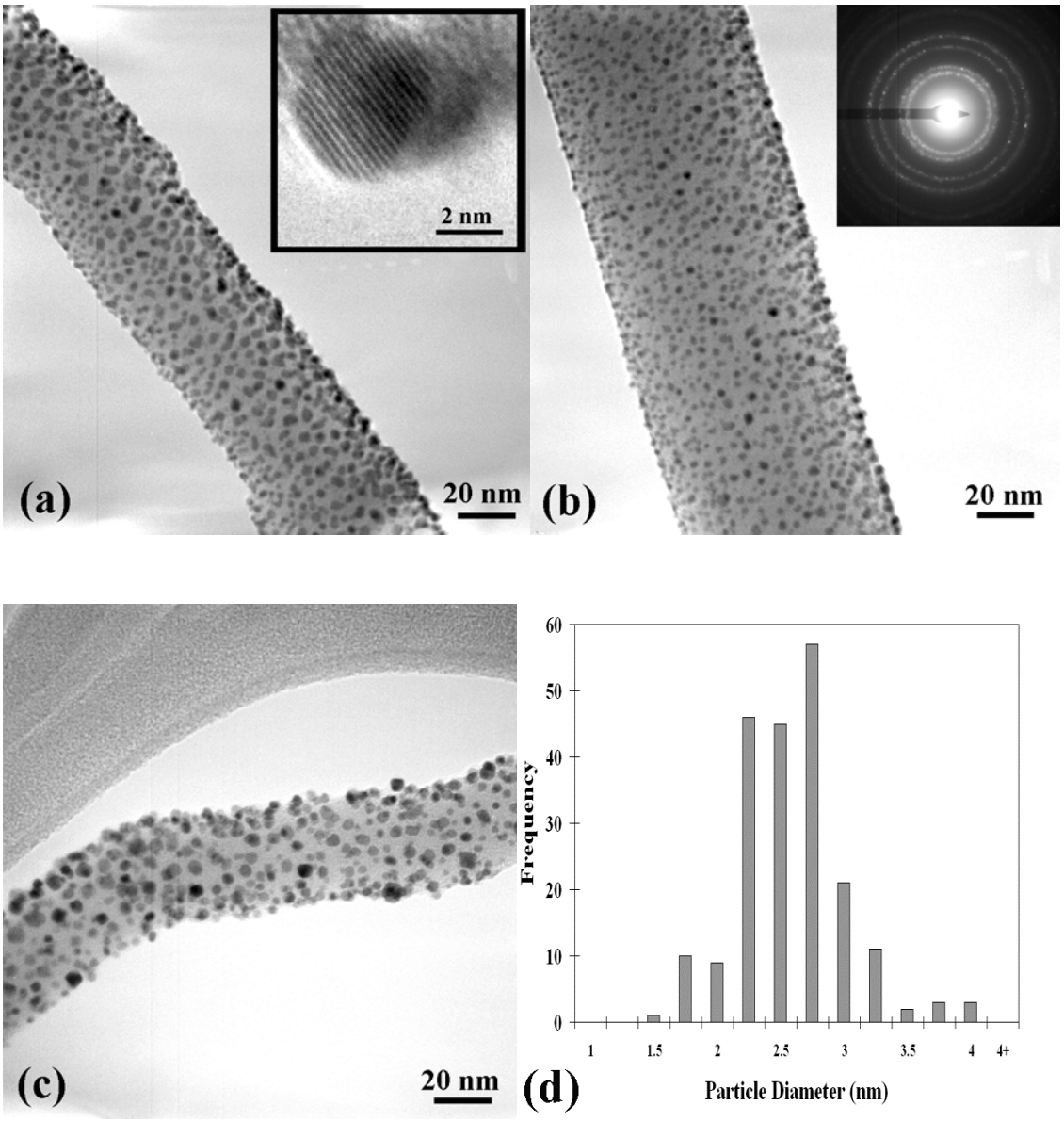

Figure 9. TEM images of Pt nanoparticles: (a) on a 40 nm SiO_2 nanowire, (inset) HRTEM image of a Pt nanoparticle, (b) on a 70 nm SiO_2 nanowire, (inset) diffraction pattern, (c) on a 35 nm SiO_2 nanowire, (d) histogram of particle size distribution of Pt nanoparticles. Reprinted with permission from Ref. 172, A. D. Lalonde, M. G. Norton, D. Zhang, D. Gangadean, A. Alkhateeb, R. Padmanabhan and D. N. McIlroy, J. Nanoparticle Res., 8, 99 (2006), Copyright @ Springer.

4.2 Solution Deposition Processes

Several types of solution process for the deposition of metal nanoparticles on ceramic nanostructures have been developed as shown in **Table 12**. Also included in this table are some of the methods used to form metal nanoparticles on films and planar substrates as these have potential application for coating 1D nanostructures. Solution processes generally follow a similar procedure. The metal source is suspended or dissolved in a liquid then the 1D nanostructures are added. The mechanism responsible for the attachment of the nanoparticle to the substrate varies between the processes.

Table 12. Solution Methods for Forming Metal Nanoparticles on 1D Ceramic Nanostructures

Metal	Ceramic (Form)	Method	References
Au	TiO_2 (nanotube,, thin film)	Anion adsorption/reduction, cation adsorption/reduction, deposition-precipitation, colloid	15, 173, 174
Au	ZrO_2 (thin film)	Colloid	174
Pt, Au, Ag, Cu, Ni, Cd	MoO_2 (thin film)	Electrodeposition	175
Ag, Mo, Pt, Au, Cu, Cd, Ni	Graphite (thin film)	Electrodeposition	176
Pt, Au, Ni	CNT	Cation adsorption/reduction, colloid, electroless plating	177-180
Ag, Cu	Si (nanowire)	Cation adsorption/reduction	70

The reduction of metal ions has been widely studied and proven to be an effective method for the deposition of metal nanoparticles on ceramic nanostructures.[70, 178, 179, 182] For example, the deposition of Pt nanoparticles on CNT has been demonstrated using a simple reduction process using a solution of H_2PtCl_6, water, ethylene glycol, and KOH.[179] The nanotubes were immersed in solutions of varying concentration and the metal ions reduced on the nanotube surface upon heating of the solution. As is typical of many solution deposition processes, the size of the metal nanoparticles depends on the reduction rate of the metal ions. Generally, fast reduction leads to increased growth rates and larger nanoparticles as well as a broader size distribution.[177]

Short deposition times and narrow size distributions have been achieved by using two different potentials during electrodeposition. A 5 ms initial pulse of 500 mV was used create nuclei of Pt, Au, Ag, Cu, Ni, and Cd on graphite substrates, while a 100 mV potential was used for 1 minute to slowly grow the nuclei into nanoparticles with a narrow size distribution.[176] Other factors that affect the metal nanoparticle deposition process and quality of the deposited particles include the solution concentration, pH, temperature, and surface defects on the nanostructure.[174, 178, 179, 183]

Au nanoparticles have been attached to functionalized CNT using a colloid containing Au nanoparticles.[180] The CNT were treated in acidic solution to create carboxyl, carbonyl, hydroxyl, and sulfate groups on their surface. Organic functional groups were attached at the sites created by the acid treatment. Negatively charged Au nanoparticles in solution bonded to the walls of the CNT through electrostatic interactions. The process is relatively simple and the Au nanoparticles were evenly dispersed on the nanotube surfaces because the acid treatment creates a regular pattern of exposed functional groups. A similar process has been used to attach

Au nanoparticles to planar surfaces of TiO_2, Al_2O_3, and ZrO_2.[175] In these cited studies, the Au nanoparticles were suspended in a colloid and then immobilized on the substrate in an acidic fluid. No functional polymers were needed to anchor the metal nanoparticles to the substrate. This type of suspension process may be feasible for the decoration of ceramic 1D nanostructures with metal nanoparticles.

4.3 Supercritical Fluid Deposition

A method for the deposition of metal nanoparticles on CNT using highly pressurized gas that shows the characteristics of both a liquid and a gas has been developed.[184] Organometallic precursors of the metals Pd, Rh, and Ru were used to decorate functionalized CNT. The deposition occurred in a stainless steel chamber filled with a supercritical mixture of H_2 and CO_2. The organic precursors dissolved in the CO_2. Heating of the chamber to between 80 and 250°C caused the metal particles to deposit on the surface of the nanotubes. The nanoparticles were well dispersed and had diameters ranging from 5-10 nm. The process was performed in 40 minutes. However, a complex experimental set up was required to perform deposition using the supercritical fluid and the adhesion of the nanoparticles to the CNT was weak; some fell off when the sample was ultrasonicated.

5. Properties of 1D Nanostructures

5.1 Properties Associated with One Dimensionality

One-dimensional nanostructures have shown exciting promise as sensors and catalysts due to unique properties not found in the corresponding bulk and thin-film forms. The electronic behavior exhibited by 1D nanostructures, due to quantum size effects, differs greatly from the electronic behavior of bulk materials and contributes to improved sensors and catalysts. For example, the bandgap energy (E_G) of 1D nanostructured ceramics depends on their diameter.

Silicon nanowires with 7nm diameters have E_G = 1.1 eV (close to the bulk value), while when the diameter is reduced to 1nm E_G = 3.5 eV.[185]. This property allows tailoring of E_G for specific applications. In some instances the size dependence may be a limiting factor in the use of a 1D nanostructure as a catalyst or sensor. For example, GaN nanowires with diameters <17.6 nm are insulating, indicating that small diameter GaN nanowires will not be useful as resistive elements in sensor applications.[156]

The high surface to volume ratio found in 1D nanoceramics is desirable for sensing and catalyst applications due to the vast amount of reactive surface sites available compared to bulk material. Nanoscale particles offer even higher surface to volume ratios than 1D nanostructures, seemingly making them better suited for catalysts and sensors. However, 1D nanostructures remain more desirable for these applications for several reasons:

- They can be grown reproducibly using a number of different techniques.
- In many cases they grow in the same crystallographic direction with the same crystallographic planes exposed on the side walls. Nanoparticles usually have a varied distribution of surface planes. TEM has shown that Ti nanoparticles exhibit faceted surfaces with as many as six different crystallographic planes exposed.[186] A specific family of crystallographic planes in a ceramic usually provides a lower surface energy for adsorption or catalyzes a reaction more efficiently than other planes. The predictable surface features of 1D nanostructures typically make them efficient catalysts and sensitive sensors. **Figure 10** shows the catalytic properties of CeO_2 nanowires compared to CeO_2 nanoparticles for the oxidation of CO.

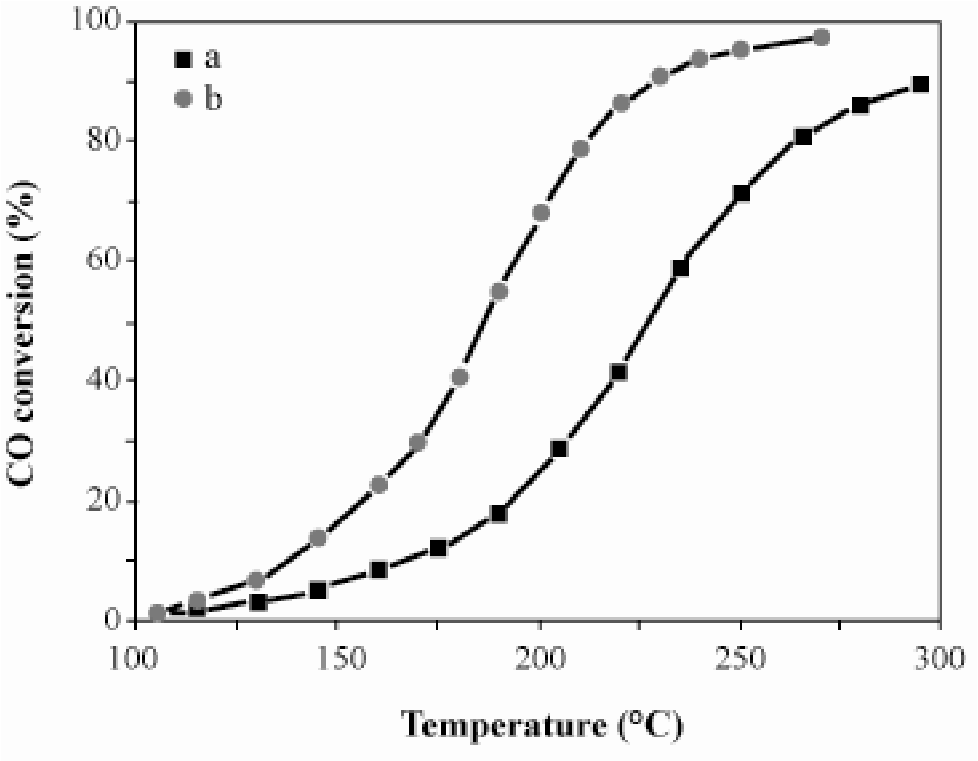

Figure 10. Percentage of CO oxidized versus temperature by a) CeO2 nanoparticle and b) CeO2 nanowire catalysts at temperatures ranging from 100-300°C. Data from Ref. 26

- They can be more easily integrated into practical devices than nanoparticles. Nanoparticles are not easily connected into circuits or transistors or immobilized on a substrate without being first imbedded in an adhesive media. Simple circuits and complex FETs that would be impossible to create using nanoparticles alone can be fabricated using 1D nanostructures.[7, 9, 31, 60, 62, 64] Processes and considerations of integrating 1D nanostructures into functional devices is further discussed in a later section.

5.2 Resistivity Changes in 1D Nanostructure Sensors

An outside species must adsorb on the surface of a 1D nanostructure in order for it to function in all catalyst applications and most sensor devices. In sensors, a molecule or atom adsorbed on the surface of the nanostructure might drastically alter □ by either withdrawing or injecting electrons. An individual 1D nanostructure can be viewed as a conducting channel with a specific cross sectional area available for charge carrier transport. When an atom or molecule that withdraws the charge carriers is adsorbed, the cross-sectional area available for current flow is effectively decreased due a depletion region at the surface of the nanostructure near the adsorbed species.[186] **Figure 11** shows a schematic view of the depletion region caused by adsorbed species that affect the carrier density of a 1D nanostructure.

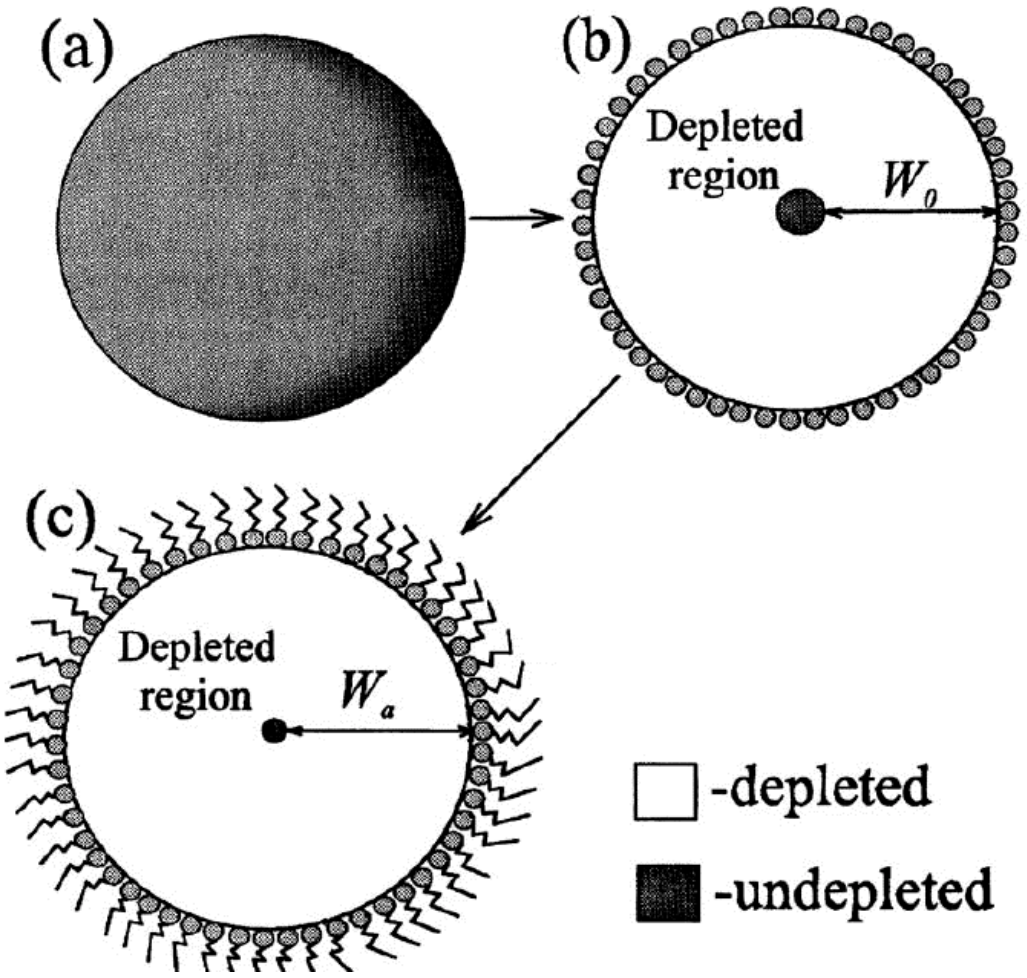

Figure 11. Schematic cross-sectional view of a nanowire, showing the size of the conducting channel (grey) with no metal nanoparticles on its surface (a), decorated with metal nanoparticles (b), with gas adsorbed on the surface of the nanoparticles (c). Redrawn after Ref. 115.

.

Since the depletion region created by the adsorbed species is nearly the same size as the diameter of the nanostructure, the change in □ in the nanostructure can be several orders of magnitude. [e.g., 3] This is in contrast to bulk materials where adsorbed species may alter the density of charge carriers or create a depletion region at the surface, but not throughout the bulk of the material. The observed change in □ is therefore much smaller than that found in 1D nanostructures. The size of the depletion region in the nanowire is determined by the boundary conditions at the interface. For example, the depletion region formed in a GaN nanowire at the interface between the nanowire and a Au nanoparticle has been recently examined.[186] With a sufficient density of Au nanoparticles on the nanowire surface, a uniform depletion region is created in the outer diameter of the nanowire, causing an increase in □. This effect is an important consideration when forming functional devices using nanoparticle-decorated nanostructures.

By comparing □ of the nanowire in the presence of an external species to □ of the nanowire in an ambient condition, the concentration of the species in a certain environment can be determined (providing a calibration is performed, e.g., by exposing the sensor to known concentrations). Other molecules present in the environment may also affect □, making specific sensing a complex issue. Proposed solutions for selective sensing are described in more detail later. Outside species adsorbed on the surface of the 1D nanostructure may also donate charge carriers. In this case, the density of charge carriers in the nanostructure will increase, causing a measured decrease in □. The principles and methods for detection remain the same.

Although smaller nanostructures have larger surface area to volume ratios, a minimum cross-sectional area is required for 1D nanostructures used as resistive elements in sensors. There must be enough of an undepleted cross sectional area so that there will be a conducting channel in the

nanostructure when the external species to be detected are adsorbed. The required cross-sectional area can be calculated as a function of the charge carrier concentration in the nanostructure and the effective gating potential induced by the detected species.[115] Each individual adsorbed molecule or atom is viewed as applying a gate potential to the 1D nanostructure in a similar manner that a gate potential is used to alter □ of the conducting channel of a transistor. If the adsorbed species create too large a gating potential, there will not be a conducting channel through the nanostructure, rendering it ineffective as a sensing element. Calculations have been made for sensing of N_2 using GaN nanowires.[115] In each case, a 50% change in □ was set as the standard for successful sensing of an arbitrary gas concentration. The calculations showed that a nanowire with a carrier concentration of $2x10^{17}$ cm^{-3} required a diameter of at least 194 nm, while a nanowire with a carrier concentration of $5x10^{17}$ cm^{-3} required a minimum diameter of 126 nm in order to be responsive to the specified concentration of gas.

Equation 2 relates the radius of the conducting region of a nanowire in a vacuum and in the presence of an adsorbed species to the measured current.[115] It is the result of the considerations described above and is useful for determining the minimum diameter of nanowires required for sensing applications where the measured current through a set of nanowires will be translated into a concentration of detected species.

$$\frac{I_g}{I_0} = \frac{r_{cg}^2}{r_{co}^2} \qquad (2)$$

I_g = Current measured through nanowire in presence of adsorbed species

I_0 = Current measured through nanowire in vacuum

r_{cg} = Radius of conducting channel of nanowire with adsorbed species

r_{co} = Radius of conducting channel of nanowire in vacuum

Even though a minimum cross-sectional area is required for a 1D nanostructure intended for sensor use, the cross-sectional area must not be too large. The unique electronic properties, which often facilitate adsorption of the detected species, will be lost as the nanostructure approaches bulk dimensions. In addition, the depletion region caused by surface adsorbent must be on the same order of magnitude as the cross-sectional area of the 1D nanostructure, or changes in □ will be less obvious.[3]

For catalyst applications the nanowire surfaces need to be low energy sites for reactants to adsorb. An efficient nanowire catalyst should also quickly and easily convert the reactants into reactive intermediate species. Thus, control over growth direction and the exposed surface planes are important for 1D nanostructures for catalyst applications. For example, the {110} and {100} planes of CeO_2 are approximately twice as catalytically active for the oxidation of CO than the {111} planes.[27] In addition, different crystallographic phases may lead to more efficient catalytic properties for some ceramics. The catalytic activity of the monoclinic phase of ZrO_2 is approximately an order of magnitude greater than that of the tetragonal phase for the conversion of CO, CO_2, and H_2 to methanol.[187]

5.3 Adsorption of External Species

The adsorption of molecular species onto the surface of the 1D nanostructure is necessary for sensing and catalyst applications. The change of the electronic band structure of a material as it reaches nanoscale dimensions is an effect of the reduced interaction with neighboring atoms. As a result, the surface atoms have the ability to easily change electronic state and assist the adsorption process. One dimensional nanostructures of several of the transition metal oxides

including TiO_2, Fe_2O_3, CuO, Co_3O_4, and V_2O_5 have already proven to be well suited for these applications.[e.g., 34, 35, 42, 63-65, 109] Metal oxide nanowires have cations that can easily change valence states and a controllable number of oxygen vacancies. The number of surface oxide vacancies contributes to the doping level of the nanostructures and the metal atoms missing a bond due to an oxygen vacancy can readily change between valence states. Oxygen vacancies are often preferred adsorption sites, as electrons are easily transferred between adsorbed surface species and the surrounding metal ions in order to stabilize the adsorbate. One dimensional metal oxide nanostructures have many available surface sites, typically on the order of 10^{20} cm^{-3}.[188]

Catalytic oxidation reactions are well suited to metal oxide nanowires, as molecular oxygen has been shown to dissociate and fill oxygen vacancies as readily available, highly reactive atomic oxygen.[26] Studies have also shown that gas species containing oxygen sometimes do not bind well to metal oxide surfaces without the presence of oxygen vacancies.[38] In addition, the products of the catalyzed reaction or adsorbed species can often desorb from the nanowire surface with very little energy since the metal ions can easily switch valence states, causing a change in the affinity of the products for the metal oxide surface.

5.4 Metal Nanoparticle/Ceramic Nanowire Architectures

Nanometer sized metal particles deposited on the surface of nanowires can enhance the catalytic activity and sensing properties of nanowire devices. The metal particles serve as extremely active sites for the adsorption and dissociation of molecules due to their unique electrical properties caused by quantum size effects. As metal particles reach the nanometer size range, the energy bands lose their nearly continuous nature (of the bulk material) and become quantized. There is a shift in E_F leading to semiconductor behavior.[29] This behavior greatly enhances the ability of

the nanoparticles to adsorb and dissociate external molecules. Gold nanoparticles showing semiconductor behavior have been reported as being especially catalytically active.[20, 21, 72, 139, 189] Structural effects also appear to be important. Small Au nanoparticles containing ≤12 atoms are particularly active for the oxidation of CO and are generally amorphous, whereas nanoparticles with >13 atoms are crystalline. [190]

The shape of Au nanoparticles also appears to influence their catalytic activity. Nanoparticles with 13 atoms and icosahedral symmetry were more active than similarly sized particles having cuboctahedral symmetry. The icosahedral symmetry is constructed entirely of corner atoms bonded to five other atoms, while the octahedral symmetry consists of corner atoms bonded to four other atoms. These two symmetries yield different band structures.[190] Even particles consisting of 300 atoms were shown to have band structures different from bulk gold, although they are less catalytically active than smaller nanoparticles.[21] Minimizing the overall potential energy of metal nanoparticles is the reason or the drastic changes in particle shape and crystal structure from the bulk metal: the potential energy is heavily influenced by the number of nearest neighbors. The transition of geometries and crystallinity is similar to the types of changes that have been observed in Al nanoparticles consisting of several hundred to a few thousand atoms.[114] The activity of transition metal nanoparticles has been extensively studied and appears to be optimal for particles in the range 3-6 nm.[191] The electrical properties conducive to catalyst and sensor applications in these metals are due to quantum size effects similar to that found for Au nanoparticles. In particular, the nanoparticles of metals that have either d-band vacancies or easily ionized d-bands (e.g., Au, Fe, Co, Ni, Cu, Rh, Pd, and Ag) are highly active.

Gold nanoparticles supported on 1D metal oxide nanostructures have been demonstrated as excellent chemical sensors and catalysts.[21, 77, 192, 193] The increased activity in these

systems is believed to be related to the phase boundary between the metal and ceramic: for Au nanoparticles on TiO_2 substrates the Au atoms bonded to Ti and O atoms are the most active atoms in the system.[194] Atoms or ions dissociated by metal nanoparticles can diffuse onto the surface of the ceramic where they may react with other atoms or remained physisorbed for detection. The enhanced adsorption rate at the metal particles often leads to a higher catalytic activity and faster chemical sensing using nanowire/metal nanoparticle architectures than either the ceramic or metal system alone. The oxidation of CO takes place approximately 100 times faster on an Au nanoparticle/TiO_2 support rather than on Au nanoparticles with the same amount of surface area.[192] The same reaction is not catalyzed at all by TiO_2. **Figure 12** shows the enhanced activity of the CeO_2 nanowire/CuO nanoparticle system over CeO_2 nanowires for the oxidation of CO.

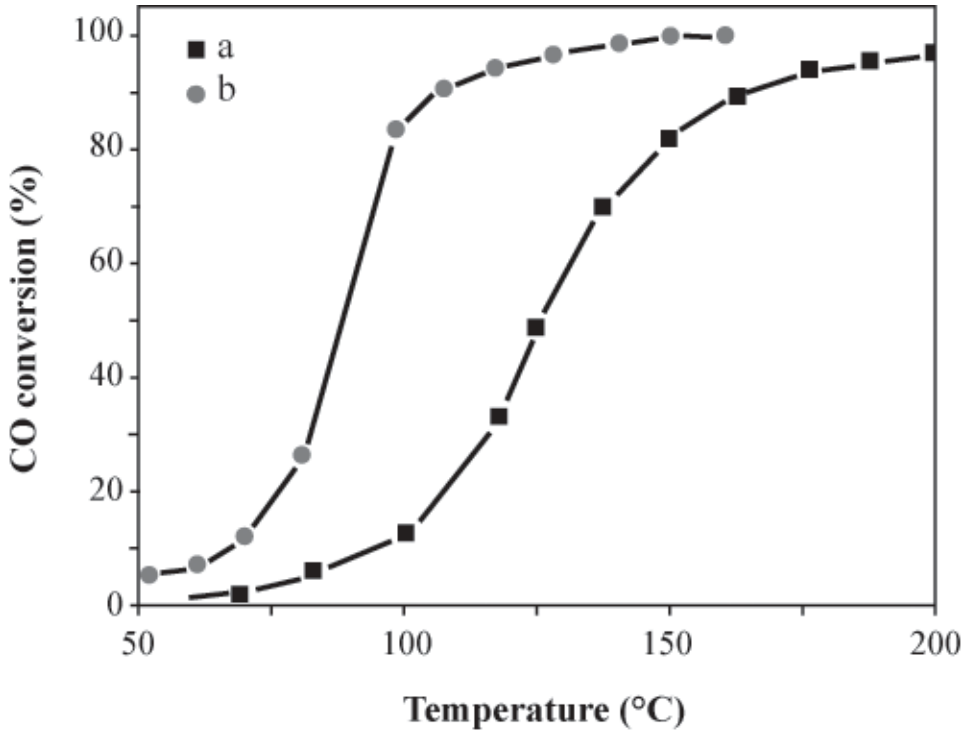

Figure 12. Percentage of CO oxidized versus temperature by a) CuO/CeO_2 nanoparticle and b) CuO/CeO_2 nanowire catalysts at temperatures ranging from 50-200°C. The data indicate that the CuO/CeO_2 system catalyzes the oxidation of CO more efficiently than CeO_2 catalysts alone. Data from Ref. 27.

Much more research is needed to understand the details of the complex interaction between metal nanoparticles and ceramic supports. For example, why is the oxidation activity of CO catalyzed on an Au nanoparticles on $SiO_2/Si(100)$ substrates increased by over 60 times by adding only trace amounts of a metal oxide such as FeO. [189]

6. Device Processing

The processing of 1D nanostructures into sensors and catalytic devices remains a major obstacle for their widespread commercialization. Devices that require the nanostructures to be configured with electrical connections have proven particularly hard to manufacture. Several techniques for the processing of 1D nanostructures into simple circuits and FETs have been developed, but none of these techniques offer an easy method for inexpensive mass production.

There are two main types of processing methods used to form devices:

- Bottom-up manufacturing where the 1D nanostructure is grown in a configuration that can be directly used to create a device without direct manipulation of the nanostructures.
- Top-down manufacturing requires the manipulation of the 1D nanostructures after growth.

Bottom-up manufacturing is desirable as the manipulation of single 1D nanostructures can be time consuming, expensive, and not well suited for mass production. A good illustration of bottom-up manufacturing is the growth of vertically aligned 1D nanostructures on a substrate that acts as an electrode. Another electrode can be fabricated on the free ends of the nanostructures to create a simple circuit.

Flat FET devices with single 1D nanostructures placed laterally between source and drain electrodes on an insulating substrate may be exceedingly difficult to fabricate with bottom-up processes. In addition, ultra sensitive detectors with a single 1D nanostructure seem unlikely to be formed in a bottom-up manner using vapor processes. The commonly used growth techniques to form 1D nanostructures produce large quantities of nanostructures simultaneously without much control over their exact location on the substrate. Another problem with bottom-up manufacturing is the difficulty involved in easily creating identical devices and the poor reproducibility of many methods used to produce nanostructures, e.g., CVD of CNT.

The advantage of the top-down approach is the ability to form devices of precise shapes and dimensions that are nearly impossible to form with bottom-up processes. An example is the placement of a single Si nanowire across two electrodes in an FET based sensor.[62] Top-down techniques are typically very difficult to execute, since the manipulation of a single 1D

nanostructure into exact placement on an electrode or substrate is a difficult and often expensive procedure. However, some top-down techniques described in this chapter involve the simultaneous placement of multiple 1D nanostructures into devices where precise placement is not required for the effective operation of the device.

6.1. Top-Down Techniques

There are methods to manipulate single 1D nanostructures into circuit-based devices, however these techniques, such as electron beam lithography, seem at present much more useful in laboratory settings than in industry. The following sections focus on techniques that are more likely to be useful for inexpensive mass production of sensor and catalyst devices.

6.1.1Solution Drawing

Alignment of 1D nanostructures using a fluid and channel has been the most promising top-down manufacturing process for the creation of sensors and catalytic devices. A solution containing the nanostructures is either compressed in or flowed through a channel to create an array of aligned nanostructures on a substrate.[195, 196, 197, 198] For example, arrays of aligned $BaCrO_4$ nanowires have been created on a flat substrate by suspending them in water and compressing the suspension in a long trough (25 x 100mm and was 75 mm deep) with the substrate.[196] With an applied pressure $>0.035 N.m^{-1}$ the nanowires become aligned on the substrate.

Nanowires of GaP, InP, Si and molecular $[Mo_3Se_3^-]_\infty$ have been aligned into 2D arrays by flowing a suspension of nanowires through a channel.[195, 197] The channels can be formed using methods used to produce microfluidic devices involving poly(dimethylsiloxane). Two-dimensionality is created by repeating the method with the channel orientated in a different direction from the originally deposited nanowires. The channel is placed on the substrate and the moving fluid creates a drag force on the nanostructures that causes their long axes to align in the

direction of the fluid flow. This approach is similar to that used to align whiskers during tape casting of whisker-reinforced composites. Several geometries of nanowire junctions have been demonstrated with this technique including square, rectangular, and triangular 2D arrays.[195]

Suspension alignment processes are advantageous over other top-down methods because individual 1D nanostructures do not need to be manipulated. Large amounts of 1D nanostructures can be aligned and placed in an area in a single process, saving time and money. Single electrodes can be formed over multiple 1D nanostructures as well, since research has shown that the sensing capabilities of 1D nanostructure based sensors are not affected by multiple nanostructures connecting to a single electrode.[1] There is minimal cross talk between the nanostructures, so microfluidic alignment is a viable option for device fabrication. The distance between the electrodes is the most important aspect of electrode placement. [1]

6.1.2. Dielectrophoresis

Some 1D ceramic nanostructures suspended in a fluid can be aligned with an alternating electric field by a method known as dielectrophoresis.[198] Carbon nanotubes and SnO_2 nanobelts have been aligned using this method.[99, 199] Carbon nanotubes aligned by dielectrophoresis were first suspended in a mixture of non polar liquids.[199] This suspension was placed between two specifically patterned rectangular electrodes. An alternating current applied at a frequency of 4 MHz through the electrodes aligned the CNT perpendicular to the electrodes in 15 minutes. A new set of electrodes patterned in a different orientation were used to create another layer of aligned CNT on top of the first layer, proving that 2D arrays can be formed using dielectrophoresis in a similar manner to microfluidic flow alignment. SnO_2 nanobelts can aligned by dielectrophoresis using in a similar process to that used for CNT.[99]

Dielectrophoresis methods may be very difficult to scale up for mass production because the uniformity of the applied electric field is very important. If multiple electrodes are used near each other the electric field between complementary electrodes may not be uniform due to interference by other pairs of nearby electrodes. The alignment of 1D nanostructures could be affected in these manufacturing conditions.

6.1.3 Disadvantages with Micro Fluidic Alignment and Dielectrophoresis

The main problem with the fluid alignment methods for 1D nanostructures is the inability to place a 1D nanostructure in an exact location. Dielectrophoresis methods, particularly those where the nanostructures are attracted to the electrodes, guarantee that one end of the nanostructure is placed on an electrode. However, it is more difficult to control orientation of the 1D nanostructure on the electrode with dielectrophoresis methods where the tips of the nanostructures are attracted to the electrodes. A significant percentage of the nanostructures do not span both electrodes. The average distance between the nanowires can be decreased and the

density of nanowires increased by increasing the flow time or concentration of the suspension. However, the ends of the 1D nanostructures are still randomly placed along the length of the channel. Electrodes can be patterned over the nanostructures, but some of the nanostructures may only be connected to a single electrode. In addition, surface groups may need to be bonded to the surface of the substrate to enhance the adhesion of the nanostructures to the substrate. In one study, NH_2^- terminated monolayers were needed on the substrate to adhere the first layers of InP nanowires in place.[195]

6.1.4. Selective Bonding with Functional Groups

Functional groups bonded to CNT have been used to selectively place them on substrates.[200] In this top-down process, molecules with hydroxamic functional groups were covalently bonded to the CNT. The functional groups made the nanotubes selectively bind to Al_2O_3 but not SiO_2. SiO_2 substrates with Al_2O_3 stripes of approximately 40nm by 300 nm were fabricated, and functionalized CNT dispersed in ethanol or methanol placed on the patterned substrates. The Al_2O_3 stripes were patterned such that the CNT were longer than the width of the stripe. The deposition process resulted in the CNT roughly aligning along the length of the Al_2O_3 stripe. The functionalized polymer was burned off, and Pd electrodes were placed perpendicular to the stripes across the entire substrate to make FETs.

Out of forty nine nanotube/electrode junctions measured, only twenty eight showed an electrical connection in this type of FET device.[200] Of the working devices, sixteen were semiconducting junctions and twelve were metallic. The difference in electrical behavior was likely due to different wrapping configurations in the CNT: the percentage of functional junctions needs to be improved. The fabrication process takes several steps, including a precise electron beam lithography patterning of the Al_2O_3 stripes. The process will need modification for

different substrates and 1D nanostructures. In addition, the functional group bound to the CNT affected their electronic properties and had to be removed at 600°C, a processing temperature that might be unsuitable for other materials combinations.

6.2 Bottom-Up Techniques

Although some top-down manufacturing techniques allow for the creation of ultra precise devices used for research on a few or even single 1D nanostructures as sensors and catalysts, bottom-up techniques currently seem better suited for sensor and catalyst device processing because they eliminate the need to manipulate 1D nanostructures, which usually requires several collection and cleaning steps.

6.2.1 Processing 1D Nanostructures Directly into Devices

Mats of unaligned, curved nanowires supported on a substrate, which are characteristic of many vapor based growth processes, can be used directly as catalysts with little additional processing. These types of 1D nanostructures are commonly formed under less restrictive growth conditions than straight, aligned 1D nanostructures. They can also be formed into simple sensors if the nanostructures are relatively densely packed.[115] A traditional four point electrical connection may be made on arbitrary points on the mat to form a simple circuit. This setup has been used to determine the sensing capabilities of 1D nanostructures in laboratory settings. Several paths for the transport of charge carriers are typically present across multiple nanostructures in the mat, allowing for detection of adsorbed species providing there is an associated change in charge carrier density.

Aligned 1D ceramic nanostructures supported on a substrate have been processed into several working devices as shown in **Table 13**.[45, 50, 52, 54-56, 117, 201, 202] These techniques offer great promise as methods to mass produce sensors and catalytic devices.

Table 13. Devices Produced Using Aligned 1D Nanostructures

Nanostructure	Sensor	Process	References
ZnO nanowire	Radial FET	Vertically aligned nanowires grown and SiO_2 deposited on substrate for support. Cr electrodes applied at tips of nanowires.	202
CNT	Ionization sensor, radial FET, simple electrode	Used for detection of biological species in solution. The CNT were functionalized and an electrical connection established with the substrate.	45, 50, 52, 54-56
Si nanowire	FET	Nanowires grown across a channel to bridge two pieces of Si. Source and drain electrodes were plated, making the Si nanowires the gate.	117
In_2O_3 nanowire	Vertical FET	Vertically aligned nanowires grown and SiO_2 deposited between nanowires for support. Electrodes were patterned at the tips of the exposed nanowires after mechanical polishing.	201

There are several methods for producing aligned groups of straight nanowires and CNT.[45, 91, 201, 202] For example, vertically aligned ZnO nanowires have been grown by CVD on alumina substrates with specific crystallographic orientations as shown in **Figure 13**.[91] Epitactic growth resulted in the nanowires forming perpendicularly to the substrate surface. These nanowires and nanotubes are generally easier to fabricate into complex sensor and catalyst devices than mats of curved, non-aligned nanowires and nanotubes.

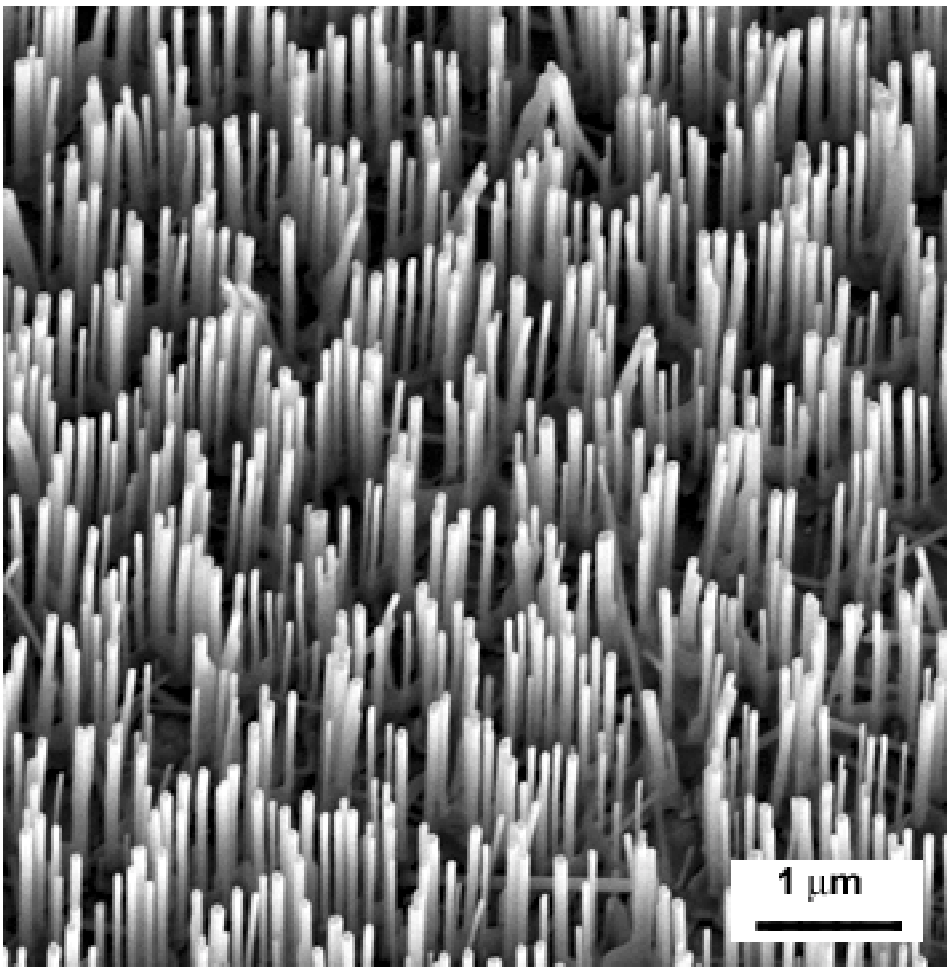

Figure 13. SEM image of vertically aligned ZnO nanowires grown by evaporation on an alumina substrate. Reprinted with permission from Ref. 91, X. Wang, C. J. Summers, and Z. L. Wang, Nano Lett., 4, 423 (2004), Copyright @ American Institute of Physics. Image courtesy of Prof. Z.L. Wang, Georgia Tech University.

Aligned Si nanowires have been grown into an FET template using catalyst-assisted CVD.[118] Two parallel (111) surfaces were created in a silicon wafer using reactive ion and wet etching. The faces were formed between ridges of Si atop insulating SiO_2. Electron beam evaporation was used to deposit Ti or Au nanoparticles on one of the facing (111) surfaces by orientating the substrate at a specific angle to the evaporating metal. The CVD growth was initiated and Si nanowires grew across the gap between the substrate faces. The growing nanowires formed an electrical connection with the opposite face upon reaching the other Si plane. Electrodes were plated on top of each ridge of Si to form FETs.

Vertically aligned ZnO nanowires have been processed into vertical surround gate FETs (VSG-FETs) using a bottom-up procedure.[202] A layer of SiO_2 was deposited by CVD over the aligned nanowires on a SiC substrate to form the surround gate layer. An ion beam process was used to deposit a layer of Cr over the SiO_2 coated nanowires and another layer of SiO_2 was deposited over the entire top of the substrate to form a block of SiO_2 around the layered nanowire structures. Mechanical polishing was used to polish the top of the SiO_2 layer and remove the catalyst particles from the tips of the nanowires. Next, a wet etching process was used to remove a portion of the exposed ring of Cr surrounding each ZnO nanowire, leaving a trench around the exposed tip of each nanowire. Chromium drain electrodes were plated at the tip of each exposed nanowire. The process left the ZnO nanowires covered with SiO_2, however an extra selective etching step could presumably be used to remove SiO_2 resulting in parts of the ZnO nanowires being exposed for sensing or catalysis. Although complicated processes like this require many steps to create devices, advantages are still maintained over top-down manufacturing. The complicated process of manipulating the 1D nanostructures is avoided, and

there is a vast amount of knowledge about etching and deposition techniques for Si and SiO_2 from the semiconductor industry.

6.3 Device Manufacturing Issues

The placement of the electrodes is a very important consideration when developing a process to create sensors or catalytic devices with 1D nanostructures. The distance between electrodes in FET or simple circuit designs affects the electrical behavior of the device. It has been shown that the observed □ of SnO_2 and ZnO nanobelt-based FETs was more difficult to modulate when the spacing between the electrodes was short.[7] When the electrode spacing was 127 nm, the measured □ was nearly identical at any gate potential between -15 V and 15 V. When the spacing was increased to 1840 nm, □was 5 orders of magnitude greater at a gate potential of -10 V compared to a gate potential of 10 V.

These data indicate that □ is not only contingent on adsorbed species on the 1D nanostructure, but also a function of the channel length of the detector. However, other groups have speculated that an ultra short channel length could be used to form sensors capable of detecting single molecules since a short 1D nanostructure would only facilitate the adsorption of a single species and still produce a measurable change in □.[60]

The placement of the 1D nanostructures in relation to the electrodes can affect the behavior of sensors. For example, V_2O_5 nanobelts used as resistive elements in FET devices for amine sensors showed different electrical behavior depending on the placement of the nanobelts on the electrodes (i.e., whether they were on top or below).[64] In this case, □ increased upon exposure to an amine molecule when the nanobelts were on top of the electrodes and decreased if the Au electrodes were placed above the nanobelts. The study also showed that different sites on the

nanobelts were responsible for different responses upon exposure to amines. Some of the sites were inaccessible to the amines if the nanobelts were in contact with the SiO_2 substrate.

The development of inexpensive processing methods for 1D nanostructure based devices still remains the most prevalent issue holding back the widespread introduction of sensors and catalysts with 1D nanoscale technology into the market. The techniques for creating devices mentioned above work well in laboratory settings and offer promise as realistic methods for creating sensor and catalyst devices, but until these processes are improved or new processing methods are created 1D ceramic nanostructures will not be a feasible option for sensors and catalysts.

7. Research Opportunities

With all the promise that 1D ceramic nanostructures have shown for catalyst and sensor applications, there remains much research to be done on a wide range of issues prior to their widespread use. The topics requiring further research vary, ranging from catalysts for specific reactions expected to be important for energy production to the need for improved sensors for counter terrorism. The following sections outline some of these issues along with the direction of current research activities.

7.1 Fuel Cell Catalysts

A low energy method for the production of hydrogen has emerged as an important issue. The waning supply of fossil fuels paired with the increasing demand from rapidly developing nations such as China makes it inevitable that alternative energy sources will be needed. In the United States oil, coal, and natural gas accounted for 84% of the total energy consumed in 2004, and an estimated 12 million barrels of oil were used daily to power all of the transportation vehicles in the US.[203] Hydrogen has been predicted as a fuel source for future vehicles through the use of

hydrogen combustion engines and eventually the hydrogen fuel cell. Ford and BMW are both actively researching a hydrogen internal combustion engine as an interim solution before fuel cells become affordable.[204] There are several proposed reactions using various fuel sources for the fuel cell, but the most basic and commonly recognized reaction for the production of energy by the direct oxidation of H_2, given by Equation 3 will be discussed.[205] **Table 14** lists some of the other commonly studied fuel cells.[205, 206]

$$2H_2 + O_2 \rightarrow 2H_2O \qquad (3)$$

The reaction in Equation 3 produces 1.229 V between the anode and cathode due to the difference in potential between the half cell reactions at the electrodes.[205] An important factor in the fuel cell operation is the ability of the catalyst to facilitate this reaction at a high rate.

Table 14. Types of Fuel Cell

Type	**Cathode Reaction**	**Anode Reaction**	**Overall Reaction**	**Operating temperature (^oC)**
Alkaline-KOH (AFC)	$O_2+2H_2O+4e^-\rightarrow 4OH^-$	$2H_2+4OH^-\rightarrow 4H_2O+4e^-$	$2H_2+O_2\rightarrow 2H_2O$	50-90
Polymer exchange membrane (PEMFC)	$O_2+4H^++4e^-\rightarrow 2H_2O$	$2H_2\rightarrow 4H^++4e^-$	$2H_2+O_2\rightarrow 2H_2O$	50-125
Direct methanol (DMFC)	$CH_3OH+H_2O\rightarrow CO_2+6H^++6e^-$	$3/2O_2+6H^++6e^-\rightarrow 3H_2O$	$CH_3OH+3/2O_2\rightarrow CO_2+2H_2O$	50-120
Phosphoric acid (PAFC)	$2H_2\rightarrow 4H^++4e^-$	$O_2+4H^++4e^-\rightarrow 2H_2O$	$2H_2+O_2\rightarrow 2H_2O$	190-210
Molten carbonate (MCFC)	$2H_2+2CO_3^{2-}\rightarrow 2H_2O+2CO_2+4e^-$	$O2+2CO2+4e^-\rightarrow 2CO_3^{2-}$	$2H_2+O_2\rightarrow 2H_2O$	630-650

As hydrogen powered vehicles and fuel cells move into the mainstream there will be increased demand for hydrogen. It has been estimated that fourteen times the current worldwide production of hydrogen will be needed for a global energy market based on hydrogen.[207] With this increased demand, there will be a need for a low cost method to produce huge amounts of pure H_2; an efficient production method remains a huge obstacle.

In the United States, the majority of pure H_2 is produced by steam reforming of methane.[207] Huge reforming plants are currently the only economically viable method and the entire supply of a single plant is usually purchased by a single customer. Hydrogen must be harvested in this manner because steam reforming of methane is inherently inefficient.[207] Efficient catalysts are needed to assist with the production of H_2 in smaller plants located throughout the world to meet the demand .

The most likely reaction for the future production of H_2 appears to be the water gas shift reaction (WGS) shown in Equation 4.

$$CO + H_2O \rightarrow CO_2 + 2H_2 \qquad (4)$$

The advantage of the WGS reaction is that water is the source. The main drawback is the emission of CO_2 and its associated environmental problems. **Table 15** lists some of the alternative methods identified for the production of H_2.

Table 15. Alternative Methods for the Production of H_2.

Source	Reaction	Advantages	Disadvantages	Reference
Methane (CH_4)	$CO_2+CH_4 \rightarrow 2CO + 2H_2$	Can be used in conjunction with WGS reaction to reuse CO_2 and CO	CO_2 source must be pure or reaction may be inefficient, small amounts of C are produced	37
Methane (CH_4)	$CH_4 \rightarrow 2H_2 + C$	No CO or CO_2 produced	Huge amounts of elemental C must be removed to prevent catalyst fouling	37
Ethanol (C_2H_5OH)	$C_2H_5OH+2H_2O+1/2O_2 \rightarrow 2CO_2 +5H_2$	5 H_2 molecules produced per 3 total H_2 molecules, ethanol is widely produced from agricultural product, low C buildup on catalyst	The amount of energy required to create ethanol from corn may be greater than the amount of energy harvested from the reaction	28

The search for an efficient catalyst for the WGS reaction as well as other reactions that produce hydrogen has been widespread and several 1D ceramic nanostructures have been identified as potential catalysts. However, none of these systems yet meet the standards required of the catalyst in the operating conditions [78]:

- The catalyst for the WGS reaction must have high activity between 200 to 300°C for H_2 production in an automobile
- The catalyst must remain stable for multiple start up and shut down cycles
- The catalyst must have a lifetime of thousands of hours

One-dimensional ceramic nanostructures identified as potential catalysts for the oxidation of CO or other possible fuel cell energy sources include: Ag nanoparticles on MnO_2 nanowires (and phases) [17], SnO_2 nanowires [2], TiO_2 nanotubes with Au nanoparticles [15], CeO_2 nanowires [26, 27], and CNT with Pt nanoparticles [79, 81] Although these systems have proven to be efficient catalysts, huge opportunities remain for the development of a low temperature, inexpensive, efficient catalysts in the fuel cell industry.

7.2 Ultra Specific Sensors

One of the most troubling aspects of 1D nanostructure-based sensors has been the difficulty in making detectors sensitive to only one molecule or atom in the environment they are intended for without functionalizing the nanostructure surface. **Table 16** illustrates the problem for sensors operating on a change of . Several of the 1D nanostructures that have been demonstrated to be good candidates for gas sensors are sensitive to multiple individual molecules that would likely be common to environments encountered during sensor use. For example, **Figure 14** shows the effect of humidity on the impedence of TiO_2 nanowires. [63]

Table 16. Species Affecting □ of Nanostructured Sensors

Nanostructure	**Species Affecting □**	**References**
SnO_2 nanobelt or nanowire with various metal nanoparticles	H_2, O_2, NO_2, CO, Ethanol, N_2	2, 4, 8, 9, 39
CNT	O_2, NO_2, NH_3,	43,44, 46
Si nanowire	H_2O, NH_3	32
TiO_2 nanowire	H_2, H_2O	42, 63
ZnO nanowire	NO_2, NH_3, O_2	23, 24
In_2O_3 nanowire	NO_2, NH_3	5, 60

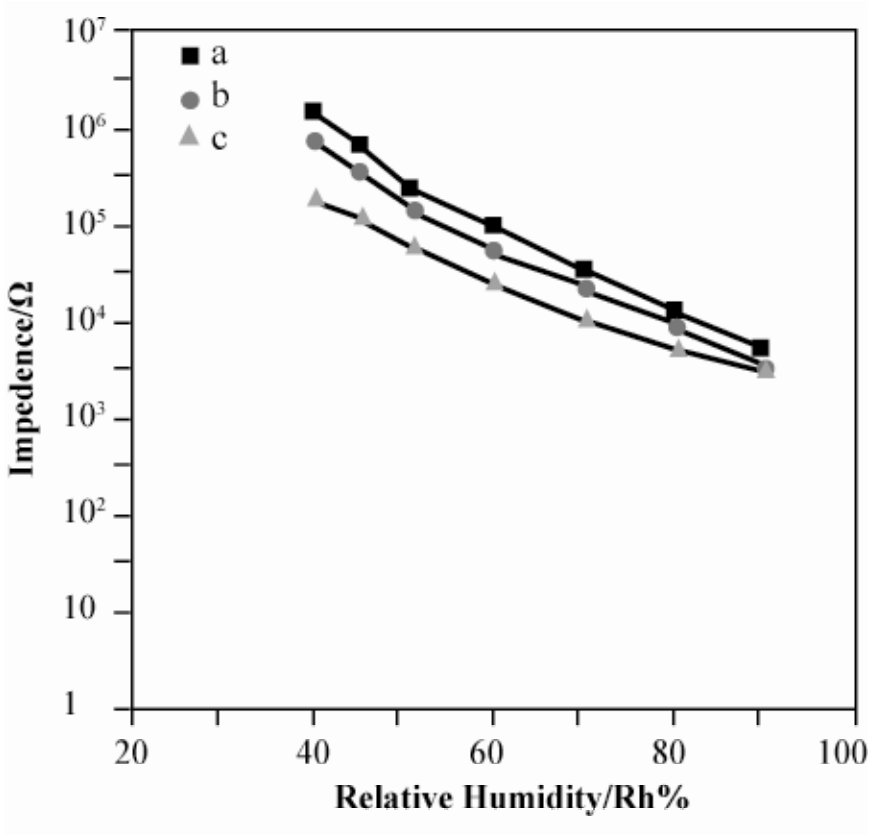

Figure 14. Effect of relative humidity (Rh) on the impedence of TiO_2 nanowire sensors at: (a) 17°C, (b) 25°C, and (c) 35°C. The data demonstrate the effect that other species in the sensing environment can have on the performance of 1D nanostructured sensors.[Data from 63]

Using multiple types of 1D nanostructures in a single detection device could be a step towards the creation of ultra selective sensors. For example, Si nanowires could be combined with TiO_2 nanowires in a single device to measure the concentration of H_2 or NH_3 in a certain environment. These two types of nanowires are both sensitive to H_2O vapor and could be used simultaneously in an environment known to be free of NH_3 or H_2. The Si nanowires could be used to gauge the concentration of H_2O in an environment void of NH_3 vapor, allowing for accurate detection of H_2 with TiO_2 nanowires by calibrating the effect of the H_2O on □ of the TiO_2 nanowires.

Ultra specific detection using 1D nanostructures may be aided by configuring the nanostructures into FET devices. Research has shown that the threshold gate voltage is different for individual devices when exposed to different gases that affect □.[23, 60] However, the threshold voltage of ZnO nanowires in FET configurations was also affected by the concentration of NO_2 and NH_3 gases that were being detected.[23] This result indicates that the presence of NO_2 and NH_3 could likely be identified by scanning the gate voltage of the FET, but the exact concentrations of each gas may be hard to determine since the concentration of each will alter the threshold voltages if both NO_2 and NH_3 are present.

There is some limited evidence that doping can enhance the selectivity of 1D nanostructures in sensor devices.[36] This cited study investigated the effect of Ru doping on the properties of SnO_2 nanowires. It was found that nanowires doped with 0.48% Ru were better for sensing NO_2, while SnO_2 nanowires doped with 0.23 % Ru were more effective for the detection of liquefied petroleum gas. This area clearly merits additional research.

7.3 Biomedical Applications

One-dimensional ceramic nanostructure sensors have the potential to revolutionize biomedical fields. Functionalized nanotubes and nanowires have already been proven to detect ultra low concentrations of specific DNA sequences and proteins that are nearly impossible to detect with alternative methods.[51, 52, 54, 55, 62] Similar sensors could be used for earlier detection of cancer or other diseases than is currently possible, which could lead to more effective treatment for patients. Since many ceramics are inert in human physiological fluids and are the ideal size for detection of individual proteins and other molecules in the body, it is possible that 1D ceramic nanostructures could be used as implanted as sensors for very early detection.

Ceramic nanostructures might also be perfect supports for metal nanoparticles used in biomedical sensing and catalyst applications. Metal nanoparticles have been demonstrated as detectors for a variety of analytes in blood, serum, and saline.[208, 209] In one study, Au nanoparticles were found to bound only to breast cancer cells when placed in a sample of healthy and cancerous cells.[210] A laser was then used to destroy the cancerous cells. These types of sensors are speculated as a method for early detection, diagnosis, and treatment of several diseases and infections.

7.4 Antiterrorism Devices

The detection of hazardous airborne materials has emerged as an important issue for public safety, reflected by the growing market for sensors of biohazardous molecules and toxic chemicals. The National Institute of Health provided approximately $1.6 billion for bioterrorism research in 2004.[211] The U.S. Food and Drug Administration has identified anthrax, plague, small pox, botulism, and Ebola as primary bioweapons that could have major impacts on public

health if used as a weapon.[212] Sensors capable of detecting very small concentrations of hazardous biomaterials are needed since exposure to a very small amount of these dangerous materials can infect individuals and lead to the transmission through the population.

The ideal sensor devices should be portable, offer fast detection, and be inexpensive enough that the devices can be purchased and placed in sites where terrorist attacks are most likely to occur. One-dimensional ceramic nanostructures offer all of the needed characteristics to be a perfect sensing elements; they are often small, require little power, and have extremely short detection times. Researchers at the NASA Ames Laboratory have developed a handheld sensor consisting of billions of vertically aligned CNT.[42] The CNT in these detectors have been functionalized to sense various biological molecules, mainly focusing on biomedical applications. However, it seems that a sensor of this type could be functionalized to sense hazardous materials, making the detector a good representative of the type of product ideal for counter terrorism applications.

7.5 Novel Production Techniques

There is a need to improve existing techniques, and to develop new ones, for making 1D ceramic nanostructures that may be useful in sensors and catalytic devices.[100, 102, 201, 213, 214] Alternative approaches for producing novel nanostructures (**Figure 15**) offer some exciting possibilities in this regard.

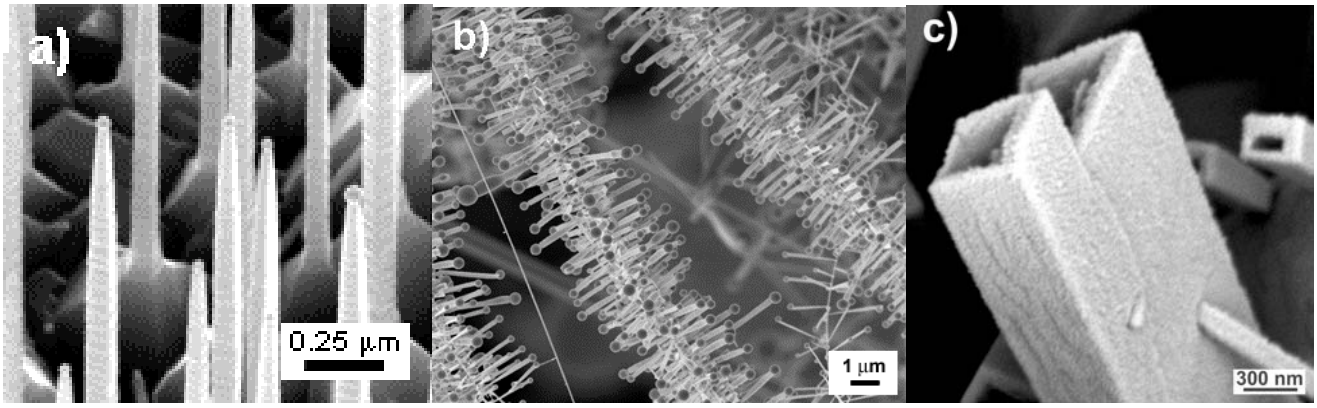

Figure 15. SEM images of various 1D nanostructures: (a) In_2O_3 nanowires with threads. Reprinted with permission from 201, P. Nguyen, H.T. Ng, T. Yamada, M.K. Smith, J. Li, J. Han, and M. Meyyappan, Nano Letters, 4, 651 (2004), Copyright @ American Chemical Society. (b) SnO_2 nanowire with SnO_2 nanobelts growing epitaxially from the surface Reprinted with permission from Ref. 102, P. Gao and Z. L. Wang, J. Phys. Chem. B, 106, 12653 (2002), Copyright @ American Chemical Society. Image courtesy of Prof. Z.L. Wang, Georgia Tech University. (c) SnO_2 nanotubes with rectangular cross section. Reprinted with permission from Ref. 214, Y. Liu and M. Liu, Adv. Func. Mater., 15, 57 (2005), Copyright @ Elsevier. Image courtesy of Y. Liu.

The aligned array of threaded In_2O_3 nanostructures was grown on a-plane sapphire using carbothermal reduction in conjunction with Au catalyst particles.[201] The nanowires formed epitaxially on the substrate in the <100> direction, followed by the formation of the threads to expose the {111} planes, likely lowering the overall surface energy of the nanostructures. These threaded structures could be useful as sensors or catalysts since the exposed planes were different from those typically observed in a nanostructure growth in the <100> direction. If the planes exposed by the threads are more active for adsorption of a certain species or show a higher catalytic activity for a desired reaction, the threaded structure will be effective in sensor or catalyst devices.

The branched ZnO nanowire/nanobelt arrays shown in Figure 15(b) were formed by thermal evaporation using a mixture of ZnO and SnO_2 powders as the source.[102] The central ZnO nanowires formed in the <0001> direction with a hexagonal cross section. Zinc oxide nanobelts subsequently grew epitaxially from this structure in the six <01-10> directions. This type of 1D nanostructure appears to have promise as a catalyst because of the increase in surface area.

The nanotubes shown in Figure 15(c) were formed with combustion CVD on quartz substrates in the temperature range of 850-1150°C. Each tube formed in the <001> direction and had {110} side planes. The nanotubes showed high sensitivity to ethanol vapor when tested as gas sensors. This type of morphology could also be useful as catalyst with high surface area and specifically exposed side walls.

8. Conclusions

As nanotechnology expands into large markets including the medical, automobile, and power production industries, next generation sensors and catalysts will be essential elements. One-dimensional ceramic nanostructures are an excellent option for sensors or catalysts in many of

these anticipated applications. Ceramic nanostructures exhibit quantum size effects and often have surface atoms that can easily change valence states, which makes them especially active where the adsorption of certain outside species is essential. The extremely small cross sectional area of these structures make them ideal for □-based sensors where an adsorbed species may change the carrier density by orders of magnitude.

Many methods for fabricating 1D ceramic nanostructures have been developed and several of these processes have been improved to the point that mass production of sets of nearly identical nanostructures seem on the verge of being economically feasible. Evaporation, CVD, solution, and template assisted growth methods have been widely studied, leading to advanced knowledge on how to grow crystallographically identical nanostructures with small size distributions and specific morphologies. Several viable methods for the deposition of metal nanoparticles on ceramic nanostructures, which often results in a system with enhanced sensing and catalytic properties, have also been developed. Both solution and vapor methods for the rapid deposition of metal nanoparticles have been established and may offer realistic options for device production.

Functionalized ceramic nanowires and nanotubes have already been shown to detect specific proteins, and ceramic nanowires and nanotubes with metallic nanoparticles have been demonstrated to efficiently catalyze reactions that are essential to the production of pure hydrogen. The key issue for the implementation of 1D nanostructure technology into sensor and catalyst devices is the improvement and development of methods to create functional devices. The size scale of 1D nanostructures increases the importance of device design since the nanostructures cannot be handled easily especially compared with materials used for conventional sensors and catalysts. Procedures that create devices with the direct manipulation of

single 1D nanostructures are not currently realistic for mass production, and many of them are highly complex. Early studies focused on methods to produce large amounts of identical 1D ceramic nanostructures. Current research should shift to ways to improve device fabrication and creative new approaches to directly integrate 1D ceramic nanostructures into reliable, reproducible devices.

There are great opportunities for research in specific sensor and catalyst applications where 1D ceramic nanostructures have already shown promise. In the search for alternative fuel sources, especially fuel cells, efficient catalysts will be tremendously important. The increased threat of terrorism through the use of biological or chemical weapons has driven up the demand for portable, highly sensitive detectors that can sense the presence of hazardous materials almost instantly. Ceramic nanowires and nanotubes have shown all the properties necessary for this application. Ultra sensitive, specific sensors are also desired in medical applications where early detection and treatment leads to better recovery rates. One-dimensional ceramic nanostructures can detect specific proteins and DNA sequences instantaneously, typically do not react with other body tissues, and are the perfect size to be used in medical applications.

References

1. F. Patolsky, and C.M. Lieber, Mater. Today, **20**, 2005.

2. Y. Zhang, A. Kolmakov, Y. Lilach, and M. Moskovits, J. Phys. Chem. B, **109**, 1923 (2005).

3. E. Comini, V. Guidi, C. Malagu, G. Marinelli, Z. Pan, G. Sberveglieri, and Z.L. Wang, J. Phys. Chem. B, **108**, 1882 (2004).

4. E. Comini, G. Faglia, G. Sberveglieri, Z. Pan, and Z. L. Wang, Appl. Phys. Lett., **81**, 1869 (2002).

5. D. Zhang, Z. Liu, C. Li, T. Tang, X. Liu, S. Han, B. Lei, and C. Zhou, Nano Lett., **4**, 1919 (2004).

6. J. Richter, M. Mertig, W. Pompe, I. Monch, and H.K. Schackert, Phys. Lett., **78**, 536 (2001).

7. M. Arnold, P. Avouris, Z. W. Pan, and Z. L. Wang, J. Phys. Chem. B, **107**, 659 (2003).

8. A. Kolmakov, D.O. Klenov, Y. Lilach, S. Stemmer, and M. Moskovits, Nano Lett., **5**, 667 (2005).

9. M. Law, H. Kind, B. Messer, F. Kim, and P. Yang, Agnew. Chem. Int. Ed., **41**, 2405 (2002).

10. A. Kolmakov, Y. Zhang, G. Cheng, and M. Moskovits, Adv. Mater., **15**, 997 (2003).

11. Y. Wang, X. Jiang, and Y. Xia, J. Am. Chem. Soc., **125**, 16176 (2003).

12. M.L. Kantam, K.B.S. Khumar, Ch. Sridhar, Adv. Synth. Catal., **347**, 1212 (2005).

13. J.H. Clark and D.J. Macquarrie, Chem. Commun., 853 (1998).

14. H.H. Kung, and M.C. Kung, Appl. Catal. A, **246**, 193 (2003).

15. V. Idakiev, X.Y. Yuan, T. Tabakova, B.L. Su, Appl. Catal. A, **281**, 149 (2005).

16. S.F. Yin, B.Q. Xu, C.F. Ng, and C.T. Au, Appl. Catal. B, **48**, 237 (2004).

17. R. Xu, X. Wang, D. Wang, K. Zhou, and Y. Li, J. Catal., **237**, 426 (2006).

18. R.A. Bennett, P. Stone, and M. Bowker, Faraday Discuss., **114**, 267 (1999).

19. S. Iijima, Nature, **354**, 56 (1991).

20. M. Haruta, Appl. Catal. A: General, **222**, 427 (2001).

21. M. Haruta, The Chemical Record, **3**, 75 (2003).

22. C. Baratto, E. Comini, G. Fagli, G. Sberveglieri, M. Zha, and A. Zappettini, Sensors and Actuators B, **109**, 2 (2005).

23. Z. Fan, and J. G. Lu, Appl. Phys. Lett, **86** 123510 (2005).

24. Q.H. Li, Y.X. Liang, X. Wan, and T.H. Wang, Appl. Phys. Lett., **85**, 6389 (2004).

25. Q. Wan, Q.H. Li, Y.J. Chen, T.H. Wang, X.L. He, J.P. Li and C.L. Lin, Appl. Phys. Lett., **84**, 3654 (2004).

26. K. Zhou, X. Wang, X. Sun, Q. Peng, and Y. Li, J. Catal., **229**, 206 (2005).

27. K. Zhou, R. Xu, X. Sun, H. Chen, X. Tian, D. Shen, and Y. Li, Catal. Lett., **101**, 169 (2005).

28. G.A. Deluga, J.R. Salge, L.D. Schmidt, and X.E. Verykios, Science, **303**, 993 (2004).

29. D.C. Meier, X. Lai and D.W. Goodman, *Surface Chemistry and Catalysis* edited by A.F. Carley, P.R. Davie, G.J. Hutchings and M.S. Spencer, Klumer Academic Plenum Publishers, New York (2002).

30. S. Shen, K. Hidajat, L.E. Yu, and S. Kawi, Adv. Mater., **16**, 541 (2004).

31. Z. Li, Y. Chen, X. Li, T.I. Kamins, K. Nauka, and R.S. Williams, Nano Lett., **4**, 245 (2004).

32. X.T. Zhou, J.Q. Hu, C.P. Li, D.D.D. Ma, C.S. Lee, and S.T. Lee, Chem. Phys. Lett., **369**, 220 (2003).

33. J. Hahm, and C.M. Lieber, Nano Lett., **4**, 51 (2004).

34. Z. Sun, H. Yuan, Z. Liu, B. Han, and X. Zhang, Adv. Mater., **17**, 2993 (2005).

35. J. Chen, L. Xu, W. Li, and X. Gou, Adv. Mater., **17**, 582 (2005).

36. N. S. Ramgir, I. S. Mulla, K. P. Vijayamohanan, Sensors and Actuators B, **107**, 708 (2005).

37. M. Law, H. Kind, B. Messer, F. Kim, and P. Yang, Angew. Chem. Int. Ed., **41**, 2405 (2002).

38. A. Maiti, J.A. Rodriguez, M. Law, P. Kung, J.R. McKinney, and P. Yang, Nano Lett. **3**, 1025 (2003).

39. W. Wan, and T.H. Wang, Chem. Commun., 3841 (2005).

40. Z. Ying, Q. Wan, Z.T. Song, and S.L. Feng, Nanotechnology, **15**, 1682 (2004).

41. Y. Xu, X. Zhou and O.T. Sorenson, Sens. Act. B, **65**, 2 (2000).

42. R.W. Bogue, Sensor Review, **24**, 253 (2004).

43. J. Kong, N.R. Franklin, C. Zhou, M.G. Chapline, S. Peng, K. Cho, and H. Dai, Science, **287**, 622 (2000).

44. J. Li, Y. Lu, Q. Ye, M. Cinke, J. Han, and M. Meyyappan, Nano Lett., **3**, 929 (2003),

45. A. Modi, N. Koratkar, E. Lass, B. Wei, and P.M. Ajayan, Nature, **424**, 171 (2003).

46. P.G. Collins, K. Bradley, M. Ishigami, and A. Zettl, Science, **287**, 1801 (2000).

47. H. Vedala, J. Huang, X.Y. Zhou, G. Kim, S. Roy, and W.B. Choi, Appl. Surf. Sci., **252**, 7987 (2006).

48. T. Someya, J. Small, P. Kim, C. Nuckolls, and J.T. Yardley, Nano Lett., **3**, 877 (2003).

49. M. Chen, and A. Gelprin, Nano Lett., **5**, 1774 (2005).

50. Y Lin, F. Lu, Y. Tu, and Z. Ren, Nano Lett., **4**, 191 (2004).

51. K. Besteman, J. Lee, F.G.M. Wiertz, H.A. Heering, and C. Dekker, Nano Lett., **3**, 727 (2003).

52. S. Roy, H. Vedala, and W. Choi, Nanotechnology, **17**, S14 (2006).

53. G. Li, J.M. Liao, G.Q. Hu, N.Z. Ma, and P.J. Wu, Biosensors and Bioelectronics, **20**, 2140 (2005).

54. X. Yu, D. Chattopadhyay, I. Galeska, F. Papadimitrakopoulos, and J.F. Rusling, Electrochem. Commun., **5**, 408 (2003).

55. C.V. Nguyen, L. Delzeit, A.M. Cassell, J. Han, and M. Meyyappan, Nano Lett., **2**, 1079 (2002).

56. S. Sotiropoulou, and N.A. Chaniotakis, Anal. Bioanal. Chem., **375**, 103 (2003).

57. M. Musameh, J. Wang, A. Merkoci, and Y. Lin, Electrochem. Commun., **4**, 743 (2002).

58. R.J. Chen, S. Bangsaruntip, K.A. Drouvalakis, N.W.S. Kam, M. Shim, Y. Li, W. Kim, P.J. Utz and H. Dai, Proc. Natl. Acad. Sci. U.S.A., **100**, 4984 (2003).

59. A. Star, J.C.P. Gabriel, K. Bradley and G. Gruner, Nano Lett., **3**, 459 (2003).

60. C. Li, D. Zhang, X. Liu, S. Han, T. Tang, J. Han, and C. Zhou, Appl. Phys. Lett. **82**, 1613 (2003).

61. M.W. Shao, Y.Y. Shan, N.B. Wong, and S.T. Lee, Adv. Funct. Mater., **15**, 1478 (2005).

62. Y. Cui, Q. Q. Wei, H. K. Park, and C.M. Lieber, Science **293**, 1289 (2001).

63. R.J. Wu, Y.L. Sun, C.C. Lin, H.W. Chen, and M. Chavali, Sensors and Actuators B, **115**, 198 (2006).

64. I. Raible, M. Burghard, U. Schlecht, A. Yasuda, and T. Vossmeyer, Sensors and Actuators B, **106**, 730 (2005).

65. W.Y. Li, L.N. Xu, J. Chen, Adv. Func. Mater., **15**, 851 (2005).

66. B.R. Weinberger, G.G. Peterson, T.C. Eschrich and H.A. Krasinski, J.Appl. Phys., **60**, 3232 (1986).

67. M.J. Sailor and E.J. Lee, Adv. Mater., **9**, 783 (1997).

68. J.T. Yates Jr., Science, **279**, 335 (1998).

69. A. Puzder, A.J. Williamson, J.C. Grossman and G. Galli, Phys. Rev. Lett., **88**, 097401 (2002).

70. X.H. Sun, H.Y. Peng, Y.H. Tang, W.S. Shi, N.B. Wong, C.S. Lee, and S.T. Lee, J. Appl. Phys., **89**, 6396 (2001).

71. X.Y. Zhang, L. Zhang, G.W. Meng, G.H. Li, N.Y. Jin-Phillip, and F. Phillip, Adv. Mater., **13**, 1238 (2001).

72. S.W. Chung, J. Y. Yu, and J.R. Heath, Appl. Phys. Lett., **76**, 2068 (2000).

73. L. Liu, G. Tan, V. Agarwal, A. Bose, J. He, G.L. McPherson, and V.T. John, Chem. Commun., 4517 (2005).

74. S.J. Limmer, S. Seraji, Y. Wu, T. P. Chou, C. Nguyen, and G. Cao, Adv. Funct. Mater., **12**, 59 (2002).

75. Z.L. Wang, J. Mater. Chem., **15**, 1021 (2005).

76. D. Terribile, A. Trovarelli, C. Leitenburg, and G. Dolcetti, Chem. Mater., **9**, 2676 (1997).

77. S. Carretin, P. Concepción, A. Corma, J.M. López,Nieto, and V.F. Puntes, Agnew. Chem. Int. Ed., **43**, 2538 (2004).

78. J.M. Zalc, V. Sokolovskii, and D.G. Löffler, J. Catal., **206**, 169 (2002).

79. C. Wang, M. Waje, X. Wang, J.M. Tang, R.C. Haddon, and Y. Yan, Nano Lett., **4**, 345 (2004).

80. W. Li, C. Liang, J. Qiu, W. Zhou, H. Han, Z. Wei, G. Sun, and Q. Xin, Carbon, **40**, 787 (2002).

81. Z. Liu, L.M. Gan, L. Hong, W. Chen and J.Y. Lee, J. Power Sources, **139**, 73 (2005).

82. X. Wang, and Y. Li, Agnew. Chem. Int. Ed., **41**, 4790 (2002).

83. Y. Zhang, N. Wang, S. Gao, R. He, S. Miao, J. Liu, J. Zhu and X. Zhang, Chem. Mater., **14**, 3564 (2002).

84. Z.R. Dai, Z.W. Pan, and Z.L. Wang, J. Phys. Chem. B, **106**, 902 (2002).

85. A. Di6guez, A. Romano-Rodriguez, J.R. Morante , U. Weimar, M. Schweizer-Berberich and W. G6pel, Sens. Act. B, **31**, 1 (1996).

86. R.S. Wagner and W.C. Ellis, Appl. Phys. Lett. , **4**, 89 (1964).

87. D.N. McIlroy, A. Alkhateeb, D. Zhang, D.E. Aston, AC Marcy and M.G. Norton, J. Phys. Cond. Matt., **16**, R415 (2004).

88. Y. Ando, X. Zhao, T. Sugai and M. Kumar, Mater. Today, , 22 (2004).

89. A.I. Persson, M.W. Larsson, S. Stenstrom, B.J. Ohlsson, L. Samuelson and L.R. Wallenberg, Nature, **3**, 677 (2004).

90. K.A. Dick, K. Deppert, T. Mårtensson, B. Mandl, L. Samuelson and W. Seifert, Nano Lett., **5**, 761 (2005).

91. X. Wang, C.J. Summers, and X.L. Wang, Nano Lett., **4**, 423 (2004).

92. H.T. Ng, J. Li, M.K. Smith, P. Nguyen, A. Cassell, J. Han, and M. Meyyappan, Science, **300**, 1249 (2003).

93. P. Nguyen, H.T. Ng, J. Kong, A.M. Cassell, R. Quinn, J. Li, J. Han, M. McNeil, and M. Meyyappan, Nano Lett., **3**, 925 (2003).

94. S.H.Sun, G.W. Meng, M.G. Zhang, X.H. An, G.S. Wu, and L.D. Zhang, J. Phys. D: Appl. Phys., **37**, 409 (2004).

95. C. Tang, S. Fan, M.L. de la Chapelle, H. Dang, and P. Li, Adv. Mater, **12**, 1346 (2000).

96. C.N.R. Rao, G. Gundiah, F.L. Deepak, A. Govindaraj, and A.K. Cheetham, J. Mater. Chem., **14**, 440 (2004).

97. X.S. Fang, C.H. Ye, L.D. Zhang, Y.H. Wang, and Y.C. Wu, Adv. Func. Mater., **15**, 63 (2005).

98. Z.W. Pan, Z.R. Dai, and Z.L. Wang, Science, **291**, 1947 (2001).

99. S. Kumar, S. Rajaraman, R.A. Gerhardt, Z.L. Wang, and Pr.J. Hesketh, Eletrochimica Acta, **51**, 943 (2005).

100. Y.X. Chen, L.J. Campbell, W.L. Zhou, J. Crystal Growth, **270**, 505 (2004).

101. M.S. Arnold, P. Avouris, Z.W. Pan and Z.L. Wang, J. Phys. Chem. B, **107**, 659 (2003).

102. P. Gao and Z.L. Wang, J. Phys. Chem. B, **106**, 12653 (2002).

103. C. Li, D. Zhang, S. Han, X. Liu, T. Tang and C. Zhou, Adv. Mater., **15**, 143 (2003).

104. Z.W. Pan, Z.R. Dai and Z.L. Wang, Appl. Phys. Lett., **80**, 309 (2002).

105. Q. Zhao, H. Z. Zhang, B. Xiang, X.H. Luo, X.C. Sun and D.P. Yu, Appl. Phys. A, **79**, 2033 (2004).

106. Y. Liu, Z. Liu and G. Wang, Appl. Phys. A, **76**, 1117 (2003).

107. M.S. Gudiksen, J. Wang, and C.M. Lieber, J. Phys. Chem. B, **105**, 4062 (2001).

108. L. Schubert, P. Werner, N.D. Zakharov, G. Girth, F. M. Kolb, L. Long, U. Gösele, and T. Y. Tan, Appl. Phys. Lett., **84**, 4968 (2004).

109. X. Jiang, T. Herricks, and Y. Xia, Nano Lett., **2**, 1333 (2002).

110. X.L. Ma, Y. Li, Y.L. Zhu, Chem. Phys. Lett., **376**, 794 (2003).

111. T.C. Wong, C.C. Yu, and J.J. Wu, Adv. Funct. Mater., **15**, 1440 (2005).

112. R. Fan, Y. Wu, D. Li, M. Yue, A. Majumdar, and P. Yang, J. Am. Chem. Soc., **125**, 5254 (2003).

113. D. Zhang, A. Alkhateeb, H. Han, H. Mahmood, D.N. McIlroy, and M.G. Norton, Nano Lett., **3**, 983 (2003).

114. D.N. McIlroy, D. Zhang, Y. Kranov and M.G. Norton, Appl. Phys. Lett., **79**, 1540 (2001).

115. V. Dobrokhotov, D.N. McIlroy, M.G. Norton, A. Abuzir, W.J. Yeh, I. Stevenson, R. Pouy, J. Bochenek, M. Cartwright, L. Wang, J. Dawson, M. Beaux and C. Berven, J. Appl. Phys., 99, 104302 (2006).

116. D. N. McIlroy, D. Zhang, R.M. Cohen, J. Wharton, Y. Geng, M.G. Norton, G. De Stasio, B. Gilbert, L. Perfetti, J.H. Streiff, B. Brooks, and J.L. McHale, Phys. Rev. B 60, 4874 (1999).

117. D. Zhang, D.N. McIlroy, Y. Geng, and M.G. Norton, J. Mat. Sci. Lett., 18 349 (1999).

118. M. Saifislam, S. Sharma, T.I. Kamins and R.S. Williams, Appl. Phys. A, 80, 1133 (2005).

119. Y. Wu, H. Yan, P. Yang, Top. Catal., 19, 197 (2002).

120. O.R. Lourie, C.R. Jones, B.M. Bartlett, P.C. Gibbons, R.S. Ruoff, and W.E. Buhro, Chem. Mater., 12, 1808 (2000).

121. P. Nguyen, H.T. Ng, and M. Meyyappan, Adv. Mater., 17, 1773 (2005).

122. J.C. Wang, S.Q. Feng, D.P. Yu, Appl. Phys. A: Materials Science & Processing, 75, 691(2002).

123. W. Shi, Y. Zheng, N. Wang, C.S. Lee, and S.T. Lee, Adv. Mater., 13, 591 (2001).

124. M.S. Gudikson and C.M. Lieber, J. Am. Chem. Soc., 122, 8801 (2000).

125. Y. Cai, S.K. Chan, I.K. Sou, Y.F. Chan, D.S. Su, and N. Wang, Adv. Mater., 18, 109 (2004)

126. J. Hu, T.W. Odom, and C.M. Lieber, Acc. Chem. Res., 32, 435 (1999).

127. B. Lei, C. Li, D. Zhang, T. Tang and C. Zhou, Appl. Phys. A, 79, 439 (2004).

128. X. Duan and C.M. Lieber, Adv. Mater., 12, 298 (2000).

129. X. Duan, and C.M. Lieber, J. Am. Chem. Soc., 122, 188 (2000).

130. A.M. Morales and C.M. Lieber, Science, 279, 208 (1998).

131. K.A. Jeon, J.H. Kim, and S.Y. Lee, Progress in Solid State Chemistry, 1 (2005).

132. X. Duan, J. Wang, and C. Lieber, Appl. Phys. Lett., 76, 1116 (2000).

133. J.D. Holmes, K.P. Johnston, R.C. Doty, and B.A. Kogel, Science, 287, 1471 (2000).

134. J.Q. Lu and S.S. Yi, Langmuir, 22, 3951 (2006).

135. D.F. Zhang, L.D. Sun, J.L. Yin, C.H. Yan, Adv. Mater., 15, 1022 (2003).

136. J. Zhan, X. Yang, D. Wang, S. Li, Y. Xie, Y. Xia, and Y. Qian, Adv. Mater., 12, 1348 (2000).

137. K. Tang, Y. Qian, J. Zeng, and X. Yang, Adv. Mater., 15, 448 (2003).

138. T.J. Trentler, S.C. Goel, K.M. Hickman, A.M. Viano, M.Y. Chiang, A.M. Beatty, P.C. Gibbons, and W.E. Buhro, J. Am. Chem. Soc., 119, 2172 (1997).

139. T. Hanrath and B.A. Korgel, J. Am. Chem. Soc., 124, 1424 (2002).

140. X. Wang and Y. Li, J. Am. Chem. Soc., 124, 2880 (2002).

141. Z. Gu, Y. Ma, W. Yang, G. Zhang, and J. Yao, Chem. Commun., 3597 (2005).

142. L. Manna, E.C. Scher, and A.P. Alivisatos, J. Am. Chem. Soc., 122, 12700 (2000).

143. T. Kasuga, M. Hiramatsu, A. Hoson, T. Sekino, and K. Niihara, Adv. Mater, 11, 1307 (1999).

144. Z.Y. Yuan, J.F. Colomer and B.L. Su, Chem. Phys. Lett., 363, 362 (2002).

145. L. Vayssieres, Adv. Mater., 15, 464 (2003).

146. W.Q. Han, L. Wu and Y. Zhu, J. Am. Chem. Soc., 127, 12814 (2005).

147. Y. Lei, L.D. Zhang, G.W. Meng, G.H. Li, X.Y. Zhang, C.H. Liang, W. Chen, and S.X. Wang, Appl. Phys. Lett., 78, 1125 (2001).

148. Y. Li, G.W. Meng, and L.D. Zhang, Appl. Phys. Lett., 76, 2011 (2000).

149. D.T. Mitchell, S.B. Lee, L. Trofin, N. Li, T.K. Nevanen, H. Söderlund and C.R. Martin, J. Am. Chem. Soc., 124, 11864 (2002).

150. S.J. Limmer, S. Seraji, M.J. Forbess, Y. Wu, T.P. Chou, C. Nguyen, and G. Cao, Adv. Mater., 13, 1269 (2001).

151. S.S. Kim, C. Chun, J.C. Hong, and D.Y. Kim, J. Mater. Chem., 16, 370 (2006).

152. Y. Wang, K. Takahashi, H. Shang, and G. Cao, J. Phys. Chem. B, 109 3085 (2005).

153. Y.K. Choi, J. Zhu, J. Grunes, J. Bokor and G.A. Somorjai, J. Phys. Chem. B, 107, 3340 (2003).

154. J.A. Rogers, K.E. Paul, R.J. Jackman, and G.M. Whitesides, Appl. Phys. Lett., 70, 2658 (1997).

155. J.C. Hulteen and C.R. Martin, J. Mater. Chem., 7, 1075 (1997).

156. Y. Xia, P. Yang, Y. Sun, Y. Wu, B. Mayers, B. Gates, Y. Yin, F. Kim, and H. Yan, Adv. Mater., 15, 353 (2003).

157. S.O. Obare, N.R. Jana, and C.J. Murphy, Nano Lett., 1, 601 (2001).

158. J. Richter, M. Mertig, W. Pompe, I. Monch, and H.K. Schackert, Phys. Lett. 78, 536 (2001).

159. T. Scheibel, R. Parthasarathy, G. Sawicki, X.-M. Lin, H. Jaeger, and S.L. Lindquist, Proc. Natl Acad. Sci. 100, 4527 (2003).

160. S. Han, C. Li, Z. Liu, B. Lei, D. Zhang, W. Jin, X. Liu, T. Tang, and C. Zhou, Nano Lett., 4, 1241 (2004).

161. Y.S. Min, E.J. Bae, K.S. Jeong, Y.J. Cho, J.H. Lee, W.B. Choi, G.S. Park, Adv. Mater., 15, 1019 (2003).

162. R.A. Beckman, E. Johnston-Halperin, N.A. Melosh, Y. Luo, J.E. Green, and J.R. Heath, J. Appl. Phys., 96, 5921 (2004).

163. N.A. Melosh, A. Boukai, F. Diana, B. Gerardot, A. Badolato, P.N. Petroff, and J.R. Heath, Science, 300, 112 (2003).

164. S.M. Liu, M. Kobayashi, S. Sato, and K. Kimura, Chem. Commun., 4691 (2005).

165. T. Seeger, P. Kohler-Redlich, and M. Rühle, Adv. Mater., 12, 279 (2000).

166. N. Sano, J. Nakano and T. Kanki, Carbon, 42, 686 (2004).

167. K. Peng, J. Hu, Y. Yan, Y. Wu, H. Fang, Y. Xu, S. Lee, and J. Zhu, Adv. Funct. Mater., 16, 387 (2006).

168. Z.L. Xiao, C.Y. Han, U. Welp, H.H. Wang, W.K. Kwok, G.A. Willing, J.M. Hiller, R.E. Cook, D.J. Miller and G.W. Crabtree, Nano Lett., 2, 1293 (2002).

169. T. Ikuno, M. Katayama, M. Kishida, K. Kamada, Y. Murata, T. Yasuda, S. Honda, J.G. Lee, H. Mori and K. Oura, Jpn. J. Appl. Phys., 43, L644 (2004).

170. Y. Zhang, Q. Zhang, Y. Li, N. Wang and J. Zhu, Solid State Commun., 115, 51 (2000).

171. X.R. Ye, Y. Lin and C.M. Wai, Chem. Commun., 642 (2003).

172. A.D. Lalonde, M.G. Norton, D.N. McIlroy, D. Zhang, R. Padmanabhan, A. Alkhateeb, H. Han, N. Lane and Z. Holman, J. Mater. Res. 20, 549 (2005).

173. A.D. Lalonde, M.G. Norton, D. Zhang, D. Gangadean, A. Alkhateeb, R. Padmanabhan and D.N. McIlroy, J. Nanoparticle Res., 8, 99 (2006).

174. R. Zanella, S. Giorgio, C.R. Henry and C. Louis, J. Phys. Chem. B, 106, 7634 (2002).

175. J.D. Grunwaldt, C. Kiener, C. Wögerbauer and A. Baiker, J. Catal., 181, 223 (1999).

176. R.M. Penner, J. Phys. Chem. B, 106, 3339 (2002).

177. H. Liu, F. Favier, K. Ng, M.P. Zach, and R.M. Penner, Electrochimica Acta, 47, 671 (2001).

178. M. Endo, Y.A. Kim, M. Ezaka, K. Osada, T. Yanagisawa, T. Hayashi, M. Terrones, and M.S. Dresselhaus, Nano Lett., 3, 723 (2003).

179. Z. Liu, L.M. Gan, L. Hong, W. Chen and J.Y. Lee, J. Power Sources, 139, 73 (2005).

180. K. Jiang, A. Eitan, L.S. Schadler, P.M. Ajayan, and R.W. Siegel, Nano Lett., 3, 275 (2003).

181. Q. Li, S. Fan, W. Han, C. Sun and W. Liang, Jpn. J. Appl. Phys., 36, L501 (1997).

182. Q. Li and C. Wang, Chem. Phys. Lett., 375, 525 (2003).

183. B. Wen, C. Hiu, and Y. Liu, J. Phys. Chem. B., 109, 12372 (2005).

184. X.R. Ye, Y. Lin, C. Wang, M.H. Englehard, Y. Wang and C.M. Wai, J. Mater. Chem. B, 107 8294 (2004).

185. D.D.D. Ma, C.S. Lee, F.C.K. Au, S.Y. Tong, S.T. Lee, Science, 299, 1874 (2003).

186. C.R. Perrey and C.B. Carter, J. Mater. Sci., 41, 2711 (2006).

187. K.T. Jung, and A.T. Bell, Catal. Lett., **80**, 63 (2002).

188. Z.L. Wang, *Nanowires and Nanobelts Materials, Properties and Devices*, Kluwer Academic Publishers, Boston (2003).

189. L. Guczi, G. Peto, A. Beck, K. Frey, O. Geszti, G. Molnar, and C. Daroczi, J. Am. Chem. Soc., **125**, 4332 (2003).

190. D.A.H. Cunningham, W. Vogel, H. Kageyama, S. Tsubota and M. Haruta, J. Catal., **177**, 1 (1998).

191. R. Schögl, and S.B.A. Hamid, Agnew. Chem. Int. Ed., **43**, 1628 (2004).

192. Y. Iizuka, T. Tode, T. Takao, K. Yatsu, T. Takeuchi, S. Tsubota, and M. Haruta, J. Catalysis, **187**, 50 (1999).

193 X. Fu, H. Saltsburg, and M. Flytzani-Stephanopoulos, Science, **301**, 935 (2003).

194. C.T. Campbell, Science, **306**, 234 (2004).

195. Y Huang, X. Duan, Q. Wei, and C. Lieber, Science, **291**, 630 (2001).

196. F. Kim, S. Kwan, J. Akana, and P. Yang, J. Am. Chem. Soc., **123**, 4360 (2001).

197. B. Messer, J.H. Song, and P. Yang, J. Am. Chem. Soc., **122**, 10232 (2000).

198. Y. Cui, X. Duan, Y. Huang and C.M. Lieber, *Nanowires and Nanobelts Materials, Properties and Devices* edited by Z.L. Wang, Kluwer Academic Publishers, Boston (2003).

199. M. Diehl, S.N. Yaliraki, R.A. Beckman, M. Barahona, and J.R. Heath, Angew. Chem. Int. Ed., **41**, 353 (2002).

200. C. Klinke, J.B. Hannon, A. Afzali and P. Avouris, Nano Lett., **6**, 906 (2006).

201. P. Nguyen, H.T. Ng, T. Yamada, M.K. Smith, J. Li, J. Han, and M. Meyyappan, Nano Letters, **4**, 651 (2004).

202. H.T. Ng, J. Han, T. Yamada, P. Nguyen, Y. P. Chen, and M. Meyyappan, Nano Lett., **4**, 1247 (2004).

203. M.S. Dresselhaus, Basic Research Needs for the Hydrogen Economy, Neutrons & Energy for the Future, Office of Science of the U.S. Department of Energy, 4 June, 2004.

204. J. Muller and J. Fahey, Forbes, **174**, 46 (2004).

205. L. Carrette, K. A. Friedrich, U. Stimming, Chem. Phys. Chem., **1**, 162 (2000).

206. G.J.K. Acres and G.A. Hards, Phil Trans. R Soc. Lond. A, **354**, 1671 (1996).

207. J.N. Armor, Catal. Lett., **101**, 131 (2005).

208. L.R. Hirsch, R.J. Stafford, J.A. Bankson, S.R. Sershen, B. Rivera, R.E. Price, J.D. Hazle, N.J. Halas and J.L. West, Analyt. Chem., **75**, 2377 (2003).

209. N. Holstrum, P. Nilsson, J. Carlsten and S. Bowland, Biosens. and Bioelect., **13**, 1287 (1998).

210. L.R. Hirsch, A.M. Gobin, A.R. Lowery, F. Tam, R.A. Drezek, N.J. Halas and J.L. West, Annals Biomed. Eng., **34**, 15 (2006).

211. R.M. Atlas, Nature Rev. Micro., **1**, 70 (2003).

212. E. Niiler, Nature Biotech., **20**, 21 (2002).

213. X.M. Cai, A.B. Djurisic, and M.H. Xie, J. Appl. Phys, **98**, 074313 (2005).

214. Y. Liu and M. Liu, Adv. Func. Mater., **15**, 57 (2005).

B. TEFLON AF/Ag NANOCOMPOSITES WITH TAILORED OPTICAL PROPERTIES

Teflon AF/Ag nanocomposites with tailored optical properties

H. Eilers[a] and A. Biswas[b]
Institute for Shock Physics, Washington State University, Spokane, Washington 99210
T.D. Pounds and M. Grant Norton
School of Mechanical and Materials Engineering, Washington State University, Pullman, Washington 99164
M. Elbahri
Chair for Multicomponent Materials, Faculty of Engineering, Christian Albrechts University, D-24143, Kiel, Germany

(Received 13 February 2006; accepted 5 May 2006)

Teflon AF/Ag nanocomposites with various metal concentrations were fabricated by an evaporation process. Transmission electron microscopy examination showed that for low metal concentrations, the silver formed isolated individual nanoparticles. At higher metal concentrations, percolating metallic networks within the polymer matrix were formed. Optical absorption measurements showed a transition from individual plasmon absorption peaks for individual Ag nanoparticles to broadband optical absorption for the metallic networks. The absorption profile closely matches the solar radiation spectrum for an intermediate metal concentration of 45%. Thus, these novel polymer-metal nanocomposites have significant potential for photovoltaic applications.

The desire to create new materials with improved optical properties has led many researchers to synthesize nanometer-scale composites. As an example, polymer–metal nanocomposites, consisting of metallic nanoparticles embedded in various polymer matrices, have been evaluated for their novel functional properties, including optical, electronic, magnetic, and chemical.[1,2]

Polymer–metal nanocomposites can absorb light by the excitation of surface plasmons (oscillations of the electron gas) in the nanometer-sized metal particles. The resonance frequency of this oscillation depends on the size of the metal particles, their shape, and the type of metal.[3] When the frequency of the incoming light is close to the resonance frequency of the surface plasmon, strong absorption can occur.[4] Surface plasmon resonance (SPR) occurs normally in the visible part of the electromagnetic spectrum; the typical resonance frequency for spherical Ag nanoparticles is at about 400 nm.[3,4] However, nanostructures with specific shapes and structures can exhibit SPRs at longer wavelengths into the infrared (IR) region.

Surface plasmons have been investigated by many authors[5,6] for various applications, including surface-enhanced Raman scattering (SERS) in which a roughened metal layer on a dielectric is used to enhance the Raman scattering signal from an absorbed sample species.[4] The strongly enhanced signal allows for single-molecule detection. Surface plasmons are also used in the form of dielectric nanoparticles capped with a metallic layer.[7] The spectral response of such a capped nanoparticle depends on the size of the nanoparticles and the thickness of the shell. By varying the size and thickness, the plasmon resonance can be tuned to different wavelengths. Other applications include color filters,[8–11] all-optical switching devices,[12] photonic band gap materials,[13,14] and efficient Bragg reflectors.[15,16]

We have recently reported on the broadband plasmonic absorption of Teflon AF/Ag nanocomposites near the percolation threshold for potential photovoltaic and sensor applications.[17] It has been shown that surface plasmons can eject electrons, generating a photocurrent,[18] and enhanced absorption in polymer–metal nanocomposites for solar-cell application was observed.[19] Our goal is to develop materials with a spectral absorption closely matching the solar radiation spectrum. In this paper, we present significant progress in meeting this goal.

Polymer-based materials with plasmonic absorption bands that overlap with the solar radiation intensity profile (300–2500 nm)[20,21] are of interest for next-generation high-efficiency, low-cost solar cells. However, tailoring the optical absorption of a material to match the solar spectrum is not straightforward. A systematic investigation of the effects of metal concentration

Address all correspondence to these authors.
[a]e-mail: eilers@wsu.edu
[b]Present address: Office of Electronic Miniaturization, University of Alaska-Fairbanks, Fairbanks, AK 99709
e-mail: ffab2@uaf.edu
DOI: 10.1557/JMR.2006.0267

in the polymer matrix and nanoparticle size distribution and shape distribution on the plasmon resonance absorption is needed.

In this paper we report the morphological and optical properties of Teflon AF/Ag nanocomposites with metal concentrations ranging from 15% to 65% and demonstrate how the optical properties (in the visible and IR) of these nanocomposites dramatically change with metal concentration. Significantly, our study revealed that nanocomposites with a metal concentration of about 45% exhibit a plasmon absorption band that closely matches the full solar spectrum.

Polymer–metal nanocomposites were fabricated in a vacuum chamber equipped with a four-pocket mini-evaporator. A detailed description of this chamber is given elsewhere.[17] This evaporation system allows for sequential as well as parallel evaporation of up to four different materials. For the synthesis of Teflon AF/Ag nanocomposites, one pocket was filled with Teflon AF (grade 2400, granulates, DuPont, Wilmington, DE) and a second pocket was filled with silver (Alfa Aesar, Ward Hill, MA, 99.999%, 1-mm-diameter wires). Sapphire substrates were attached to a heatable substrate holder, which was set to 120 °C. Shutters were used to prevent premature deposition, and a quartz crystal was used to monitor the evaporation rates. The relative evaporation rates were adjusted to fabricate nanocomposites with metal concentrations of 15%, 30%, 45%, 60%, and 65%. The thickness of the films was about 60 nm.

The samples were characterized using transmission electron microscopy (TEM; Philips CM200, Eindhoven, The Netherlands, operated at 200 kV) to provide information on the particle shape, crystal structure, particle size, level of agglomeration, and particle size distribution. Transmission and reflection measurements (Perkin-Elmer Lambda 900, Boston, MA) were performed by M. Elbahri (Kiel, Germany) and were used to determine the spectral response. Absorption data were determined from the reflection and transmission data. We neglected scattering effects in our analysis because the samples appeared very clear, and angle-resolved measurements did not show any angular dependence.[17]

Figure 1 shows TEM images of Teflon AF/Ag nanocomposites. The silver concentration increases from 15% [Fig. 1(a)] to 65% [Fig. 1(e)]. These nominal concentrations are based upon the deposition rates and have an estimated error of ±5%. As the concentration increases, the size of the metal particles increases. The two images with the lowest concentration [Figs. 1(a) and 1(b)] show mostly spherical particles. The third image [Fig. 1(c)] shows larger nonspherical particles that appear to be the result of two or more spherical particles growing together. As the metal concentration is increased even further, particles continue to grow into larger irregularly shaped particles. When the percolation threshold is reached, a conductive metallic path is formed inside the polymer matrix. Shalaev has shown that when the metallic network forms a fractal structure, it can absorb a wide range of plasmon frequencies; i.e., many different frequencies can resonate somewhere within this percolating network.[4]

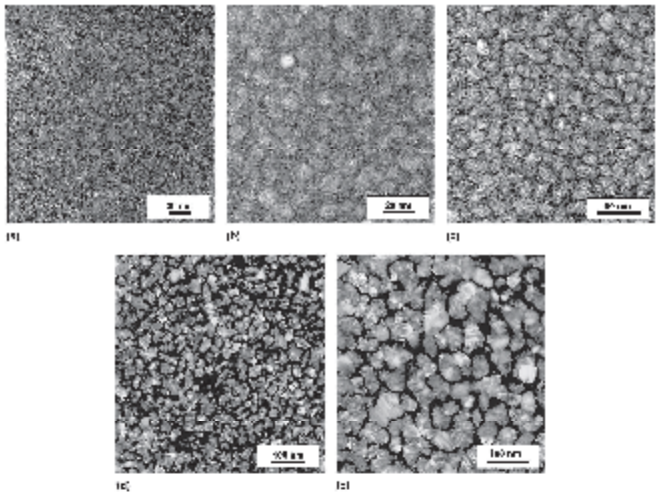

FIG. 1. TEM images of Teflon AF/Ag nanocomposites with metal concentrations of (a) 15%, (b) 30%, (c) 45%, (d) 60%, and (e) 65%. Note the different length scales of the images.

Figure 2 shows the transmission, reflection, and absorption spectra of the Teflon AF/Ag nanocomposites. The spectra clearly show how the plasmon resonance shifts to longer wavelength as the metal concentration increases. As the percolation threshold is approached, the absorption becomes very broad, covering a wide range of wavelengths. A flat and broadband absorption stretching well beyond 3000 nm into the mid IR is observed for a metal concentration of about 65%. Further measurements in the longer wavelengths were not possible due to the limitations of our spectrometer. The results indicate a dramatic switch from clearly distinguishable absorption peaks in the visible wavelength region to broadband absorption covering the visible and IR wavelengths as the metal concentration increases.

For nanocomposites with a metal content well below the percolation threshold (e.g., 15%), the Ag nanoparticles are isolated with a relatively narrow particle size and shape distributions [Fig. 1(a)]. The plasmon resonance in the visible wavelength region is largely due to dipolar type excitations.[3]

A broad distribution of particle shapes and sizes [Figs. 1(d) and 1(e)] results in a broad distribution of resonance frequencies. When the filler concentration of the metallic nanoparticles is close to the percolation threshold (i.e., a continuous metallic pathway is created), whole clusters of metallic nanoparticles can start to oscillate, and surface plasmons will be localized within the cluster. Surface plasmons, spread over larger clusters, will absorb at longer wavelengths than surface plasmons on individual nanoparticles. A collection of clusters with varying sizes will therefore absorb light over a broad spectral range.[22]

Further, the oscillations of the electron gas can lead to strongly enhanced electric fields within the inter-particle gaps. For Ag nanoparticles, the internal field can exceed the external field by up to a factor of 50.[4] This strong internal electric field can eject excited electrons from the surface plasmons. These electrons will be conducted along the percolation path by an applied bias voltage.[23] It has been shown that these electrons do not readily recombine with the holes in the metal clusters.[18] Moreover, a jump of several orders of magnitude in the current density has been observed in percolating Ag-polymer nanocomposites.[23] Such properties are extremely useful for photovoltaic applications.

Figure 3 shows the plasmonic absorption of a Teflon AF/Ag nanocomposite with a metal content of about 45% and the simulated solar radiation spectrum, demonstrating the close match. As can be seen in Fig. 1(c), a metal concentration of about 45% results in a Ag nanostructure forming an interpenetrating network. The combination of this feature and an optical absorption closely matching the solar radiation spectrum is important for high-efficiency photovoltaic devices as described in our

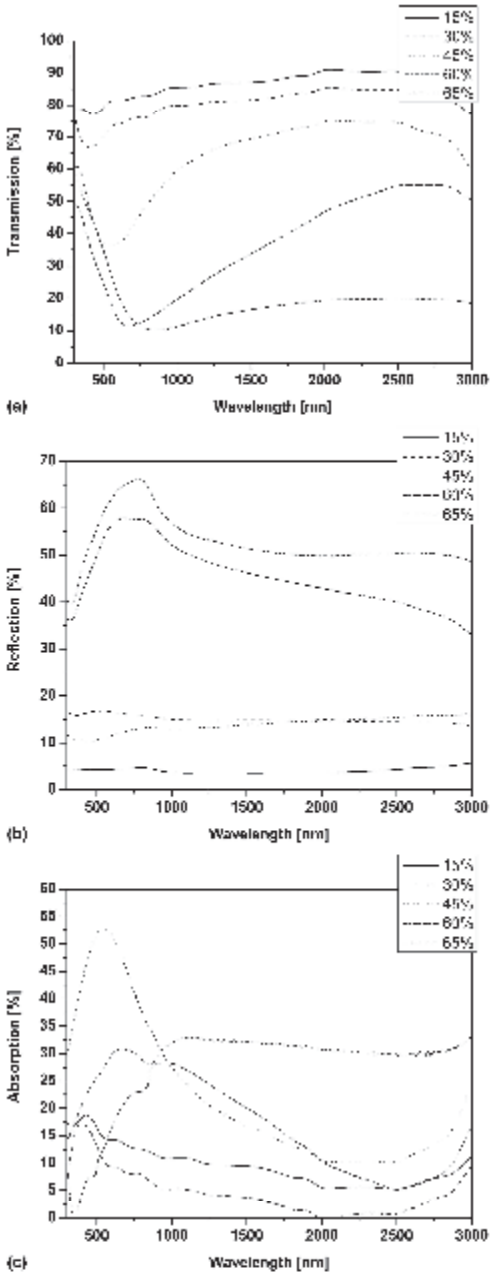

FIG. 2. (a) Transmission, (b) reflection, and (c) absorption of Teflon AF/Ag nanocomposites.

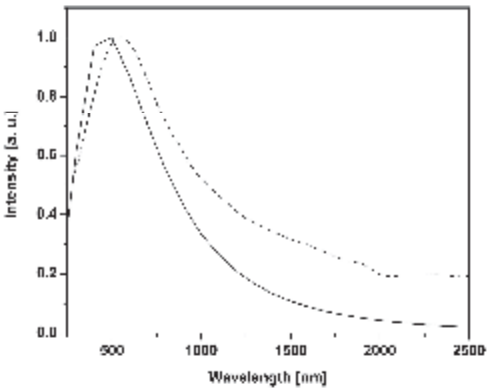

FIG. 3. The solid curve shows the Planck distribution for 6000 K (simulation of solar radiation), and the dashed curve shows the absorption of the polymer–metal nanocomposite with a metal concentration of about 45%.

earlier work.[17] While a percolating structure [Figs. 1(d) and 1(e)] provides a perfect interpenetrating metallic network, the highly conducting paths may create an electrical short between the electrodes sandwiching the active layer. Nanocomposites with relatively low metal contents (45%) would reduce the probability of electrical shorts between the electrodes while maintaining sufficiently high charge mobility via the formed pathways and electron tunneling.

We have demonstrated that the optical absorption of Teflon AF/Ag nanocomposites can be tailored to match the full solar spectrum. This occurs when the metal concentration is at about 45%. This absorption is due to surface plasmons in silver nanoparticles that have a distribution of particle sizes and shapes. We are currently investigating the electrical performance of these materials and how they can be incorporated into photovoltaic devices.

ACKNOWLEDGMENT

This work was support by the Office of Naval Research under Grant No. N00014-03-1-0247.

REFERENCES

1. *Metal-Polymer Nanocomposites*, edited by L. Nicolais and G. Carotenuto (Wiley Interscience, Hoboken, NJ, 2005).
2. A. Heilmann: *Polymer Films with Embedded Metal Nanoparticles*, Springer Series in Materials Science, Vol. 52 (Springer-Verlag, Berlin, Heidelberg, New York, 2003).
3. U. Kreibig and M. Vollmer: *Optical Properties of Metal Clusters*, Springer Series in Materials Science, Vol. 25 (Springer-Verlag, Berlin, Heidelberg, New York, 1995).
4. V.M. Shalaev: Optical nonlinearities of fractal composites, in *Optical Properties of Nanostructured Random Media*, Topics in Applied Physics, Vol. 82, edited by V.M. Shalaev (Springer-Verlag, Berlin, Heidelberg, Germany, 2002), pp. 93–114.
5. U. Schürmann, W.A. Hartung, H. Takele, V. Zaporojtchenko, and F. Faupel: Controlled syntheses of Ag-PTFE nanocomposite thin films by co-sputtering from two magnetron sources. *Nanotechnology* 16, 1078 (2005).
6. H. Takele, U. Schürmann, H. Greve, D. Paretkar, V. Zaporojtchenko, and F. Faupel: Controlled growth of Au nanoparticles in co-evaporated metal/polymer composite films and their optical and electrical properties, *Eur. Phys. J. Appl. Phys.* 33, 83 (2006).
7. N. Halas: Playing with plasmons: Tuning the optical resonant properties of metallic nanoshells. *MRS Bull.* 30, 362 (2005).
8. A. Biswas, O.C. Aktas, U. Schürmann, U. Saeed, V. Zaporojtchenko, F. Faupel, and T. Strunskus: Tunable multiple plasmon resonance wavelengths response from multicomponent polymer-metal nanocomposite systems. *Appl. Phys. Lett.* 84, 2655 (2004).
9. A. Biswas, O.C. Aktas, J. Kanzow, U. Saeed, T. Strunskus, V. Zaporojtchenko, and F. Faupel: Polymer–metal optical nanocomposites with tunable particle plasmon resonance prepared by vapor phase co-deposition. *Mater. Lett.* 58, 1530 (2004).
10. Y. Dirix, C. Bastiaansen, W. Caseri, and P. Smith: Oriented pearl-necklace arrays of metallic nanoparticles in polymers: A new route toward polarization-dependent color filters. *Adv. Mater.* 11, 223 (1999).
11. M. Quinten: The color of finely dispersed nanoparticles. *Appl. Phys. B: Lasers Opt.* 73, 317 (2001).
12. G.I. Stegeman and E.M. Wright: All-optical waveguide switching. *Opt. Quantum Electron.* 22, 95 (1990).
13. M. Bockstaller, R. Kolb, and E.L. Thomas: Metallodielectric photonic crystals based on diblock copolymers. *Adv. Mater.* 13, 1783 (2001).
14. M.R. Bockstaller and E.L. Thomas: Optical properties of polymer-based photonic nanocomposite materials. *J. Phys. Chem. B* 107, 10017 (2003).
15. A.J. Ward, J.B. Pendry, and W.J. Steward: Photonic dispersion surfaces. *J. Phys.: Condens. Matter* 7, 2217 (1995).
16. A. Convertino, A. Capobianchi, A. Valentini, and E.N.M. Cirillo: A new approach to organic solvent detection: High-reflectivity bragg reflectors based on a gold nanoparticle/teflon-like composite material. *Adv. Mater.* 15, 1103 (2003).
17. A. Biswas, H. Eilers, F. Hidden, O.C. Actas, and C.V.S. Kiran: Large broadband visible to infrared plasmonic absorption from Ag nanoparticles with a fractal structure embedded in a Teflon AF matrix. *Appl. Phys. Lett.* 88, 013103 (2006).
18. M. Westphalen, U. Kreibig, J. Rostalski, H. Lüth, and D. Meissner: Metal cluster enhanced organic solar cells. *Sol. Energy Mater. Sol. Cells* 61, 97 (2000).
19. B.P. Rand, P. Peumans, and S.R. Forrest: Long-range absorption enhancement in organic tandem thin-film solar cells containing silver nanoclusters. *J. Appl. Phys.* 96, 7519 (2004).
20. C.G. Granqvist: Solar energy materials. *Adv. Mater.* 15, 1789 (2003).
21. J. Wu, W. Walukiewicz, K.M. Yu, W. Shan, J.W. Ager III, E.E. Haller, H. Lu, W.J. Schaff, W.K. Metzger, and S. Kurtz: Superior radiation resistance of $In_{1-x}Ga_xN$ alloys: Full-solar-spectrum photovoltaic material system. *J. Appl. Phys.* 94, 6477 (2003).
22. D.A. Genov, A.K. Sarychev, and V.M. Shalaev: Metal-dielectric composite filters with controlled spectral windows of transparency. *J. Nonlin. Opt. Phys. Mater.* 12, 419 (2003).
23. A. Kiesow, J.E. Morris, C. Radehaus, and A. Heilmann: Switching behavior of plasma polymer films containing silver nanoparticles. *J. Appl. Phys.* 94, 6988 (2003).

C. MECHANICAL ELASITICTY OF VAPOUR-LIQUID-SOLID GROWN GaN NANOWIRES

IOP Publishing Nanotechnology
Nanotechnology 18 (2007) 135708 (8pp) doi:10.1088/0957-4484/18/13/135708

Mechanical elasticity of vapour–liquid–solid grown GaN nanowires

Yunxia Chen[1], Ian Stevenson[2], Rebecca Pouy[2], Lidong Wang[2], David N McIlroy[2], Tyler Pounds[3], M Grant Norton[3] and D Eric Aston[1,4]

[1] Department of Chemical Engineering, University of Idaho, PO Box 441021, Moscow, ID 83844-1021, USA
[2] Department of Physics, University of Idaho, PO Box 440903, Moscow, ID 83844-0903, USA
[3] School of Mechanical and Materials Engineering, Washington State University, Pullman, WA 99164, USA

E-mail: aston@uidaho.edu

Received 6 November 2006, in final form 19 January 2007
Published 28 February 2007
Online at stacks.iop.org/Nano/18/135708

Abstract
Mechanical elasticity of hexagonal wurtzite GaN nanowires with hexagonal cross sections grown through a vapour–liquid–solid (VLS) method was investigated using a three-point bending method with a digital-pulsed force mode (DPFM) atomic force microscope (AFM). In a diameter range of 57–135 nm, bending deflection and effective stiffness, or spring constant, profiles were recorded over the entire length of end-supported GaN nanowires and compared to the classic elastic beam models. Profiles reveal that the bending behaviour of the smallest nanowire (57.0 nm in diameter) is as a fixed beam, while larger nanowires (89.3–135.0 nm in diameter) all show simple-beam boundary conditions. Diameter dependence on the stiffness and elastic modulus are observed for these GaN nanowires. The GaN nanowire of 57.0 nm diameter displays the lowest stiffness (0.98 N m^{-1}) and the highest elastic modulus (400 ± 15 GPa). But with increasing diameter, elastic modulus decreases, while stiffness increases. Elastic moduli for most tested nanowires range from 218 to 317 GPa, which approaches or meets the literature values for bulk single crystal and GaN nanowires with triangular cross sections from other investigators. The present results together with further tests on plastic and fracture processes will provide fundamental information for the development of GaN nanowire devices.

1. Introduction

Investigation of the mechanical properties of nanowires is essential and of significant importance to determine the material strength for practical implementation as electronic or optical interconnects, as components in microelectromechanics, and as active or passive parts in nanosensors [1–8]. Mechanical failure of those interconnects or building blocks may lead to malfunction or even fatal failure of the entire device. Mechanical reliability, to some extent, will determine the long-term stability and performance for many of the nanodevices currently being designed and fabricated. When nanowire properties have been adequately explored and understood, their incorporation into solutions of practical problems will become evident more quickly and feasible for active and concerted pursuit.

Since GaN was synthesized in 1932 [9], large quantities of data have established GaN as an important semiconductor material with wide bandgap (3.4 eV), possessing high thermal stability, chemical inertness and hardness. Its properties make it a suitable material for high-power, high-temperature, high-voltage and high-frequency electronic or optoelectronic device applications [10, 11]. Research interest in GaN nanowires has increased significantly in recent years because for sufficiently thin shapes such as nanowires, quantum confinement effects are expected to lead to novel or enhanced physical properties of potential use in future nanotechnology.

[4] Author to whom any correspondence should be addressed.

GaN nanowires have been reported in numerous works to show promise as elemental building blocks for photonic, electronic and optoelectronic nanodevices including logic gates, field-effect transistors (FETs), light-emitting diodes (LEDs), subwavelength photonics components and so-called 'nanolasers' [12–17]. For integration into true nanodevices, controllable assembly and precise location of fabricated nanowires must be accomplished in device architectures. A better understanding of mechanical behaviour is just one of many aspects that require detailed study.

To date, the mechanical properties of bulk GaN (or films) have been studied by various techniques, such as Brillouin scattering, resonance ultrasound and nanoindentation [18–21]. Classical molecular dynamics has been adopted to investigate theoretically the mechanical properties of GaN nanotubes under tension and fatigue [22, 23]. The related studies revealed that mechanical properties of GaN are related to the preparation, microstructure, size and the measurement technique in use. Electromechanical resonance analysis in a transmission electron microscope (TEM) was used previously to infer the Young's modulus (E) and quality factor of GaN nanowires [24]. The modulus obtained for an 84 nm nanowire was close to the theoretical bulk value; but the inferred values of E decreased gradually for smaller diameters, which is difficult to resolve against the present understanding of mechanics and materials at the nanoscale.

Several methods have been proposed to investigate the mechanical properties of nanowires. Among them, bending tests using atomic force microscopy (AFM) in different modes is most common, such as contact mode [2, 7, 8, 25, 26], lateral force mode [27, 28] and digital pulsed force mode (DPFM) [29, 30]. The force–distance behaviour measured with AFM is interpreted based on classic beam model theory to measure stiffness and strength of nanowires, usually only for isolated midpoint measurements. This approach is valid when the nanowires follow linear elastic theory of isotropic materials and have high length-to-thickness ratios [3]. Compared to other AFM operations, DPFM combines the advantages of imaging and simultaneously performing three-point bending tests at every point imaged along the suspended nanowire [29, 30], not just single-position measurements as reported elsewhere [2, 7, 8, 25, 27, 28]. This technique provides enough data to resolve the uncertainty of positioning the AFM tip right at the midpoint and to investigate the validity of boundary condition assumptions.

In this study, we applied DPFM AFM to the study of the mechanical elasticity of vapour–liquid–solid (VLS) [31] grown GaN nanowires with diameters in the range of 57–135 nm. The bending deflection and effective bending stiffness profiles were recorded over the entire length of end-supported GaN nanowires. Elastic moduli (E) for these nanowires were computed and compared on the basis of classic mechanics models. The findings for elasticity and boundary condition behaviour were investigated and are discussed in detail.

2. Experimental details

2.1. Nanowire growth and characterization

GaN nanowires were synthesized using an iron catalyst (60 nm) deposited on silicon substrates through direct reaction of Ga and ammonia (NH_3) at 900 °C and atmospheric pressure via a VLS mechanism with a similar procedure as that published elsewhere [32]. The reaction duration was 30 min and the flow rate for NH_3 was in the range of 5–10 ml min^{-1}. The produced GaN nanowires by this method have diameters in the range of 30–150 nm (mostly ~85–140 nm) and lengths up to several hundred micrometres (figure 1(a)) as determined by field emission scanning electron microscopy (FE-SEM, SUPRA 35 VP, Zeiss). A transmission electron microscope (TEM, Philips CM200) 200 kV image shows the hexagonal cross section of a single GaN nanowire (figure 1(b)). The corresponding electron-diffraction pattern indicates that the nanowire is a single-crystalline hexagonal wurtzite structure with epitaxial growth orientation parallel to [0001]. The diffraction peaks (figure 1(c)) recorded with a Siemens D5000

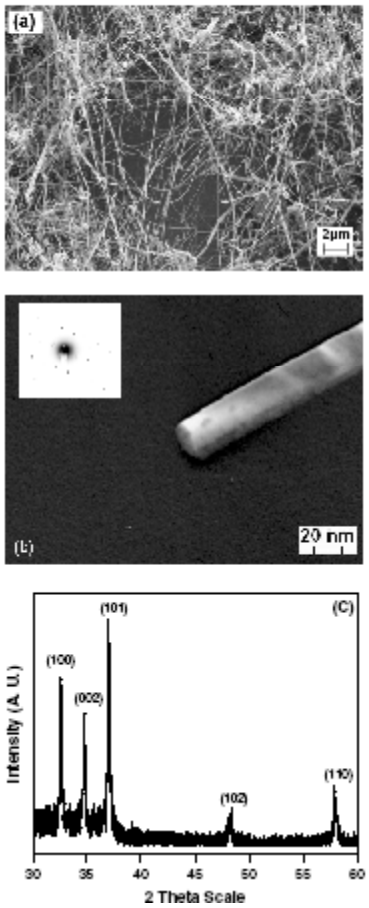

Figure 1. SEM image (a), dark-field TEM image and corresponding electron-diffraction pattern (b) and XRD pattern (c) of the synthesized GaN nanowires.

Table 1. Applied force (point load) on individual GaN nanowires and corresponding maximum deflection, bending angle and minimum effective stiffness.

No	Diameter (nm)	Length (nm)	Diameter to length ratio	Force (nN) Range	Force (nN) Average	Maximum deflection (nm)	Bending angle (deg)	Minimum stiffness (N m^{-1})
1	57.0	3054	53	98.8–122.7	107.8	109.1	4.1	0.98
2	89.3	2398	27	88.3–136.7	112.3	53.7	2.6	2.10
3	94.5	2427	26	38.7–72.1	53.5	31.6	1.5	2.13
4	97.8	2465	25	101.1–127.7	111.1	44.0	2.0	2.56
5	105.0	2611	25	123.4–166.4	139.4	43.9	1.9	3.23
6	109.7	2558	23	174.7–203.8	189.5	47.8	2.1	3.95
7	110.0	2220	20	263.8–274.6	269.5	55.5	2.9	4.83
8	111.0	2048	18	101.7–113.9	108.7	16.8	0.9	6.49
9	135.0	1794	13	273.8–300.5	283.9	16.0	1.0	17.32

or clamped ends (fixed model) and with simply supported ends (simple model). Two ends of the nanowires are clamped against bending moments in the fixed model, while the simple model allows free motion. The relationships between elastic modulus E and deflection z_x with a suspended (gauge) length of L at a certain tip position x subjected to a load F are given by [35–37]

$$\text{Fixed model:} \quad EIz_x = -\frac{F}{3L^3} \cdot x^3 \cdot (L-x)^3 \quad (3)$$

$$\text{Simple model:} \quad EIz_x = -\frac{F}{3L} \cdot x^2 \cdot (L-x)^2 \quad (4)$$

where I is the cross-sectional moment of inertia; $I = 5\sqrt{3}r^4/16$ for a solid, regular hexagon with a side length of r. The best fits to experimental deflection profiles were determined by shape comparison of classic models against the data using an average value for E as the fitted parameter. As shown later, the tested nanowires show maximum deflection at the middle with nearly symmetric profiles. Consequently, the mixed beam model (one end is simply supported and the other is fixed) used in our previous studies [30] was not relevant.

3. Results and discussion

Table 1 lists the maximum point force on the GaN nanowires applied at each pixel, the corresponding maximum deflection at the midpoint and bending angles near the edges for a midpoint deflection. All tested GaN nanowires display small bending angles (<4.1°) under applied force, and they have high length-to-diameter ratios (L/D > 13, mostly > 20), which make classic elastic beam theories valid for quantitative comparison in our case [35]. As expected, higher applied loads or smaller diameters gave rise to larger maximum deflections near the midpoint. For example, for comparable diameters of nanowires #6–8, nanowire #8 deflected 16.8 nm under a set-point load of ~110 nN, less than half the loading force of nanowire #7. The maximum deflection of nanowire #7 under ~270 nN load was 55.5 nm. A comparison of nanowire deflections under similar loading conditions (#1, #2, #4, #8) demonstrates the consistent and expected trend of decreasing midpoint deflection with increasing nanowire diameter.

Knowing the boundary conditions for bending profiles is extremely important for measuring the elastic modulus of nanowires accurately. A fixed-beam boundary shows a shallow slope in the deflection profile near the ends and has more curvature throughout the profile, while a simple-beam boundary gives a steeper slope at the ends, and the profile is more parabolic in shape rather than the subtle S-curve of the fixed beam. Profiles for mixed boundaries (one simply supported and one fixed) would show intermediate values of deformation and be asymmetric about the midpoint. Bending profiles of typical nanowires have been plotted as a function of relative tip position x/L, *as* shown in figure 3, to illustrate the experimental boundary conditions observed for GaN nanowires. The maxima in deflection at the middle and profile symmetry indicate comparable boundary conditions at each supported end. Accordingly, in this paper, only fixed and simple-beam models were needed to describe the bending tests. Theoretical profiles for fixed and simple beams are also shown in figure 3. The bending profile for a 57.0 nm nanowire shows a smoother transition in slope from the edge toward the midpoint, which is the main feature of fixed ends. All other tested nanowires, with diameters ranging from 89.3 to 135.0 nm, show sharper and steeper sloping for edge deflections, best fitted by the simple-beam boundary condition. All experimental deflection profiles exhibit a reasonable fit, though not perfect, with theoretical values from fixed or simple-beam models.

These findings are similar to previous DPFM data for silver nanowires but different from earlier experiments on polymer nanowires (silver and polymer nanowires did not require a polymer adhesion layer) [29, 30]. The deflection profiles of polymer nanowires were best fitted with a fixed-beam model even though they were quite large (170–200 nm). Silver nanowires showed fixed-end behaviour for smaller diameters under low loading conditions and resulted in simple supports for larger diameters, which consequently required high loading for similar deflections. Large silver nanowires under low applied force exhibited intermediate conditions, probably due to transitions from fixed to simple ends with increasing stress. Higher work of adhesion with the substrate was suspected for small nanowires due to increased capillary effects, or meniscus forces [30]. However, under relatively large applied force, the work of adhesion is not always sufficient to resist the resultant stresses.

Compared to silver, GaN nanowires show relatively weak adhesion to the substrate, demonstrated from initial AFM images on the silicon test gratings without a polymer adhesion layer. Though the polymer thin film improved adhesion, it was still insufficient in most cases for larger nanowires. Aside from nanowire size and experimental loading, this suggests that the

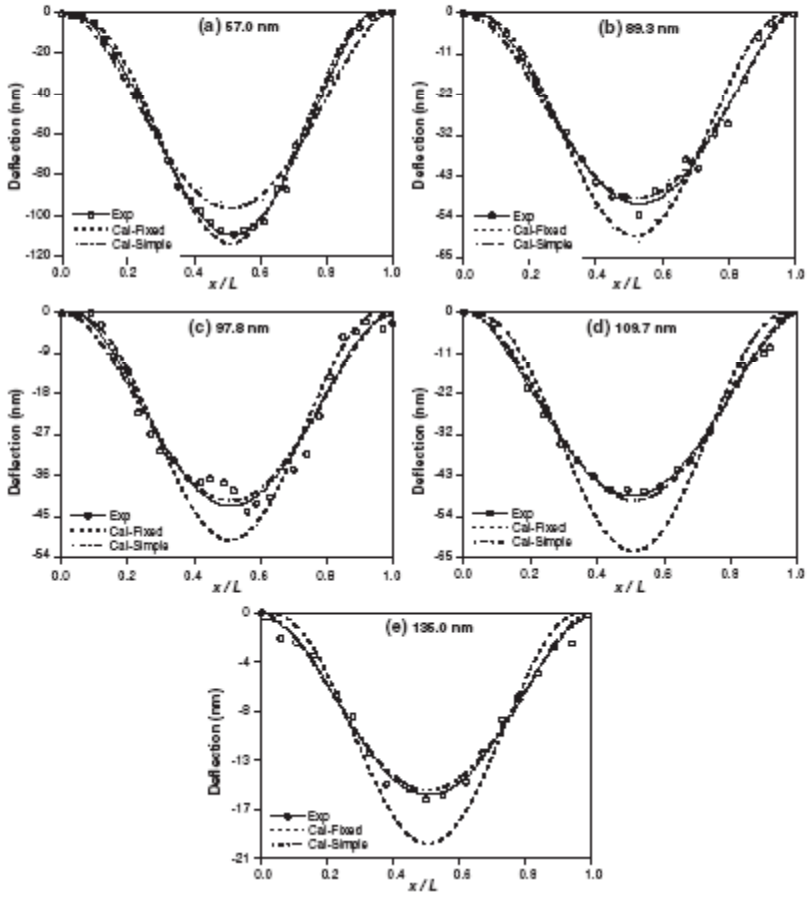

Figure 3. Comparison of experimental and model deflections for tested GaN nanowires.

intrinsic surface energy of GaN nanowires is quite low, as is well known of boron nitride. (Contact angle measurements with the water on substrates of random GaN nanowire coatings also exhibit complete nonwetting.) In the future, we will be investigating the adhesion between nanowire and substrate in order to obtain a comprehensive understanding of boundary conditions in bending tests.

Figure 4 displays effective bending stiffness profiles of selected GaN nanowires as a function of relative tip position x/L compared to fixed and simple models. As expected, effective bending stiffness of GaN nanowires increases from the midpoint to the edges, and it is inclined to infinity at the ends. As listed in table 1, the minimum stiffness (at the midpoint) increases regularly from 0.98 to 17.32 N m^{-1} as nanowire diameters increase from 57.0 to 135.0 nm. Stiffness profiles of GaN nanowires (except for ⌀57.0 nm case, which is fixed) exhibit a reasonable fit with theoretical stiffness as a simple beam. Deviations near the edges are due to increased experimental sensitivity of the three-point bending design and magnification of errors since the actual boundary conditions are not perfect.

After confirming the boundary conditions, GaN nanowire elastic moduli were computed using the appropriate model. Figure 5 shows elastic modulus for GaN nanowires versus diameters; decreasing from 400.1 ± 14.9 GPa (standard deviation errors) to 195.6 ± 19.7 GPa as diameter increases from 57 to 135 nm. The value of 400 GPa for 57 nm nanowire is from the fixed-beam model, while the simple-beam model was found to be valid for the 89.3–135.0 nm range. Moduli trends similar to our results were reported for many other nanowires, such as ZnO, SiC and TiO_2. The elastic modulus for ZnO nanowires with diameters smaller than 120 nm increases dramatically with decreasing diameters and is significantly higher than larger nanowires or bulk

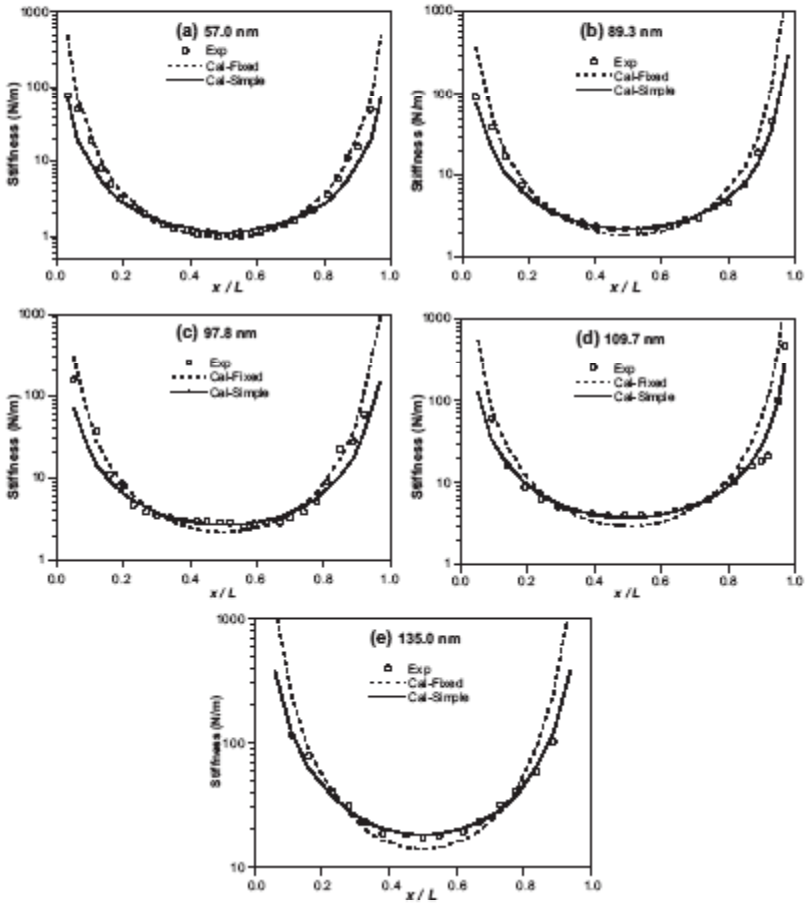

Figure 4. Comparison of experimental and model effective stiffness for tested GaN nanowires.

ZnO [38]. SiC nanorods were reported to approach the theoretical value for E when the diameter was reduced to ~20 nm [39]. Generally, physical properties such as elastic modulus are believed to be directly related to the material structural perfection [40]. The elastic stiffening for smaller nanowires can be explained by the lower probability of finding a defect in smaller volumes [38–40]. However, these findings are different from the results of silver and triangular GaN nanowires.

In our previous work, no obvious size dependence on E was observed for silver nanowires [30]. The opposite trend was observed in E for triangular GaN nanowires within the diameter range of 36–84 nm [24]. The authors suggested this converse behaviour was due to the increase of surface-to-volume ratio (S/V) with decreasing d. They believed the atomic coordination and cohesion near the surface were 'poor' relative to bulk, and the increasing dominance of the surface would decrease the rigidity of the structure [41]. Furthermore, nanowire shape and, microstructure are also determinate contributions to the difference in observed moduli trends: the GaN nanowires we produced have a hexagonal cross section grown along the [0001] direction (figure 1(b)), while those of [24] have a triangular cross-sectional shape grown along the [120] direction.

For most nanowires with diameters of 89–110 nm, the simple-beam model gave E = 218.1–316.9 GPa, which approaches or meets the literature values of ~295 GPa for bulk single crystal [19–21, 42]. Literature values for GaN nanowires with triangular cross sections were similar: 227–305 GPa for 36–84 nm diameter [24]. But for the smallest nanowire with diameter of 57.0 nm, E is as high as 400.1 ± 14.9 GPa from the fixed-beam model, which far exceeds the literature values. This

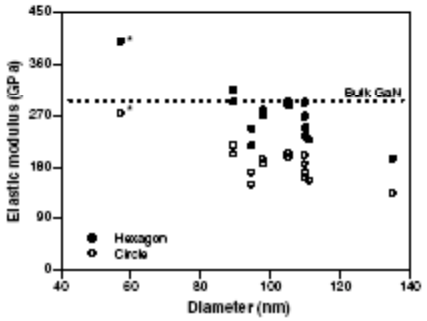

Figure 5. Elastic moduli for tested GaN nanowires versus nanowire diameters from the simple-beam model (*fixed-beam model).

may be due to variations in nanowire shape. Though the TEM image reveals a nearly hexagonal cross section for the GaN nanowire, it is not perfect. In fact, it is more like a 'circular' hexagon. For cross sections of regular circular and hexagonal shape, their inertial moments are as follows: $I_c = \pi r^4/4$ for a solid circular area with a radius of r and $I_h = 5\sqrt{3}r^4/16$ for solid regular hexagon with a side length of r, respectively. For a given nanowire deflection, the calculated E using a hexagonal cross section would be 45% larger than that with a circular cross section for the same observable width (figure 5). For relatively small nanowires, this becomes significant due to the fourth-order dependence in I on diameter.

With the boundary condition issue essentially solved, the practical uncertainty of diameter size and shape are the most significant sources of persisting error in nanomechanics. This error cannot be precisely determined because the exact shape of a specific nanowire is not available for confirmation. In addition, compared to those literature values, E for some tested GaN nanowires is low. Microstructure differences may contribute to this discrepancy. Via FE-SEM and TEM images, we have observed that some nanowires are not uniform in diameter or smooth on the surface. These microstructural irregularities may weaken the nanowire, as well as complicating comparison with the standard beam model assuming a uniform cross section. Obvious elastic weakening for nanowires or nanobelts was also observed in ZnO [6], lead zirconate titanate (PZT) [8] and ZnS [42, 43] compared to bulk materials. Elastic modulus of ZnO nanowires is even smaller (80%) than that of the bulk [6].

The theoretical propagation of errors is due primarily to uncertainty in

(i) nanowire diameter, and to a lesser degree, gauge length,
(ii) the use of a polymer adhesion layer,
(iii) boundary conditions,
(iv) shear deflection and indentation, and
(v) AFM scanner and detector calibrations, and cantilever stiffness.

Among them, the uncertainty in nanowire diameter is responsible for the greatest magnitude in total uncertainty of calculated E values. As discussed earlier, the classic elastic beam model is valid only under the assumption of a homogeneous beam, that is, constant and uniform E and I. Very slight variations in diameter are significant because of the fourth-order dependence in I of equations (3) and (4), resulting in an experimental error of ~10%. The error due to length is insignificant at ~0.3%. The polymer coating helped adhere to the nanowire but makes an absolute determination of nanowire deflection theoretically impossible, since there is no method to measure the compressibility of that layer independently for the three-point bending experiment with precision. Instead, the best solution is to subtract the indentation as measured on the supported end, which is currently the standard approach in the literature [7]. Due to high length-to-diameter ratio of tested nanowires and relatively low applied loads, shear and indentation deformation are insignificant. Even under the maximum experimental force (300 nN), both shear deformation and indentation are estimated as less than 0.3 nm (estimated with a spherical AFM tip), which gives an experimental error of ~1.7%.

The plastic and fracture process of these nanowires and their aging were not evaluated in the current study and cannot be deduced directly from consideration of mechanical elasticity. Extended experiments with increased applied loads, bending frequency and repetitions on GaN nanowire with both ends fixed can be pursued to advance the investigation of mechanical properties of nanowires and size–property relationships. Those findings will provide more detailed information for development of GaN nanowire devices. Increased failure strength is expected with decreased nanowire physical dimensions, due to the lower concentration of critically sized defects [44].

4. Conclusions

Mechanical elasticity of hexagonal wurtzite GaN nanowires with hexagonal cross sections grown via a VLS method have been investigated with advanced digital capabilities of AFM. Diameter dependence on the stiffness and elastic modulus is observed for these GaN nanowires (57.0–135.0 nm ⌀). With increasing diameter, elastic modulus decreases while stiffness increases. The bending behaviour of the nanowire with the smallest diameter (57 nm) reveals fixed-beam boundary conditions, while larger nanowires (89.3–135.0 nm) appear as simple beams that do not resist bending moments at the supported ends. The GaN nanowire of 57.0 nm diameter displays the lowest stiffness, or spring constant (0.98 N nm^{-1}), and the highest elastic modulus (400.1 ± 14.9 GPa). Elastic moduli for most tested nanowires range from 218.1 to 316.9 GPa, approaching or exceeding literature values for bulk single crystal and GaN nanowires with triangular cross sections, reported by others. These moduli are based on the assumption that all tested nanowires were of a hexagonal wurtzite structure with hexagonal cross sections, which is supported by complementary analytical techniques but cannot be known for certain of every nanowire. This uncertainty must be resolved before determining direct diameter-dependence effects on elasticity for GaN. With the details of the boundary condition well documented and understood, the practical uncertainty of variations in diameter size and shape for each individual nanowire are the most significant sources

of persisting error in nanomechanics. The coauthors are designing a combined AFM and spectroscopic experiment using *in situ* scanning Raman techniques to investigate the possibility of structural confirmation with adequate spatial resolution to identify each nanowire.

Acknowledgments

The authors gratefully acknowledge the support of the National Science Foundation (EPS-0132626, EPS-0447689) and the W M Keck Foundation. We thank Franklin Bailey, Brendan Twamley and Tom Williams at the University of Idaho for their SEM and XRD analyses. We also thank Glen Dunham at Pacific Northwest National Laboratory for supplying the polymer solution.

References

[1] Heidelberg A, Ngo L T, Wu B, Phillips M A, Sharma S, Kamins T I, Sader J E and Boland J J 2006 *Nano Lett.* 6 1101
[2] Ni H, Li X D and Gao H S 2006 *Appl. Phys. Lett.* 88 043108
[3] Withers J R and Aston D E 2006 *Adv. Colloid Sci.* 120 54
[4] Cuenot S, Demoustier-Champagne S and Nysten B 2000 *Phys. Rev. Lett.* 85 1690
[5] Li X D, Nardi P, Baek C-W, Kim J-M and Kim Y-K 2005 *J. Micromech. Microeng.* 15 551
[6] Song J H, Wang X D, Riedo E and Wang Z L 2005 *Nano Lett.* 5 1954
[7] Humar M, Arcon D, Umek P, Škarabot M, Muševič I and Bregar G 2006 *Nanotechnology* 17 3869
[8] Xu S, Shi Y and Kim S 2006 *Nanotechnology* 17 4497
[9] Johnson W C, Parsons J B and Crew M C 1932 *J. Phys. Chem.* 36 2561
[10] Strite S and Morkoç H 1992 *J. Vac. Sci. Technol.* B 10 1237
[11] Morkoç H 1999 *Nitride Semiconductors and Devices* (Heidelberg: Springer)
[12] Huang Y, Duan X, Cui Y, Lauhon L J, Kim K H and Lieber C M 2001 *Science* 294 1313
[13] Huang Y, Duan X F, Cui Y and Lieber C M 2002 *Nano Lett.* 2 101
[14] Zhong Z H, Qian F, Wang D L and Lieber C M 2003 *Nano Lett.* 3 343
[15] Johnson J C, Choi H-J, Knutsen K P, Schaller R D, Yang P and Saykally R J 2002 *Nat. Mater.* 1 106
[16] Stern E *et al* 2005 *Nanotechnology* 16 2941
[17] Pauzauskie P J, Sirbuly D J and Yang P D 2006 *Phys. Rev. Lett.* 96 143903
[18] Polian A, Grimsditch M and Grzegory I 1996 *J. Appl. Phys.* 79 3343
[19] Drory M D, Ager J W III, Suski T, Grzegory I and Porowski S 1996 *Appl. Phys. Lett.* 69 4044
[20] Schwarz R B, Khachaturan K and Weber E R 1997 *Appl. Phys. Lett.* 70 1122
[21] Nowak R, Pessa M, Suganuma M, Leszcynski M, Grzegory I, Porowski S and Yoshida F 1999 *Appl. Phys. Lett.* 75 2070
[22] Jeng Y R, Tsai P C and Fang T H 2004 *Nanotechnology* 15 1737
[23] Jeng Y R, Tsai P C and Fang T H 2005 *J. Nanosci. Nanotechnol.* 8 191
[24] Nam C Y, Jaroenapibal P, Tham D, Luzzi D E, Evoy S and Fisher J E 2006 *Nano Lett.* 6 153
[25] Bellan L M, Kameoka J and Craighead H G 2005 *Nanotechnology* 16 1095
[26] San Paulo A, Bokor J, Howe R T, He R, Yang P, Gao D, Carraro C and Maboudian R 2005 *Appl. Phys. Lett.* 87 053111
[27] Wu B, Heidelberg A, Boland J J, Sader J E, Sun X M and Li Y D 2006 *Nano Lett.* 6 468
[28] Wu B, Heidelberg A and Boland J J 2005 *Nat. Mater.* 4 525
[29] Shanmugham S, Jeong J, Alkhateeb A and Aston D E 2005 *Langmuir* 21 10214
[30] Chen Y X, Dorgan B L Jr, McIlroy D N and Aston D E 2006 *J. Appl. Phys.* 100 104301
[31] Wagner R S and Ellis W C 1964 *Appl. Phys. Lett.* 4 89
[32] Chen C C, Yeh C C, Chen C H, Yu M Y, Liu H L, Wu J J, Chen K H, Chen L C, Peng J Y and Chen Y F 2001 *J. Am. Chem. Soc.* 123 2791
[33] Sader J E 2005 *Atomic Force Microscope Cantilevers (Calibration Method of Sader)* Department of Mathematics and Statistics, University of Melbourne Website
[34] Tombler T W, Zhou C W, Alexseyev L, Kong J, Dai H J, Liu L, Jayanthi C S, Tang M J and Wu S Y 2000 *Nature* 405 769
[35] Gere J M and Timoshenko S P 1997 *Mechanics of Materials* (Boston, MA: PWS Publishing)
[36] Pilkey W D 1994 *Formulas for Stress, Strain, and Structural Matrices* (New York: Wiley)
[37] Roark R J and Young W C 1975 *Formulas for Stress and Strain* (New York: McGraw-Hill)
[38] Xiong Q, Duarte N, Tadigadapa S and Eklund P C 2006 *Nano Lett.* 6 1904
[39] Wong E W, Sheehan P E and Lieber C M 1997 *Science* 277 1971
[40] Cuenot S, Demoustier-Champagne S and Nysten B 2000 *Phys. Rev. Lett.* 85 1690
[41] Schmid M, Hofer W, Varga P, Stoltze P, Jacobsen K W and Nørskov J K 1995 *Phys. Rev.* B 51 10937
[42] Chen C Q, Shi Y, Zhang Y S, Zhu J and Yan Y J 2006 *Phys. Rev. Lett.* 96 075505
[43] Li X, Wang X, Xiong Q and Eklund P C 2005 *Nano Lett.* 5 1982
[44] Silva E C C M, Tong L, Yip S and Vliet K J V 2006 *Small* 2 239